HU ISSN 1586–2070

JOURNAL OF COMPUTATIONAL AND APPLIED MECHANICS

An Open Access International Journal

Published by the University of Miskolc

VOLUME 11, NUMBER 1 (2016)

MISKOLC UNIVERSITY PRESS

HU ISSN 1586–2070

JOURNAL OF COMPUTATIONAL AND APPLIED MECHANICS

An Open Access International Journal

Published by the University of Miskolc

VOLUME 11, NUMBER 1 (2016)

MISKOLC UNIVERSITY PRESS

Journal of Computational and Applied Mechanics, Vol. 11., No. 1., (2016), pp. 3–16
DOI: 10.32973/jcam.2016.001

OPTIMIZATION ALGORITHMS FOR LAMINATED COMPOSITE PANELS USING NONLINEAR MODAL FINITE ELEMENTS

Krzysztof Bogdanski
Faculty of Power and Aeronautical Engineering, Warsaw University of Technology
Ul. Nowowiejska 24, 00-665 Warszawa Poland
kbogdanski@meil.pw.edu.pl

Jean-Michel Dhainaut
Mechanical Engineering Deparment, Embry-Riddle Aeronautical University,
600 S Clyde Morris Blvd, Daytona Beach, FL 32114, USA
dhain460@erau.edu

Andres Josephsohn
San Andres School, Buenos-Aires, Argentina
Roque Saenz Pena 601, Buenos Aires, B1636FHA, Argentina
andres.josephsohn@sanandres.esc.edu.ar

[Received: February 2, 2016, Accepted: May 12, 2016]

Abstract. A methodology for minimization of composite panels deflections and stresses that uses a time domain nonlinear modal finite element model with two different optimization algorithms (genetic and DB algorithms) is described. The nonlinear modal formulation is based on geometrical nonlinearities rather than material nonlinearities, which does not require updating of the stiffness matrix at each time step, making it extremely time efficient when compared to commercial finite element softwares. Optimization algorithms are implemented in Matlab and can be used either with the finite element code itself or as a post-processing option. The method is applied to rectangular 10-ply symmetrically laminated plates under uniform pressure loads, with simply supported and clamped boundary conditions. The design constraints are based on the Tsai-Wu failure criterion. Results of the optimization using genetic algorithm include the influence of the initial size of population and number of generations. The DB algorithm proposed by the authors is shown to be more effective for the presented examples than the genetic algorithm.

Keywords: Composite optimization, lay-ups, stacking sequences, genetic algorithm, DB algorithm

1. Nomenclature

Latin Symbols

a, b	panel dimensions,
$_b$	indicates that a vector (or matrix) depends on bending
$_{mb}$	indicates that a vector (or matrix) depends on couples bending membrane ($_{mb=bm}$)
E	modulus of elasticity
G	shear modulus of elasticity

h	panel thickness
$_m$	indicates that a vector (or matrix) depends on membrane
z	distance from neutral axis
$[K]$	linear stiffness matrices
$[K1]$	first order stiffness matrices (they depend on $\{W_b\}$)
$[K2]$	second order stiffness matrices (they depend on $\{W_b\}$)
$[M]$	mass matrices
$P(t)$	time dependent load vector
u, v	in-plane displacements
W	transverse panel deflection.

Greek Symbols

ρ	panel density
ν	Poisson's ratio
ζ	damping coefficient

2. Introduction

The latest commercial aircraft from Boeing and Airbus, the 787 and the A350, first flew in 2009 and 2013, respectively. Both represented a technological step change by having structures composed of up to 50% of composite materials. They are only two examples of a trend that indicates that the industry will rely more and more on the beneficial properties of composites. The best mechanical properties of composite materials are obtained from laminates composed of many layers of unidirectional fibers embedded in a polymer matrix. These plies are distributed with different orientations, allowing the laminates properties to be tailored to the specific structural application. Hence, it is clear that to extract the maximum performance out of these materials, efficient stacking sequence optimization techniques are needed. Different optimization techniques based on Lagrangian minimization principle exist, however, in this work, the technique that will be explored is that of genetic algorithms (GA), which relies on evolutionary principles developed by Holland [1]. GA solve the problem of optimization by following a process analogous to what is observed in nature, where only the mutations that give an advantage to the individual are propagated to the new generations. The mechanics of GA is based on operations that result in structured, yet randomized exchange of genetic information between individual strings (chromosome strings) of the parents and consists of crossover, mutation and inversion [2]. For the sake of brevity, only the genetic representations for optimization of structural design will be discussed here. Goldberg and Samtani [3] were the first to use GA in structural design, solving the weight optimization problem of a 10 bar truss. Different variants of GA widely used in various structural problems have already been discussed in detail [4]. More specifically, multiple authors [5–7] combined commercially available finite element software with GA in the design of composite structures. However, it has been remarked that the major limitation in this application stems from the generality of the finite element package, i.e., those programs can be adapted to analyze composites but that is not their main objective. Hence, the novelty of the present work is that the authors would be using their own modal finite element program that is able to accurately predict the linear and nonlinear response of composite beams, plates, and shells subjected to different loading conditions at a reasonable computational cost. Accurate prediction of behavior of aircraft panels to different loading conditions is essential for design. Traditional design and analysis methods for commercial and military aircraft [8] [9] are based on linearization and simplified loading conditions. However, experimental data have shown that, in many instances, the loads induce large nonlinear deflection responses. Table 1 shows the non-dimensional displacement ($W_{\max}/h$) and the maximum normal stress for linear and nonlinear analysis of composite panels with varying stacking sequences when subjected to a uniform load of $1,500$ Pa. It can be seen that the linear analysis overpredicts the responses, something that will result in a heavier, overbuilt structure.

Table 1. Comparison of linear and nonlinear deformations and normal stresses

	Deformation $W_{\max}/h$		Normal stress σ [MPa]	
Stacking	Linear	Non-linear	Linear	Non-linear
0 0 0 0 0 0 0 0 0 0	1.067	0.534	33.58	12.63
-45 0 0 0 0 0 0 0 0 -45	1.283	0.616	140.19	40.54
-45 45 -45 45 -45 -45 45 -45 45 -45	1.302	0.765	153.43	59.30
45 90 90 90 45 45 90 90 90 45	2.375	0.989	265.95	61.10

h is the panel thickness

To the authors' best knowledge, all commercial finite element packages study geometrical nonlinear deformations at the structural degree of freedom, something that is extremely computationally expensive because all nonlinear matrices need to be reassembled at each time of the solution by considering deformations from the previous step. This is a severe obstacle in optimization that is intended to be overcome with the approach presented in this paper.

3. Formulation

This section introduces the fundamentals of the nonlinear modal formulation and genetic algorithms.

3.1. **Nonlinear modal finite element.** The governing equations of motion (EOM) for a two-dimensional panel subject to thermal and time dependent loading are developed. First, the EOM are expressed in terms of structural degrees of freedom (DOF) or in physical coordinates. Then the system level EOM are transformed into modal coordinates based on the expansion theorem. The plate is subjected to load intensities driving the response into the nonlinear range. The von Karman large deflection plate theory is employed here to describe the nonlinear strain and displacement relationships.

3.1.1. *Equations of motion in structural degrees of freedom.* The 24-DOF Bogner-Fox-Schmit C conforming rectangular plate element is used for the finite element model. Considering large amplitude deflections, i.e., that the transverse displacement of the panel is of the same order of magnitude as the panel thickness, the in-plane membrane response becomes coupled with the transverse bending. As the plate bends, the middle surface stretches and significant membrane forces develop. The load-transverse deflection response becomes nonlinear. The von-Karman plate theory addresses the above in-plane extension effects by introducing additional quadratic terms to the strains developed in a vibrating plate. The von-Karman nonlinear strain-displacement relationship is given by

$$\{\varepsilon\} = \left\{ \begin{array}{c} u_{,x} \\ v_{,y} \\ u_{,y} + v_{,x} \end{array} \right\} + \frac{1}{2} \left\{ \begin{array}{c} w_{,x}^2 \\ w_{,y}^2 \\ 2w_{,x}w_{,y} \end{array} \right\} + z \left\{ \begin{array}{c} -w_{,xx} \\ -w_{,yy} \\ -2w_{,xy} \end{array} \right\} = \\ = \left\{\varepsilon_m^0\right\} + \left\{\varepsilon_\theta^0\right\} + z\left\{\kappa\right\} \quad (1)$$

where $\left\{\varepsilon_m^0\right\}$ is the linear membrane strain vector, $\left\{\varepsilon_\theta^0\right\}$ is the von Karman nonlinear membrane strain vector, and $z\{\kappa\}$ is the bending strain vector.

When the principle of virtual work and the finite element expressions are combined, the assembled governing EOM for the panel subjected to aerodynamic, thermal, and acoustic excitations are derived and expressed as

$$\left[\begin{array}{cc} M_b & 0 \\ 0 & M_m \end{array} \right] \left\{ \begin{array}{c} \ddot{W}_b \\ W_m \end{array} \right\} + \\ \left(\left[\begin{array}{cc} K_b & K_{bm} \\ K_{mb} & K_m \end{array} \right] - \left[\begin{array}{cc} K_{N\Delta T} & 0 \\ 0 & 0 \end{array} \right] + \left[\begin{array}{cc} K1_{Nm} + K1_{Nb} & K1_{bm} \\ K1_{mb} & 0 \end{array} \right] + \left[\begin{array}{cc} K2 & 0 \\ 0 & 0 \end{array} \right] \right) \left\{ \begin{array}{c} W_b \\ W_m \end{array} \right\} = \\ = \left\{ \begin{array}{c} P_{b\Delta T} \\ P_{m\Delta T} \end{array} \right\} + \left\{ \begin{array}{c} P_b(T) \\ 0 \end{array} \right\} \quad (2)$$

or

$$[M]\,\{\ddot{W}\} + ([K_o] - [K_{N\Delta T}] + [K1] + [K2])\,\{W\} = \{P\} \quad (3)$$

where $\{P\} = \{P_{b\Delta t} + P_b(t)\}$. If the membrane inertia term $\{\ddot{W}_m\}$ is neglected, the in-plane displacement vector can be expressed in terms of the bending displacement as

$$\{W_m\} = [K_m]^{-1}\{P_{m\Delta T}\} - [K_m]^{-1}[K_{mb}]\{W_b\} - \\ - [K_m]^{-1}[K1_{mb}]\,\{W_b\} = \{W_m\}_0 + \{W_m\}_1 + \{W_m\}_2 \quad (4)$$

where $\{W_m\}_0 = [K_m]^{-1}\{P_{m\Delta T}\}$ is a constant matrix in function of the linear membrane matrix $[K_m]$ and the constant membrane in-plane load $\{P_{m\Delta T}\}$; $\{W_m\}_1 = -[K_m]^{-1}[K_{mb}]\{W_b\}$ is in function of the constant membrane matrix $[K_m]$, the constant coupling bending-membrane matrix $[K_{mb}]$ and the linear vertical bending deformation $\{W_b\}$; $\{W_m\}_2 = -[K_m]^{-1}[K1_{mb}(W_b)]\,\{W_b\}$ is in function of the constant matrix $[K_m]$, the first order nonlinear matrix $[K1_{mb}]$ which depends on $\{W_b\}$ and the bending deformation $\{W_b\}$. Consequently, the term $\{W_m\}_2$ quadratically ($\{W_b\}^2$) depends on $\{W_b\}$. Thus $[K1_{Nm}]$ which depends on $\{W_m\} = \{W_m\}_0 + \{W_m\}_1 + \{W_m\}_2$ has three components $\left[K1_{Nm}^0\right]$ evaluated with $\{W_m\}_0$, $\left[K1_{Nm}^1\right]$ evaluated with $\{W_m\}_1$ and $\left[K1_{Nm}^2\right]$ evaluated with $\{W_m\}_2$. Recalling that $\{W_m\} =$

$\{W_m\}_0+\{W_m\}_1+\{W_m\}_2$ it should be clear that $\{W_m\}$ is the sum of a constant term $\{W_m\}_0$, and two terms that depends on the bending deformation $\{W_b\}$ only. The term $\{W_m\}_1$ depend linearly on $\{W_b\}$ while the term $\{W_m\}_2$ depends quadratically on $\{W_b\}$. Next, by substituting $\{W_m\}$ which is now in function of $\{W_b\}$ into equation (2), the system EOM can be written in terms of the bending deformation $\{W_b\}$ only

$$[M_b]\left\{\ddot{W}_b\right\}+ \\ +\left([K_L]+[K1\left(W_b\right)]+\left[K2\left(W_b^2\right)\right]\right)\{W_b\}=\{F\} \tag{5}$$

where

$$[K_L]=[K_b]-[K_{N\Delta T}]+[K1_{bm}]\,[K_m]^{-1}\,[P_{m\Delta T}]- \\ -[K1_{bm}]\,[K_m]^{-1}\,[K_{mb}]+\left[K1^0_{Nm}\right]\ , \tag{6a}$$

$$[K1]=[K1_{Nb}]+\left[K1^1_{Nm}\right]-[K_{bm}]\,[K_m]^{-1}\,[K1_{mb}]- \\ -[K1_{bm}]\,[K_m]^{-1}\,[K_{mb}]\ , \tag{6b}$$

$$[K2]=[K2_b]+\left[K1^2_{Nm}\right]-[K1_{bm}]\,[K_m]^{-1}\,[K1_{mb}] \tag{6c}$$

and

$$\{F\}=\{P_{b\Delta T}\}+\{P_b(t)\}-[K_{bm}]\,[K_m]^{-1}\,\{P_{m\Delta T}\}\ . \tag{6d}$$

For more details on the derivation of the nonlinear modal formulation readers can consult [10]

3.1.2. *Equations of motion in modal degree of freedom.* Equation (5) is expressed in terms of structure DOF, which means a costly computational burden since the governing equations increase proportionally with the number of elements. This obstacle is resolved by transforming the system EOM in the structural DOF into a set of truncated modal coordinates by expressing the response as a linear combination of some base functions

$$\{W_b\}=\sum_{r=1}^{n} q_r\left(t\right)\{\phi_r\}=[\Phi_b]\{q\} \tag{7}$$

where $q_r(t)$ denotes the modal coordinates of the r-th mode, which reflects the contribution to the total deflection from the r-th mode; $\Phi_b=[\phi_1,\phi_2,\ldots,\phi_r,\ldots,\phi_n]$ is the modal matrix, in which ϕ_r is the mode shape due to the transverse bending of the r-th mode obtained from the linear vibration analysis.

The transformation of system governing EOM into modal coordinates is achieved by substituting equation (6) into equation (5) and pre-multiplying the whole equation by $[\Phi_b]^T$. If structural modal damping in the form of ζ_r $(r=1,2,\ldots,n)$ is assumed the transformed EOM in modal coordinates can be written in a brief form as follows:

$$\left[\bar{M}_b\right]\ \{\ddot{q}\}+2\zeta_r\frac{\omega_r}{\omega_0^2}\left[\bar{M}_b\right]\{\dot{q}\}+ \\ +\left(\left[\bar{K}_L\right]+\left[\bar{K}_q\right]+\left[\bar{K}_{qq}\right]\right)\ \{q\}=\left\{\bar{F}\right\} \tag{8}$$

Here the diagonal mass matrix is of the form

$$\left[\bar{M}_b\right] = \left[\Phi_b\right]^T \left[M_b\right] \left[\Phi_b\right] \tag{9}$$

The linear, quadratic, and cubic stiffness matrices are as follows:

$$\begin{aligned}\left[\bar{K}_L\right] = {}& \left[\Phi_b\right]^T \left(\left[K_b\right] - \left[K_{N\Delta T}\right]\right) \left[\Phi_b\right] + \\ &+ \left[\Phi_b\right]^T \left(\left[K1_{bm}\right]\left[K_m\right]^{-1}\left[P_{m\Delta T}\right]\right)\left[\Phi_b\right] - \left[\Phi_b\right]^T \left(\left[K1_{bm}\right]\left[K_m\right]^{-1}\left[K_{mb}\right]\right)\left[\Phi_b\right] + \\ &+ \left[\Phi_b\right]^T \left(\left[K1^0_{Nm}\right]\right)\left[\Phi_b\right] ,\end{aligned} \tag{10}$$

$$\begin{aligned}\left[\bar{K}_q\right] = {}& \left[\Phi_b\right]^T \left(\sum_{r=1}^{n} q_r \left(\left[K1_{Nb}\right]^{(r)} + \left[K1^1_{Nm}\right]^{(r)}\right)\right)\left[\Phi_b\right] - \\ &- \left[\Phi_b\right]^T \left(\sum_{r=1}^{n} q_r \left(\left[K_{bm}\right]\left[K_m\right]^{-1}\left[K1_{mb}\right]^{(r)}\right)\right)\left[\Phi_b\right] - \\ &- \left[\Phi_b\right]^T \left(\sum_{r=1}^{n} q_r \left(\left[K1_{bm}\right]^(r)\left[K_m\right]^{-1}\left[K_{mb}\right]\right)\right)\left[\Phi_b\right] ,\end{aligned} \tag{11}$$

$$\begin{aligned}\left[\bar{K}_{qq}\right] = {}& \left[\Phi_b\right]^T \left(\sum_{r=1}^{n}\sum_{s=1}^{n} q_r q_s \left(\left[K2\right]^{(rs)} + \left[K1^2_{Nm}\right]^{(rs)}\right)\right)\left[\Phi_b\right] - \\ &- \left[\Phi_b\right]^T \left(\sum_{r=1}^{n}\sum_{s=1}^{n} q_r q_s \left(-\left[K1_{bm}\right]^{(r)}\left[K_m\right]^{-1}\left[K1_{mb}\right]^{(s)}\right)\right)\left[\Phi_b\right]\end{aligned} \tag{12}$$

The modal load vector is given by:

$$\begin{aligned}\left\{\bar{F}\right\} = {}& \left[\Phi_b\right]^T \left\{P_{b\Delta T}\right\} + \left[\Phi_b\right]^T \left\{P_b\left(t\right)\right\} - \\ &- \left[\Phi_b\right]^T \left[K_{bm}\right]\left[K_m\right]^{-1}\left\{P_{m\Delta T}\right\} .\end{aligned} \tag{13}$$

3.2. **Genetic algorithms.** The application of GA operators to a problem first requires the representation of the possible combinations of the variables in terms of bit strings, analogous to chromosomes in biological genetics [2]. In order to increase the speed of the genetic search the following assumptions are considered: i) the stacking sequences are limited to using 0°, ±45° and 90° plies; ii) the laminate thickness can only be an integer multiple of the standard ply thickness; iii) the laminate is symmetric. The initial population set is generated by a function that generates pseudo-random numbers uniformly and, to generate future generations, parents are selected from the initial population based on their fitness. Next, genetic operators are used to create new stacking sequences: the children population. Good features from the initial population set propagate to the children population by using a biased roulette wheel where better parents are assigned a larger area. A description of the genetic operators for the construction of new generations is given next [7].

Crossover operator. Once a pair of parents is selected, the children are generated by combining information from both parents, for example, by splicing the left part of the string of one of the parents with the right part of the string from the other parent.

Parent 1: $[90/0/45]_s$
Parent 2: $[45/90/0]_s$ possible child designs are:

Child: [90/90/0]s, [90/0/0]s, [45/0/45]s, $[45/90/45]_s$

It is important to note that the present work utilizes a modified crossover algorithm given the constraints that all laminates must be symmetric.

Mutation operator. Mutation performs the valuable task of preventing premature loss of important genetic information by introducing random alteration in the child string obtained by the crossover operator. Inferior designs may have some good traits that would get lost in the gene pool (roulette wheel) when the parents are not selected. For example if you only consider the first child from the crossover [90/90/45]s a possible mutation is [90/0/45]s, which may lead to a good design but that would not be accounted for by the crossover operator.

The implementation of the GA was done in Matlab®. Due to the assumptions mentioned in Section 2.2, the number of possible solutions (stacking sequences) is limited and is generated as a matrix.

To fully test the program, ensuring that it fulfills all of the assumptions, the results for each layup are calculated and stored in a separate matrix. In the final version of the program, this approach can be easily replaced by real time calculations.

In the first generation, a specified number (size of population) of indices (corresponding to their chromosomes) are selected using random permutations. Selected chromosomes form the population and the random permutations used ensure the selection of unique (non-repeating) sets. The results for every chromosome are then sorted by increasing values of the Tsai-Wu failure criterion on the outer (first) layer of the laminate. That forms the fitness function. The best two from the list are then selected as parents and will be used in crossover and mutation operations. Afterwards, parents are crossed over with the rest of the population forming offspring. Subsequently, these two parents are mutated and form new sets of chromosomes. From parents, offspring and mutated chromosomes, a list of unique stacking sequences is formed and the corresponding results are extracted from the result matrix. The fitness function (value of Tsai-Wu for the outer layer) is evaluated and the ordered results constitute the first generation. Subsequent generations are generated in a similar way but, instead of randomly choosing chromosomes at the start, the best two from the previous generation become parents and the rest are used for crossover operation.

3.3. **DB algorithm.** The authors propose a DB algorithm that reduces the optimization computational cost. It does not depend on either the size of the populations nor on the number of generations. The advantage of such an approach will be explained in the results section.

At first only one stacking sequence is randomly chosen. Since the ply orientations are limited to only four angles, i.e., $0°$, $\pm 45°$ and $90°$, the chosen layup is replicated three times. In the next step, a randomly chosen layer is replaced in the replicated layups with all the other possible angle ply orientations.

Example:
Randomly chosen stacking: [90/0/45]
Newly formed stacking sequences with the third layer replaced: [90/0/0], [90/0/-45], [90/0/90].

According to the fitness function (the same as the one used in genetic algorithm: value of Tsai-Wu for the outer layer), the best layup is chosen from the four stacking sequences. This best stacking is then replicated again three times and a different layer is now replaced with the other ply orientations. That process is repeated until all of the layers have been replaced and the very best out of all stacking sequences is chosen. The number of calculations is equal to: $N_{o\,\mathrm{calc}} = L(A-1)+1$ where L is the number of layers and A is the number of possible angle ply orientations. In the present case, $L = 5$ and $A = 4$, giving $N_{o\,\mathrm{calc}} = 16$. Using the same matrices with stacking sequences and results a program using the DB algorithm has been written using Matlab®.

4. Results

4.1. **Material properties.** Composite and isotropic panels are used to validate the finite element code and the DB algorithm. The material properties of isotropic aluminum panels are $E_1 = 73$ GPa, $\nu = 0.30$, $\rho = 2750$ kg/m^3 and of composite Graphite/Epoxy T300/5208 $E_1 = 181.0$ GPa, $E_2 = 10.3$ GPa, $G_{12} = 7.17$ GPa, $G_{23} = 6.21$ GPa, $\nu_{12} = 0.28$ and $\rho = 1550$ kg/m^3.

A proportional damping ratio of $\zeta_r\omega_r = \zeta_s\omega_s$ with $\zeta_1 = 0.02$ is used for transient responses. For validation purposes, simply-supported (S-S) boundary conditions are considered and for generalization clamped (C) boundary conditions are considered as well. For all support cases the maximum deformation occurs at the center of the panel for the uniform loading but the maximum stress depends on the support conditions. For instance, maximum stress occurs at center of the plate for SS but at the midpoint of the longest edge for C conditions. Preliminary mesh convergence and modal convergence was verified for all composite panels. It was found that eight modes were sufficient for converged stress responses on a 24×24 mesh. The validation of the nonlinear modal finite element code and of the GA can be done separately since they are completely independent of each other. The former is only used to evaluate the responses, and the GA is simply a numerical procedure used for finding the optimum stacking sequence but does not depend on the linearity of the responses.

4.2. **Validation.** The validation of the present nonlinear modal FE formulation, equation (7), is performed by comparing results for isotropic SS panels obtained with classical formulation [11]. The linear and nonlinear stiffness matrices will be verified by solving the single mode linear and nonlinear free vibration problems, respectively. Table 2 shows the non-dimensional frequency parameter $\omega a\sqrt{\rho(1-\nu^2)/E_1}$ which neglects the in-plane inertia and characterizes the linear free vibration behavior by the fundamental linear bending mode (1,1) only. Results are obtained for different shell geometries ranging from spherical shells ($R_x/R_y = 1$) to hyperbolic paraboloids

($R_x/R_y = -1$). The curved panels ($b/a = 1$) are modeled by an 8×8 mesh on a quarter shell, more than adequate for modeling the fundamental mode (1,1). The validation was performed on curved and cylindrical panels because no data for flat panels was available.

Table 2. Non-dimensional frequency parameter $\omega a\sqrt{\rho(1-\nu^2)/E_1}$

	$\varpi a\sqrt{\rho(1-\nu^2)/E_1}$	
R_x/R_y	Ref. [11]	F.E.
-1.0	0.05695	0.05831
-0.5	0.06174	0.06251
0.0	0.07429	0.07471
0.5	0.09144	0.09178
1.0	0.1111	0.1115
$R_x = R_y$		
3.048	0.1111	0.1115
5.08	0.07429	0.08096
12.7	0.06007	0.006145
25.4	0.05776	0.005813
$H = h/a$		
0.005	0.09955	0.09901
0.01	0.1111	0.1115
0.02	0.1485	0.1489
0.1	0.5622	0.5778
0.2	1.033	1.1437

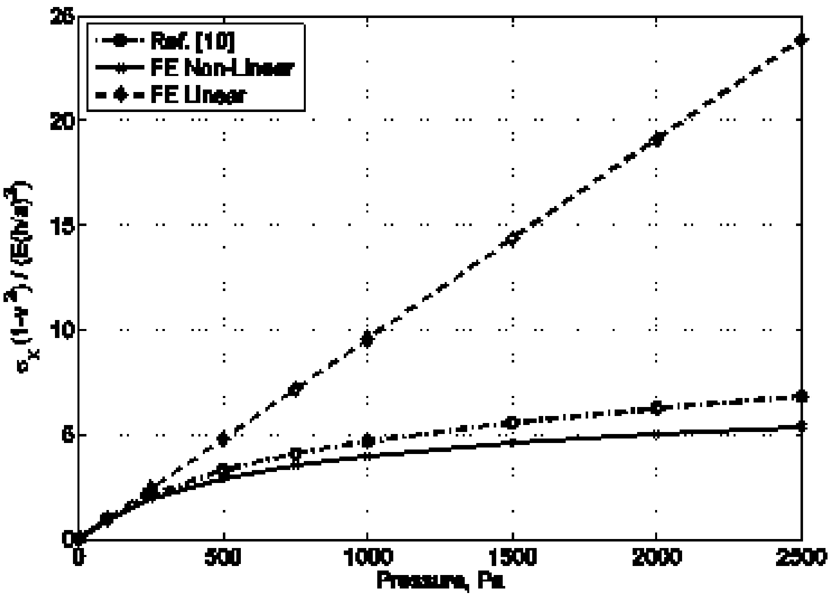

Figure 1. Non-dimensional stress vs. uniform pressure

It can be observed that results compare very well, except for the very thick shell case ($h/a = 0.2$) where the difference is 10.7%.

The stress convergence was based on stresses rather than displacements because the Tsai-Wu failure criteria used for the optimization is based on stresses. The same mesh size and number of modes will be employed in subsequent sections.

This difference is due to the fact that the present modal FE formulation neglects shear effects, negligible for thin-shells but significant in thick ones. The uniform pressure loading is verified on a $0.254 \times 0.381 \times 0.00127$ m ($12 \times 15 \times 0.05$ in.) flat panel modeled with a 20×20 mesh on a full panel. Isotropic material properties and simply-supported boundary conditions are assumed. Figure 1 shows the non-dimensional stress at different uniform load intensities.

4.3. **Results.** *Genetic algorithm.* The GA algorithm was tested on several different population sizes with the following assumptions: i) stacking sequences consisted of 10 layers (5 symmetrical), ii) there are 1024 possible (unique) stacking sequences. Calculations have been performed for both simply supported and clamped boundary conditions

Since all the stacking sequences were calculated, it was found that for the applied load and simply supported boundary conditions, the highest value of Tsai-Wu for one layup was more than twenty times greater than the lowest. The distribution of the results in comparison to the lowest value is shown in Figure 2. The solution is treated as converged if the result of the Tsai-Wu for the outer layer does not differ more than 5% from the best result of the 1024 stacking sequences. This results in a list consisting of 24 solutions (2.34% of the total population).

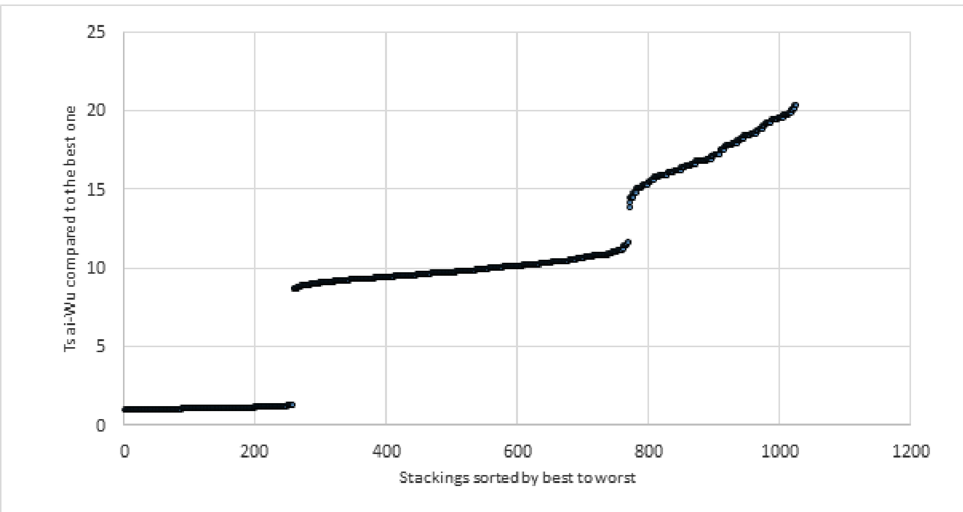

Figure 2. Distribution of results for simply supported boundary conditions in comparison to the best result

Table 2 presents the results for simply supported boundary conditions of the stacking sequences generated using the GA sorted by each generation and population size. Each of the results has been calculated using statistics based on 40 samples. Number of solutions means how many unique calculations have to be performed after every generation. The adjacent column contains the percentage of the results obtained after every generation that belong to the set of the 24 best results. The least number of calculations performed in order to find the best results was 46 with the population of 15 after the fourth generation. A 90% chance of achieving the best solution is possible after 30 calculations with the population size of 10 after the fifth generation. The same efficiency can be obtained after the second generation with a 50% larger population. However, the computational cost is 23% higher.

Table 3. Percentage of 24 best results (2.3% of all possible) in each generation sorted by population size

Population size	5		10		15	
Generation	Number of solutions	%	Number of solutions	%	Number of solutions	%
1	11	25	13	45	27	85
2	15	35	20	50	37	90
3	18	65	23	70	47	90
4	20	75	27	70	46	100
5	22	85	30	90	47	100
6	24	85	33	95	49	100
7	25	85	35	95	50	100

Population size	20		25		30	
Generation	Number of solutions	%	Number of solutions	%	Number of solutions	%
1	26	75	40	85	37	95
2	34	85	53	100	52	100
3	40	95	62	100	58	100
4	46	95	68	100	63	100
5	50	100	70	100	67	100
6	53	100	73	100	70	100
7	56	100	75	100	73	100

The results in Table 3 clearly show that the larger the population size, the higher the probability of getting the best answer in that generation. However, due to the larger size, the number of solutions needed to be calculated grows rapidly. To get a 90% chance of getting the solution, the lowest number of solutions is 30 with a population size of 10 after the fifth generation. The same efficiency can be obtained after the second generation with a 50% larger population but the computational cost is 23% higher.

Table 4 shows how the probability of finding the best solution decreases when for convergence the best 1% of the results is selected as opposed to 2.3%. It is worth noting that with a population size of 30, all of the results were in the best 1% of the results after the second generation.

Table 4. Comparison of percentage of 10 and 24 best results in each generation sorted by population size

Population size	10		20		30	
Generation	Best 10 [%]	Best 24 [%]	Best 10 [%]	Best 24 [%]	Best 10 [%]	Best 24 [%]
1	25	45	55	75	80	95
2	30	50	70	85	100	100
3	35	70	80	95	100	100
4	45	70	85	95	100	100
5	65	90	90	100	100	100
6	80	95	95	100	100	100
7	90	95	95	100	100	100

Table 5. Percentage of 9 best results (0.88% of all possible) for fixed boundary conditions in each generation sorted by population size

Population size	5		10		15	
Generation	Number of solutions	%	Number of solutions	%	Number of solutions	%
1	12	15	16	15	34	30
2	17	20	23	25	46	45
3	20	20	28	30	52	60
4	22	35	33	45	55	60
5	23	40	35	50	59	70
6	24	45	37	55	62	70
7	26	60	38	55	63	75

Population size	20		25		30	
Generation	Number of solutions	%	Number of solutions	%	Number of solutions	%
1	29	40	48	60	41	65
2	42	60	64	65	55	80
3	50	65	71	65	63	90
4	56	70	74	70	70	95
5	59	70	76	80	74	95
6	62	70	82	85	79	100
7	65	75	84	85	82	100

The second tested example differed by changing the boundary conditions from simply supported to clamped. Using the same criterion that the result of the Tsai-Wu for the outer layer does not differ more than 5% from the best result of the 1024 stacking sequences, the results list consists of only 9 solutions (0.9% of the total population). Table 5 presents the results for fixed boundary conditions using GA. In comparison to the simply supported boundary conditions the results are worse due to the lesser number of results considered for convergance. A 90% chance of achieving the best solution is possible with the population size of 30 after 63 calculations and three generations. In order to have a 100% chance of getting the solution converged, the number of calculations has to increase up to 79 (by 25.4%).

4.3.1. *DB Algorithm.* Since the DB algorithm is simpler because it is not influenced by the number of generations or population size, the analysis of the results is significantly faster.

The algorithm was run 10,000 times and in 80.6% of the calculations the best result, out of 1,024, was obtained. The two best results for simply supported boundary conditions were obtained in 100% of the calculations. Compared to the presented GA, 16 unique calculations would result in a maximum 45% chance of finding a solution in the best 24 possible results, whereas there is a 100% chance of getting one of the best two results with the DB algorithm. For fixed boundary conditions, the DB algorithm would give a 72.3% chance of converging (one of the best 9 results). Using the GA, 16 unique calculations would only give a 15% chance of achieving the converging solution. It is worth mentioning that the worst result obtained for the DB algorithm was the 72nd best answer and only appeared in 0.18% of all of the performed calculations.

5. Conclusions

An efficient nonlinear finite element modal formulation was combined with two different optimization algorithms. It was shown that the newly developed DB algorithm is more effective than the most popular GA for the studied cases.

For the first case (simply supported boundary conditions) and given assumptions, the GA allows finding a result in the best 1% of all of the results, with about 90% efficiency, by calculating about 3% of all of the possible solutions. By reducing the efficiency to 85%, the computational costs only drops to requiring the calculation of 2.2% of the solutions. Since the GA is basically a semi-controlled random process, it does not guarantee finding the best answer in the process. On the other hand, the DB algorithm gave a 100% chance of finding one of the best two solutions after only 16 calculations (1.6% of all possible stacking sequences) and in 80% of cases it gave the best possible solution.

The second tested case (fixed boundary conditions)also shoed better results gained from the DB algorithm compared to the GA. It has given a 72.3% chance of convergence compared to only 15% for the GA after 16 unique calculations. A 100% chance of finding a result in the best 1% of all of the results is possible using GA, but it takes on average 79 unique calculations. In future work, the authors will keep on testing and developing the DB algorithm, including increasing the number of layers and applying more complex loads.

References

1. Holland, J. H.: *Adaptation of Natural and Artificial Systems*. MIT Press, 1992. ISBN: 978-0-262-08213-6.
2. Gürdal, H. R. T., Z. and Hajela, P.: *Design Optimization of Laminated Composite Materials*. Wiley Inter-Science, 1999. ISBN: 0-471-25276.
3. Goldberg, D. E. and Samtani, M. P.: Engineering optimization via genetic algorithm. In *Proceedings of the 9th Conference on Electronics Computation, February 23-26*, American Society of Civil Engineers, 1986, pp. 471–482. ISBN-13: 978-0872625129.
4. Haftka, R. T.: *Genetic Algorithms for Optimization of Composite Laminates*, pp. 431–442. In Mechanics of Composite materials and Structures, NATO Sc. Series, Vol. 361., Editor: C. A. M. Soares, Kluwer Academic Publisher, 1999.
5. Muc, A. and Gurba, W.: Genetic algorithms and finite element analysis in optimization of composite structures. *Composite Structures*, **54**, (2001), 275–281.
6. Walker, M. and Smith, R. E.: A technique for multi-objective optimization of laminated composite structures using genetic algorithms and finite element analysis. *Composite Structures*, **62**, (2003), 123–128.
7. Almeida, F. S. and Awruch, A. M.: Design optimization of composite laminated structures using genetic algorithms and finite element analysis. *Composite Structures*, **88**, (2009), 443–454.
8. Holehouse, I.: *Sonic Fatigue Design Techniques for Advanced Composites Aircraft Structures*. Technical report: AFWL-TR-80-3019, Rohr Industries, P.O. Box 878, Chula Vista, California, 92012, 1980. 1-190.
9. Rudder, F. F. and Plumbee, H. E.: Sonic Fatigue Design Guide for Military Aircraft. Technical report: AFFDL-TR-74-112, AF Flight Dynamics Laboratory, Wright Petterson Air Force Base, Ohio 45433, 1975. 1-571.
10. Dhainaut, J.-M.: Nonlinear Response and Fatigue Estimate of Surface Panels to White and Non-White Random Exitations. Ph.D. thesis, Old Dominion, Norfolk, VA, 2001.
11. Locke, J. E.: A Finite Element Formulation for the Large Deflection Random Response of Thermally Buckled Structures. Ph.D. thesis, Old Dominion University, Norfolk, VA, 1988.

Journal of Computational and Applied Mechanics, Vol. 11., No. 1., (2016), pp. 17–32
DOI: 10.32973/jcam.2016.002

SPHERICAL STRAIN STATE OF INCOMPRESSIBLE ELASTIC BODIES

István Ecsedi and Attila Baksa
University of Miskolc
Institute of Applied Mechanics, Hungary
istvan.ecsedi@uni-miskolc.hu, attila.baksa@uni-miskolc.hu

[Received: February 29, 2016 Accepted: May 5, 2016]

Abstract. This paper is concerned with the statics of an isotropic, linearly elastic, homogeneous incompressible body. The body considered is bounded by two spherical surfaces and two conical surfaces. The centre of the spherical surfaces and the apex of conical surfaces are the same point. The concept of the spherical strain state is introduced and the concerning boundary value problem of elastic equilibrium is formulated in terms of a displacement potential and the mean stress. Two examples illustrate the applications of the derived equations. The analytical solutions we have obtained are compared with FEM solutions computed by the `Abaqus` finite element software.

Mathematical Subject Classification: 70B10, 70B15
Keywords: Spherical strain state, incompressible, linearly elastic

1. Introduction

As is well known the displacement based finite element solutions for incompressible isotropic elastic bodies have some difficulties such as the Poisson ratio locking [1, 2]. Poisson (volumetric) locking is a serious problem which cannot be avoided by refining the mesh. All the standard fully integrated finite elements will lock in the incompressible limit, and some elements show very poor performance if the Poisson ratio ν is approximately 0.5. The source of the error of the finite element solution when the Poisson ratio ν is close to 0.5 is that the finite element interpolation functions are unable to properly approximate a volume preserving strain field [1]. Therefore it is of great importance to find exact analytical solutions for some statical problems of incompressible elastic bodies which then can be compared with the finite element solutions. The aim of this paper is to give a new class of the exact benchmark solutions for incompressible elastic bodies.

The present paper is concerned with a statical boundary value problem of an isotropic, homogeneous, incompressible elastic body. The body considered is bounded by two spherical surfaces ∂V_1, ∂V_2 and two conical surfaces ∂V_3, ∂V_4. The centre of the spherical surfaces ∂V_1, ∂V_2 and the apex of the conical surfaces ∂V_3, ∂V_4 are the same point O as shown in Figure 1. A spherical polar coordinate system $Or\varphi\vartheta$ is introduced with an origo O (Figure 1). The body shown in Figure 1 is said to be in the Spherical Strain State (SSS) if its displacement field has the form

$$u_r = 0, \quad u_\vartheta = rU_\vartheta(\vartheta,\varphi), \quad u_\varphi = rU_\varphi(\vartheta,\varphi), \tag{1.1}$$

where u_r, u_ϑ and u_φ are the components of the displacement vector $\boldsymbol{u} = u_r\boldsymbol{e}_r + u_\varphi\boldsymbol{e}_\varphi + u_\vartheta\boldsymbol{e}_\vartheta$ and $\boldsymbol{e}_r$, $\boldsymbol{e}_\varphi$ and $\boldsymbol{e}_\vartheta$ are the unit vectors of the spherical coordinate system $Or\varphi\vartheta$. Application of the strain-displacement relationships of the linearised theory of elasticity leads to the next results for the strains in the spherical coordinate system $Or\varphi\vartheta$ [4, 5]

$$\varepsilon_r = 0, \quad \varepsilon_\vartheta(\vartheta,\varphi) = \frac{\partial U_\vartheta}{\partial\vartheta}, \quad \varepsilon_\varphi(\vartheta,\varphi) = \frac{1}{\sin\vartheta}\frac{\partial U_\varphi}{\partial\varphi} + U_\vartheta\cot\vartheta \tag{1.2}$$

$$\gamma_{r\varphi} = \gamma_{r\vartheta} = 0, \quad \gamma_{\varphi\vartheta}(\vartheta,\varphi) = \frac{1}{\sin\vartheta}\frac{\partial U_\vartheta}{\partial\varphi} + \frac{\partial U_\varphi}{\partial\vartheta} - U_\varphi\cot\vartheta. \tag{1.3}$$

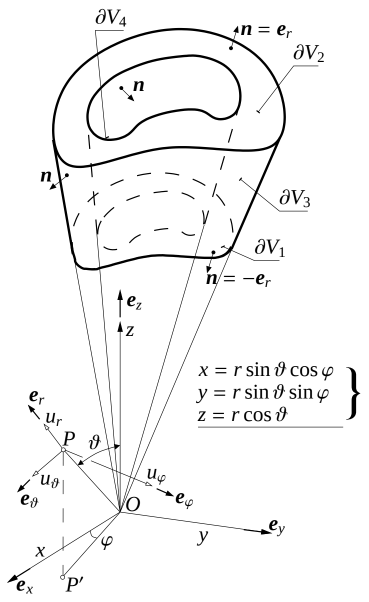

Figure 1. Space domain bounded by spherical and conical surfaces

The material of the body considered is homogeneous, isotropic, incompressible and linearly elastic. According to Hooke's law for $\nu = 0.5$ we can write [3]

$$\sigma_r = 2G\varepsilon_r + \sigma_0, \tag{1.4}$$

$$\sigma_\varphi = 2G\varepsilon_\varphi + \sigma_0, \tag{1.5}$$

$$\sigma_\vartheta = 2G\varepsilon_\vartheta + \sigma_0, \tag{1.6}$$

$$\tau_{r\varphi} = G\gamma_{r\varphi}, \qquad \tau_{r\vartheta} = G\gamma_{r\vartheta}, \tag{1.7}$$

$$\tau_{\varphi\vartheta} = G\gamma_{\varphi\vartheta}, \tag{1.8}$$

where σ_r, σ_φ and σ_ϑ are the normal stresses, $\tau_{r\varphi}$, $\tau_{r\vartheta}$ and $\tau_{\varphi\vartheta}$ are the shearing stresses, G is the shear modulus of elasticity and σ_0 is the mean stress defined by the following equation

$$\sigma_0 = \frac{1}{3}(\sigma_r + \sigma_\varphi + \sigma_\vartheta). \tag{1.9}$$

For incompressible elastic body in SSS we have [3]

$$\operatorname{div}\boldsymbol{u} = \varepsilon_r + \varepsilon_\varphi + \varepsilon_\vartheta = \frac{\partial U_\vartheta}{\partial \vartheta} + \frac{1}{\sin\vartheta}\frac{\partial U_\varphi}{\partial \varphi} + U_\vartheta \cot\vartheta = 0. \tag{1.10}$$

2. Boundary value problem

The following prescriptions define the boundary value problem of the elastic equilibrium we shall consider,

- There is no body forces in V, where V is the space domain occupied by body shown in Figure 1.
- The boundary conditions are given by the following equations:

$$u_r = 0 \quad \text{and} \quad \tau_{r\varphi} = \tau_{r\vartheta} = 0 \quad \text{on} \quad \partial V_1 \cup \partial V_2, \tag{2.1}$$

$$\boldsymbol{p}_3 = \boldsymbol{T}\cdot\boldsymbol{n}, \quad \boldsymbol{p}_3 = \widetilde{\boldsymbol{p}}_3 \quad \text{on} \quad \partial V_3 \quad \text{or} \quad \boldsymbol{u} = \widetilde{\boldsymbol{u}}_3 \quad \text{on} \quad \partial V_3, \tag{2.2}$$

$$\boldsymbol{p}_4 = \boldsymbol{T}\cdot\boldsymbol{n}, \quad \boldsymbol{p}_4 = \widetilde{\boldsymbol{p}}_4 \quad \text{on} \quad \partial V_4 \quad \text{or} \quad \boldsymbol{u} = \widetilde{\boldsymbol{u}}_4 \quad \text{on} \quad \partial V_4, \tag{2.3}$$

  The applied traction vector $\widetilde{\boldsymbol{p}}_i$ $(i = 3,\, 4)$ and the prescribed surface displacement $\widetilde{\boldsymbol{u}}_i$ on the boundary surface segment ∂V_i $(i = 3,\, 4)$ have the forms

$$\widetilde{\boldsymbol{p}}_i = \widetilde{p}_{i\vartheta}(\vartheta,\varphi)\boldsymbol{e}_\vartheta + \widetilde{p}_{i\varphi}(\vartheta,\varphi)\boldsymbol{e}_\varphi \qquad (i = 3, 4), \tag{2.4}$$

$$\widetilde{\boldsymbol{u}}_i = r\left(\widetilde{U}_{i\vartheta}(\vartheta,\varphi)\boldsymbol{e}_\vartheta + \widetilde{U}_{i\varphi}(\vartheta,\varphi)\boldsymbol{e}_\varphi\right) \qquad (i = 3, 4). \tag{2.5}$$

We remark that the radial coordinate r is constant on the boundary parts ∂V_i $(i = 1, 2)$, that is, $r = r_i$ where r_i is a constant. Observe that the traction vectors $\widetilde{\boldsymbol{p}}_3$ and $\widetilde{\boldsymbol{p}}_4$ cannot be prescribed arbitrarily, they should statisfy an equation. Later on we shall derived this equation from the condition of global mechanical equilibrium.

In the present case the local equilibrium condition can be given in the following form [4, 5]:

$$\boldsymbol{T}\cdot\nabla = \boldsymbol{0} \quad \text{in}\, V, \tag{2.6}$$

where ∇ is the gradient (del) operator. By applying the Gauss divergence theorem we get from equation (2.6) that

$$\int\limits_V \boldsymbol{T}\cdot\nabla\,\mathrm{d}V = \int\limits_{\partial V} \boldsymbol{T}\cdot\boldsymbol{n}\,\mathrm{d}A = \int\limits_{\partial V_1} \boldsymbol{T}\cdot\boldsymbol{n}\,\mathrm{d}A + \int\limits_{\partial V_2} \boldsymbol{T}\cdot\boldsymbol{n}\,\mathrm{d}A + \int\limits_{\partial V_3} \boldsymbol{T}\cdot\boldsymbol{n}\,\mathrm{d}A + \int\limits_{\partial V_4} \boldsymbol{T}\cdot\boldsymbol{n}\,\mathrm{d}A = \boldsymbol{0}. \tag{2.7}$$

Here $\boldsymbol{n}$ is the outer unit normal vector on the boundary surface $\partial V = \bigcup_{i=1}^{4} \partial V_i$ and $\mathrm{d}A$ is the area element:

$$\mathrm{d}A = r_i^2 \sin\vartheta \,\mathrm{d}\vartheta \,\mathrm{d}\varphi = r_i^2 \,\mathrm{d}a \quad \text{and} \quad \boldsymbol{n} = (-1)^i \boldsymbol{e}_r \quad \text{on} \quad \partial V_i \, (i = 1, 2), \tag{2.8a}$$

$$\mathrm{d}A = r \,\mathrm{d}r \,\mathrm{d}s_i \quad \text{and} \quad \boldsymbol{n} = n_\vartheta(\vartheta,\varphi)\boldsymbol{e}_\vartheta + n_\varphi(\vartheta,\varphi)\boldsymbol{e}_\varphi \quad \text{on} \quad \partial V_i \, (i = 3, 4). \tag{2.8b}$$

In equations (2.8a,b) $\mathrm{d}a$ is the area element on a unit sphere and $\mathrm{d}s_i$ $(i = 3, 4)$ is the arc element on the intersection line of the conical surface ∂V_i $(i = 3, 4)$ and the unit sphere $(r = 1)$. It follows from equation (2.7) that the force equilibrium equation for the whole body assumes the following form

$$\int_{\partial V} \boldsymbol{T}\cdot\boldsymbol{n}\,\mathrm{d}A = -\int_{\partial V_1} \sigma_r \boldsymbol{e}_r \,\mathrm{d}A + \int_{\partial V_2} \sigma_r \boldsymbol{e}_r \,\mathrm{d}A + \int_{\partial V_3} \boldsymbol{p}_3 \,\mathrm{d}A + \int_{\partial V_4} \boldsymbol{p}_4 \,\mathrm{d}A =$$

$$(r_2^2 - r_1^2) \int_a \sigma_r \boldsymbol{e}_r \,\mathrm{d}a + \frac{r_2^2 - r_1^2}{2} \left(\int_{\partial a_3} \boldsymbol{p}_3 \,\mathrm{d}s_3 + \int_{\partial a_4} \boldsymbol{p}_4 \,\mathrm{d}s_4 \right) = \boldsymbol{0}, \tag{2.9}$$

where the hollow two-dimensional domain a on the unit sphere $0 < \vartheta < \pi$ is bounded by the intersection line of the conical surfaces ∂V_3, ∂V_4 and the unit sphere. It is clear from Figure 2 that the boundary curve of a is $\partial a = \partial a_3 \cup \partial a_4$. A detailed form of equation (2.9) is given by

$$2\int_a \sigma_r(\vartheta,\varphi)\boldsymbol{e}_r \sin\vartheta \,\mathrm{d}\vartheta \,\mathrm{d}\varphi + \int_{\partial a_3} \boldsymbol{p}_3(s_3)\,\mathrm{d}s_3 + \int_{\partial a_4} \boldsymbol{p}_4(s_4)\,\mathrm{d}s_4 = \boldsymbol{0}. \tag{2.10}$$

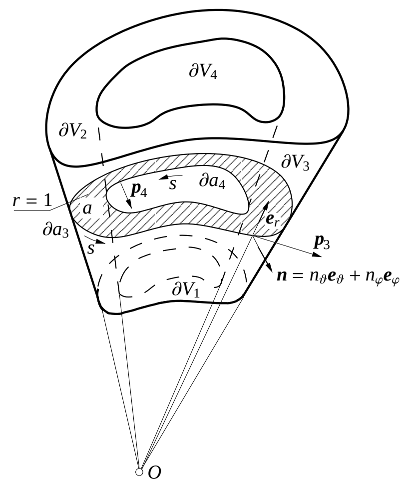

Figure 2. Definition of domain a on the unit ball.

Equation (2.10) shows how the surface forces $\widetilde{\boldsymbol{p}}_3$, $\widetilde{\boldsymbol{p}}_4$ are related to the stresses on the boundary surface $\partial V_1 \cup \partial V_2$. We would like to emphasise that equation (2.9) does not provide any constraint for the applied surface forces given by relation (2.4).

In the absence of body forces the local equilibrium condition

$$\boldsymbol{r}\times\boldsymbol{T}\cdot\nabla=\boldsymbol{0}\qquad(\boldsymbol{r}=r\boldsymbol{e}_r)\tag{2.11}$$

can be transformed into a global one in the same way as we did for equation (2.6). We obtain

$$\int_V \boldsymbol{r}\times\boldsymbol{T}\cdot\nabla\,\mathrm{d}V=\int_{\partial V}\boldsymbol{r}\times\boldsymbol{T}\cdot\boldsymbol{n}\,\mathrm{d}A-\int_V(\boldsymbol{e}_x\times\boldsymbol{T}\cdot\boldsymbol{e}_x+\boldsymbol{e}_y\times\boldsymbol{T}\cdot\boldsymbol{e}_y+\boldsymbol{e}_z\times\boldsymbol{T}\cdot\boldsymbol{e}_z)\,\mathrm{d}V$$
$$=\int_{\partial V}\boldsymbol{r}\times\boldsymbol{T}\cdot\boldsymbol{n}\,\mathrm{d}A=\boldsymbol{0},\tag{2.12}$$

where we have taken into account that [4, 5]:

$$\boldsymbol{e}_x\times\boldsymbol{T}\cdot\boldsymbol{e}_x+\boldsymbol{e}_y\times\boldsymbol{T}\cdot\boldsymbol{e}_y+\boldsymbol{e}_z\times\boldsymbol{T}\cdot\boldsymbol{e}_z=\boldsymbol{0},\tag{2.13}$$

Here $\boldsymbol{e}_x$, $\boldsymbol{e}_y$ and $\boldsymbol{e}_z$ are the unit vectors of the Cartesian coordinate system $Oxyz$ shown in Figure 1.

It follows from equations (2.11) and (2.12) that

$$\int_{\partial V}\boldsymbol{r}\times\boldsymbol{T}\cdot\boldsymbol{n}\,\mathrm{d}A=\int_{\partial V_1}\boldsymbol{r}\times\boldsymbol{T}\cdot\boldsymbol{n}\,\mathrm{d}A+\int_{\partial V_2}\boldsymbol{r}\times\boldsymbol{T}\cdot\boldsymbol{n}\,\mathrm{d}A+\int_{\partial V_3}\boldsymbol{r}\times\boldsymbol{p}_3\,\mathrm{d}A+\int_{\partial V_4}\boldsymbol{r}\times\boldsymbol{p}_4\,\mathrm{d}A=$$
$$-r_1\int_{\partial V_1}\boldsymbol{e}_r\times\sigma_r\boldsymbol{e}_r\,\mathrm{d}A+r_2\int_{\partial V_2}\boldsymbol{e}_r\times\sigma_r\boldsymbol{e}_r\,\mathrm{d}A+\int_{r_1}^{r_2}r^2\Big(\int_{\partial a_3}\boldsymbol{e}_r\times\boldsymbol{p}_3\,\mathrm{d}s_3\Big)\mathrm{d}r+$$
$$\int_{r_1}^{r_2}r^2\Big(\int_{\partial a_4}\boldsymbol{e}_r\times\boldsymbol{p}_4\,\mathrm{d}s_4\Big)\mathrm{d}r=\boldsymbol{0}.\tag{2.14}$$

The moment equilibrium equation (2.14) we have derived can be rewritten into a more compact form

$$\int_{\partial a_3}\boldsymbol{e}_r\times\boldsymbol{p}_3\,\mathrm{d}s_3+\int_{\partial a_4}\boldsymbol{e}_r\times\boldsymbol{p}_4\,\mathrm{d}s_4=\boldsymbol{0}.\tag{2.15}$$

This equation is the constraining equation the applied surface forces $\widetilde{\boldsymbol{p}}_3$ and $\widetilde{\boldsymbol{p}}_4$ should meet. Consequently, for the boundary value problem we have defined in this section the constraint equation (2.15) we have established is a solvability condition.

For the displacement boundary conditions of the form

$$\boldsymbol{u}=\widetilde{\boldsymbol{u}}_3=r\widetilde{\boldsymbol{U}}_3\quad\text{on}\quad\partial V_3\quad\text{and}\quad\boldsymbol{u}=\widetilde{\boldsymbol{u}}_4=r\widetilde{\boldsymbol{U}}_4\quad\text{on}\quad\partial V_4\tag{2.16}$$

we can rewrite the solvability condition (2.15) by utilising the incompressiblity condition (1.10):

$$\int_{\partial a_3}\widetilde{\boldsymbol{U}}_3\cdot\boldsymbol{n}\,\mathrm{d}s_3+\int_{\partial a_4}\widetilde{\boldsymbol{U}}_4\cdot\boldsymbol{n}\,\mathrm{d}s_4=\boldsymbol{0}.\tag{2.17}$$

3. Formulation of elastic equilibrium in terms of displacement potential and mean stress

In our formulation the unknown fields are $U_\vartheta = U_\vartheta(\vartheta, \varphi)$, $U_\varphi = U_\varphi(\vartheta, \varphi)$ and $\sigma_0 = \sigma_0(\vartheta, \varphi)$. Let $F = F(\vartheta, \varphi)$ be a displacement potential in the terms of which

$$U_\vartheta = \frac{1}{\sin\vartheta}\frac{\partial F}{\partial \varphi}, \qquad U_\varphi = -\frac{\partial F}{\partial \vartheta}. \tag{3.1}$$

are the two displacement components. It follows from equations (1.2), (1.3) and (3.1) that the strains are

$$\varepsilon_\vartheta = \frac{\partial}{\partial\vartheta}\left(\frac{1}{\sin\vartheta}\frac{\partial F}{\partial\varphi}\right), \tag{3.2}$$

$$\varepsilon_\varphi = -\frac{\partial}{\partial\vartheta}\left(\frac{1}{\sin\vartheta}\frac{\partial F}{\partial\varphi}\right), \tag{3.3}$$

and

$$\gamma_{\varphi\vartheta} = \frac{1}{\sin^2\vartheta}\frac{\partial^2 F}{\partial\varphi^2} - \sin\vartheta\frac{\partial}{\partial\vartheta}\left(\frac{1}{\sin\vartheta}\frac{\partial F}{\partial\vartheta}\right). \tag{3.4}$$

For a sufficiently smooth otherwise arbitrary displacement potential $F = F(\vartheta, \varphi)$ the condition of incompressiblity

$$\varepsilon_r + \varepsilon_\vartheta = 0 \tag{3.5}$$

is identically satisfied. Upon substitution of equations (3.2), (3.3) and (3.4) into Hooke's law (1.4-1.9) we get the stresses in terms of the displacment potential:

$$\sigma_\vartheta = 2G\frac{\partial}{\partial\vartheta}\left(\frac{1}{\sin\vartheta}\frac{\partial F}{\partial\varphi}\right) + \sigma_0, \tag{3.6}$$

$$\sigma_\varphi = -2G\frac{\partial}{\partial\vartheta}\left(\frac{1}{\sin\vartheta}\frac{\partial F}{\partial\varphi}\right) + \sigma_0, \tag{3.7}$$

$$\sigma_0 = \sigma_r = \frac{1}{2}\left(\sigma_\vartheta + \sigma_\varphi\right), \tag{3.8}$$

$$\tau_{\varphi\vartheta} = G\left[\frac{1}{\sin^2\vartheta}\frac{\partial^2 F}{\partial\varphi^2} - \sin\vartheta\frac{\partial}{\partial\vartheta}\left(\frac{1}{\sin\vartheta}\frac{\partial F}{\partial\vartheta}\right)\right], \tag{3.9}$$

$$\tau_{r\varphi} = \tau_{r\vartheta} = 0. \tag{3.10}$$

It is well known that the equilibrium equations (2.6) in spherical polar coordinate system are as follows [3, 4]:

$$\frac{\partial\sigma_r}{\partial r} + \frac{1}{r}\frac{\partial\tau_{\vartheta r}}{\partial\vartheta} + \frac{1}{r\sin\vartheta}\frac{\partial\tau_{\varphi r}}{\partial\varphi} + \frac{1}{r}\left(2\sigma_r - \sigma_\vartheta - \sigma_\varphi + \tau_{\vartheta r}\cot\vartheta\right) = 0, \tag{3.11}$$

$$\frac{\tau_{\vartheta r}}{\partial r} + \frac{1}{r}\frac{\partial\sigma_\vartheta}{\partial\vartheta} + \frac{1}{r\sin\vartheta}\frac{\partial\tau_{\varphi\vartheta}}{\partial\varphi} + \frac{1}{r}\left[(\sigma_\vartheta - \sigma_\varphi)\cot\vartheta + 3\tau_{r\vartheta}\right] = 0, \tag{3.12}$$

$$\frac{\partial\tau_{r\varphi}}{\partial r} + \frac{1}{r}\frac{\partial\tau_{\varphi\vartheta}}{\partial\vartheta} + \frac{1}{r\sin\vartheta}\frac{\partial\sigma_\varphi}{\partial\varphi} + \frac{1}{r}\left(2\tau_{\varphi\vartheta}\cot\vartheta + 3\tau_{r\varphi}\right) = 0. \tag{3.13}$$

For SSS problems these equations assume the form

$$\frac{\partial \sigma_\vartheta}{\partial \vartheta} + \frac{1}{\sin\vartheta}\frac{\partial \tau_{\varphi\vartheta}}{\partial \varphi} + (\sigma_\vartheta - \sigma_\varphi)\cot\vartheta = 0, \tag{3.14}$$

$$\frac{\partial \tau_{\varphi\vartheta}}{\partial \vartheta} + \frac{1}{\sin\vartheta}\frac{\partial \sigma_\varphi}{\partial \varphi} + 2\tau_{\varphi\vartheta}\cot\vartheta = 0, \tag{3.15}$$

since $\sigma_\vartheta = \sigma_\vartheta(\vartheta,\varphi)$, $\sigma_\varphi = \sigma_\varphi(\vartheta,\varphi)$ and $\sigma_r = \sigma_0 \equiv \sigma_0(\vartheta,\varphi)$.

A combination of equations (3.6), (3.7) and (3.8) with equations (3.14) and (3.15) yields a coupled system of differential equations for $F = F(\vartheta,\varphi)$ and $\sigma_0 = \sigma_0(\vartheta,\varphi)$:

$$\frac{1}{G}\frac{\partial \sigma_0}{\partial \vartheta} + L_\vartheta[F] = 0, \tag{3.16}$$

$$\frac{1}{G}\frac{\partial \sigma_0}{\partial \varphi} + L_\varphi[F] = 0, \tag{3.17}$$

where

$$L_\vartheta[F] = 2\frac{\partial^2}{\partial\vartheta^2}\left(\frac{1}{\sin\vartheta}\frac{\partial F}{\partial\varphi}\right) + \frac{1}{\sin^3\vartheta}\frac{\partial^3 F}{\partial\varphi^3} - \frac{\partial}{\partial\vartheta}\left(\frac{1}{\sin\vartheta}\frac{\partial^2 F}{\partial\vartheta\partial\varphi}\right) + 4\cot\vartheta\frac{\partial}{\partial\vartheta}\left(\frac{1}{\sin\vartheta}\frac{\partial F}{\partial\varphi}\right), \tag{3.18}$$

$$\begin{aligned} L_\varphi[F] = {} & \frac{\partial}{\partial\vartheta}\left(\frac{1}{\sin^2\vartheta}\frac{\partial^2 F}{\partial\varphi^2}\right) - \frac{\partial}{\partial\vartheta}\left[\sin\vartheta\frac{\partial}{\partial\vartheta}\left(\frac{1}{\sin\vartheta}\frac{\partial F}{\partial\vartheta}\right)\right] \\ & - \frac{2}{\sin\vartheta}\frac{\partial}{\partial\vartheta}\left(\frac{1}{\sin\vartheta}\frac{\partial^2 F}{\partial\varphi^2}\right) + 2\frac{\cot\vartheta}{\sin^2\vartheta}\frac{\partial^2 F}{\partial\varphi^2} - 2\cos\vartheta\frac{\partial}{\partial\vartheta}\left(\frac{1}{\sin\vartheta}\frac{\partial F}{\partial\vartheta}\right). \end{aligned} \tag{3.19}$$

For a simply connected region a fulfillment of the Schwarz theorem

$$\frac{\partial}{\partial\vartheta}\left(\frac{\partial\sigma_0}{\partial\varphi}\right) = \frac{\partial}{\partial\varphi}\left(\frac{\partial\sigma_0}{\partial\vartheta}\right) \tag{3.20}$$

assures that the function $\sigma_0 = \sigma_0(\vartheta,\varphi)$ is determined with the accuracy of an arbitrary constant of integration $\overline{\sigma}_0 = \sigma_0(\vartheta_0,\varphi_0)$ which is the value of the function $\sigma_0 = \sigma_0(\vartheta,\varphi)$ at the point P_0.

For a double connected region a $(0 < \vartheta < \pi)$ – this is our case – fulfillment of condition (3.20) is necessary but not sufficient. The additional condition to be satisfied is of the form

$$\int\limits_{\partial a_4}\frac{\partial\sigma_0}{\partial\vartheta}\mathrm{d}\vartheta + \int\limits_{\partial a_4}\frac{\partial\sigma_0}{\partial\varphi}\mathrm{d}\varphi = 0\,. \tag{3.21}$$

A combination of equations (3.16), (3.17) and (3.20), (3.21) results in the following two equations:

$$\frac{\partial L_\vartheta[F]}{\partial\varphi} - \frac{\partial L_\varphi[F]}{\partial\vartheta} = 0 \qquad (\vartheta,\varphi)\in a, \tag{3.22}$$

$$\int\limits_{\partial a_4} L_\vartheta[F]\mathrm{d}\vartheta + \int\limits_{\partial a_4} L_\varphi[F]\mathrm{d}\varphi = 0\,. \tag{3.23}$$

With the knowledge of the displacement potential $F = F(\vartheta, \varphi)$ the mean stress is

$$\sigma_0(\vartheta, \varphi) = \sigma_0(\vartheta_0, \varphi_0) - G \left(\int\limits_{\widehat{P_0P}} L_\vartheta[F] \mathrm{d}\vartheta + \int\limits_{\widehat{P_0P}} L_\varphi[F] \mathrm{d}\varphi \right), \tag{3.24}$$

where $\widehat{P_0P}$ is an arbitrary curve in a with end points P_0 and P and the constant of integration $\sigma_0(\varphi_0, \vartheta_0)$ can be obtained from the stress boundary conditions (2.2) and (2.3).

4. Examples

4.1 Example 1. Lamé's problem for a hollow circular cone. The body considered in this example is bounded by two spherical surfaces ∂V_i $(i = 1, 2)$ of radius r_i $(i = 1, 2)$ and two circular conical surfaces ∂V_i $(i = 3, 4)$ whose mantles are given by the following prescription

$$\vartheta = \vartheta_i \quad \text{on} \quad \partial V_i \ \ (i = 3, 4). \tag{4.1}$$

The meridian section of this body of rotation is shown in Figure 3.

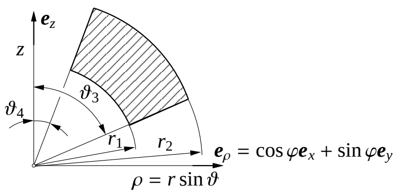

Figure 3. Meridian section of body of rotation

The surface forces on ∂V_3 and ∂V_4 are given by

$$\widetilde{\boldsymbol{p}}_3 = -p_3 \boldsymbol{e}_\vartheta, \qquad \widetilde{\boldsymbol{p}}_4 = p_4 \boldsymbol{e}_\vartheta \quad p_3 \text{ and } p_4 \text{ are constants,} \quad (p_3 > 0,\ p_4 > 0). \tag{4.2}$$

It is easy to show that the solvability condition (2.15) for this boundary value problem is fulfilled since

$$-\int\limits_{\partial a_3} p_3 \boldsymbol{e}_r \times \boldsymbol{e}_\vartheta \,\mathrm{d}s_3 + \int\limits_{\partial a_4} p_4 \boldsymbol{e}_r \times \boldsymbol{e}_\vartheta \,\mathrm{d}s_4 = -p_3 \sin\vartheta_3 \int\limits_0^{2\pi} \boldsymbol{e}_\varphi \,\mathrm{d}\varphi + p_4 \sin\vartheta_4 \int\limits_0^{2\pi} \boldsymbol{e}_\varphi \,\mathrm{d}\varphi = \boldsymbol{0}. \tag{4.3}$$

If take into account that Example 4.1 is an axially symmetric statical boundary value problem we can write

$$\begin{aligned} &U_\vartheta = U_\vartheta(\vartheta), \quad U_\varphi = 0, \quad \varepsilon_\vartheta = \varepsilon_\vartheta(\vartheta), \quad \varepsilon_\varphi = \varepsilon_\varphi(\vartheta), \quad \gamma_{\varphi\vartheta} = 0, \\ &\qquad \sigma_\vartheta = \sigma_\vartheta(\vartheta), \quad \sigma_\varphi = \sigma_\varphi(\vartheta), \quad \sigma_0 = \sigma_0(\vartheta), \quad \tau_{\varphi\vartheta} = 0. \end{aligned} \tag{4.4}$$

Solutions for the displacement potential are sought in the form

$$F = C\varphi, \tag{4.5}$$

where C is an arbitrary constant. By a routine computation it easy to see that the displacement potential given by equation (4.5) satisfies equations (3.22) and (3.23). In addition it follows from equations (3.17) and (3.16) that

$$\frac{\partial \sigma_0}{\partial \varphi} = 0, \quad \frac{\partial \sigma_0}{\partial \vartheta} = -2G\frac{C}{\sin\vartheta}. \tag{4.6}$$

Integration of equation (4.6) yields

$$\sigma_0(\vartheta) = -2GC\ln\left|\tan\frac{\vartheta}{2}\right| + D, \tag{4.7}$$

where D is a constant of integration. Making use of equations (3.6), (3.7), (3.8) and (4.7) we have

$$\sigma_\vartheta = -2GC\left(\frac{\cos\vartheta}{\sin^2\vartheta} + \ln\left|\tan\frac{\vartheta}{2}\right|\right) + D, \tag{4.8}$$

$$\sigma_\varphi = 2GC\left(\frac{\cos\vartheta}{\sin^2\vartheta} - \ln\left|\tan\frac{\vartheta}{2}\right|\right) + D, \tag{4.9}$$

$$\sigma_r = -2GC\ln\left|\tan\frac{\vartheta}{2}\right| + D. \tag{4.10}$$

The unknown integration constants C and D can now be calculated from the stress boundary conditions

$$\sigma_\vartheta(\vartheta_3) = -p_3, \qquad \sigma_\vartheta(\vartheta_4) = -p_4. \tag{4.11}$$

Omitting the details we get

$$C = \frac{p_3 - p_4}{2G\left[\ln\left|\frac{\tan\frac{\vartheta_3}{2}}{\tan\frac{\vartheta_4}{2}}\right| + \frac{\cos\vartheta_3}{\sin^2\vartheta_3} - \frac{\cos\vartheta_4}{\sin^2\vartheta_4}\right]}, \tag{4.12}$$

$$D = \frac{p_3\left(\frac{\cos\vartheta_4}{\sin^2\vartheta_4} - \ln\left|\tan\frac{\vartheta_4}{2}\right|\right) - p_4\left(\frac{\cos\vartheta_3}{\sin^2\vartheta_3} - \ln\left|\tan\frac{\vartheta_3}{2}\right|\right)}{\ln\left|\frac{\tan\frac{\vartheta_3}{2}}{\tan\frac{\vartheta_4}{2}}\right| + \frac{\cos\vartheta_3}{\sin^2\vartheta_3} - \frac{\cos\vartheta_4}{\sin^2\vartheta_4}}. \tag{4.13}$$

Once we know C equation (4.5) yields F. Then the non-zero displacement component u_ϑ can be obtained from (3.1):

$$u_\vartheta = u_\vartheta(r,\vartheta) = \frac{(p_3 - p_4)r}{2G\left[\ln\left|\frac{\tan\frac{\vartheta_3}{2}}{\tan\frac{\vartheta_4}{2}}\right| + \frac{\cos\vartheta_3}{\sin^2\vartheta_3} - \frac{\cos\vartheta_4}{\sin^2\vartheta_4}\right]\sin\vartheta}. \tag{4.14}$$

For $p_3 = p_4 = p$, we have

$$C = 0, \qquad D = -p, \tag{4.15}$$

$$\sigma_r = \sigma_\varphi = \sigma_\vartheta = \sigma_0 = -p, \qquad u_\vartheta = 0 \tag{4.16}$$

which represent a hydrostatic state of stresses.

The formulas derived above are used in the following numerical example:

$$\vartheta_3 = \frac{\pi}{3}, \quad \vartheta_4 = \frac{\pi}{6}, \quad G = 0.1\times 10^9\,\text{Pa (rubber)},$$

$$p_3 = 1\times 10^6\,\text{N/m}^2, \quad p_4 = 4\times 10^6\,\text{N/m}^2.$$

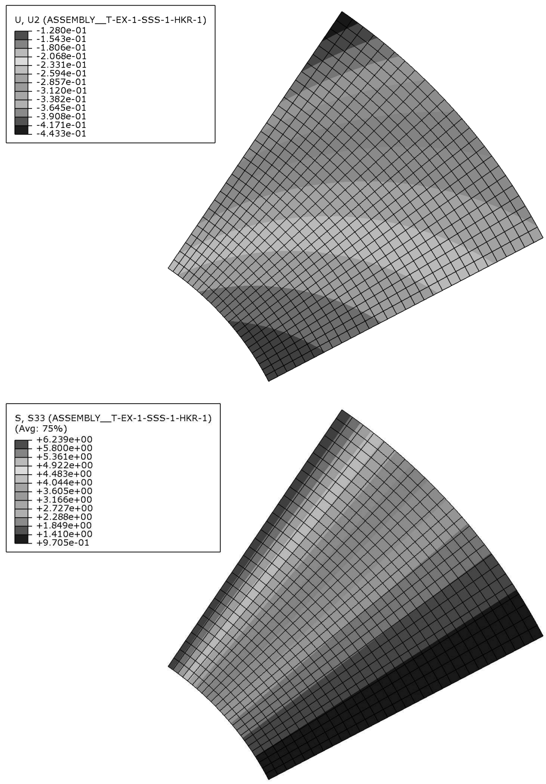

Figure 4. $\mathrm{U2} = u_\vartheta$ and $\mathrm{S33} = \sigma_\varphi$ from FEM computations

The stress values are independent of the magintude of r_i $(i = 1, 2)$. Figure 5 shows the graph of $\sigma_0 = \sigma_0(\vartheta)$, $\sigma_\vartheta = \sigma_\vartheta(\vartheta)$, $\sigma_\varphi = \sigma_\varphi(\vartheta)$. The graph of $u_\vartheta(1, \vartheta) = U_\vartheta(\vartheta)$ is shown in Figure 6.

According to equation (2.10)

$$2 \int_a \sigma_r \boldsymbol{e}_r \, \mathrm{d}a = 1.570796327 \times 10^6 \, \boldsymbol{e}_z \, \mathrm{N/m^2}, \tag{4.17}$$

$$\int_{\partial a_3} \widetilde{\boldsymbol{p}}_3 \, \mathrm{d}s_3 + \int_{\partial a_4} \widetilde{\boldsymbol{p}}_4 \, \mathrm{d}s_4 = -1.570796327 \times 10^6 \, \boldsymbol{e}_z \, \mathrm{N/m^2} \, . \tag{4.18}$$

The FEM solutions shown in Figures 4, 5 and 6 are computed by the finite element software `Abaqus` using `CAX8H`, which are 8-node biquadratic hybrid elements with linear pressure approximation.

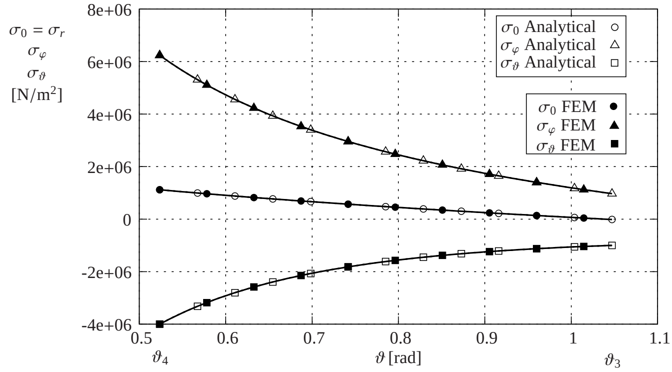

Figure 5. Graphs of normal stresses. Analytical and FEM solutions

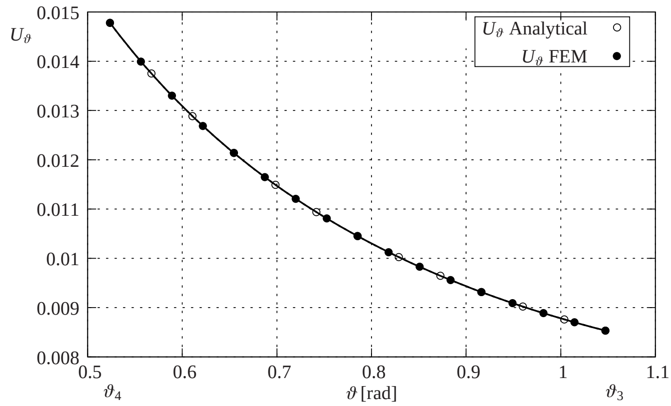

Figure 6. Graph of $u_\vartheta(1, \vartheta) = U_\vartheta(\vartheta)$

4.2 Example 2. Torsional spring. For the problem examined in this section the displacement boundary conditions on the boundary surface segment $\partial V_3 \cup \partial V_4$ are of the form

$$\boldsymbol{u} = \widetilde{\boldsymbol{u}}_3 = \boldsymbol{0} \quad \text{on} \quad \partial V_3 = \big\{(r\ \varphi,\ \vartheta)\,\big|\, r_1 \le r \le r_2,\ 0 \le \varphi \le 2\pi,\ \vartheta = \vartheta_3\big\}\,, \qquad (4.19)$$

$$\boldsymbol{u} = \widetilde{\boldsymbol{u}}_4 = r\alpha \sin\vartheta_4 \boldsymbol{e}_\varphi \quad \text{on} \quad \partial V_3 = \big\{(r,\ \varphi,\ \vartheta)\,\big|\, r_1 \le r \le r_2,\ 0 \le \varphi \le 2\pi,\ \vartheta = \vartheta_4\big\}\,. \qquad (4.20)$$

It is clear that

$$U_\vartheta = 0 \quad \text{on} \quad \partial V_3 \cup \partial V_4, \qquad (4.21)$$

$$U_\varphi = 0 \quad \text{on} \quad \partial V_3 \quad \text{and} \quad U_\varphi = \alpha \sin\vartheta \quad \text{on} \quad \partial V_4\,. \qquad (4.22)$$

Note that the solvability condition (2.17) is satisfied by the surface displacements (4.22).

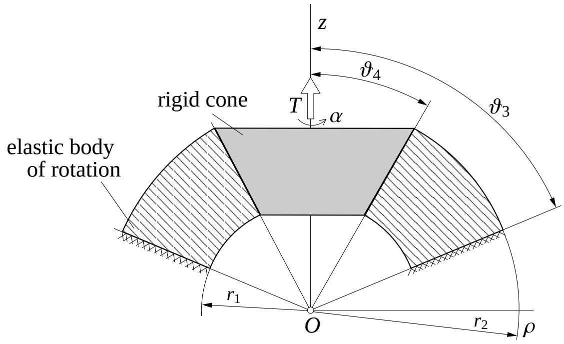

Figure 7. Example for prescribed surface displacements

Figure 7 shows the meridian section of the coupled system of an elastic-rigid body with rotational symmetry. The rigid cone is rotated by angle α about the axis z. This rotation creates that surface displacement on the boundary surface ∂V_4 which is given by equation (4.20). The rotation of the rigid cone about the axis z is produced by a torque T exerted on the cone as shown in Figure 7. Solution to the boundary value problem defined above is derived from the displacement potential

$$F(\vartheta,\, \varphi) = \frac{C_1}{2} \cos\vartheta \ln \left| \tan\frac{\vartheta}{2} \right| + C_2 \cos\vartheta. \tag{4.23}$$

It is very easy to show that in the present problem

$$L_\vartheta[F] = L_\varphi[F] = 0. \tag{4.24}$$

It follows from equation (3.1) that

$$U_\vartheta = 0, \tag{4.25}$$

$$U_\varphi = \frac{C_1}{2} \left(\sin\vartheta \ln \left| \tan\frac{\vartheta}{2} \right| - \cot\vartheta \right) + C_2 \sin\vartheta. \tag{4.26}$$

With U_φ equations (1.2) and (1.3) yield

$$\varepsilon_\vartheta = \varepsilon_\varphi = 0, \qquad \gamma_{\varphi\vartheta} = \frac{C_1}{\sin^2\vartheta}. \tag{4.27}$$

A combination of equations (1.4), (1.5), (1.6), (1.9) and (4.2) with equations (4.27) results in the stresses:

$$\sigma_r = \sigma_\vartheta = \sigma_\varphi = \sigma_0 = D = \text{constant}. \tag{4.28}$$

The equilibrium condition for the rigid circular cone leads to the equation

$$\sigma_\vartheta = D = 0. \tag{4.29}$$

Figure 8 is the free-body diagram of the rigid cone. Note that equation (4.29) is a consequence of the force equilibrium in the direction of the axis z.

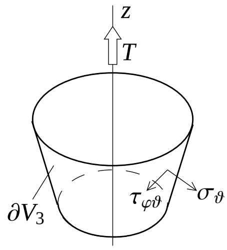

Figure 8. Free-body diagram of the rigid cone

The integration constants C_1 and C_2 are obtained from the displacement boundary conditions $(4.22)_{1,2}$. A detailed computation yields

$$C_1 = \frac{H_1}{H}, \qquad C_2 = \frac{H_2}{H}, \tag{4.30}$$

where

$$H = 2\sin\vartheta_3\left(\sin\vartheta_4 \ln\left|\tan\frac{\vartheta_4}{2}\right| - \cot\vartheta_4\right) - 2\sin\vartheta_4\left(\sin\vartheta_3 \ln\left|\tan\frac{\vartheta_3}{2}\right| - \cot\vartheta_3\right), \tag{4.31}$$

$$H_1 = 4\alpha\sin\vartheta_3\sin\vartheta_4, \tag{4.32}$$

$$H_2 = -2\alpha\sin\vartheta_4\left(\sin\vartheta_3\ln\left|\tan\frac{\vartheta_3}{2}\right| - \cot\vartheta_3\right). \tag{4.33}$$

Making use of equations (3.9) and (4.27), $(4.30)_1$, (4.31) then equation (4.32), we get the shearing stress:

$$\tau_{\varphi\vartheta} = \frac{2\alpha G}{(h(\vartheta_4) - h(\vartheta_3))\sin^2\vartheta}, \tag{4.34}$$

where

$$h(\vartheta) = \ln\left|\tan\frac{\vartheta}{2}\right| - \frac{\cos\vartheta}{\sin^2\vartheta}. \tag{4.35}$$

Relationship between the applied torque and the prescribed angular displacement α can be derived from the moment equilibrium equation:

$$T + 2\pi\int_{r_1}^{r_2} \tau_{\varphi\vartheta} r^2 \sin\vartheta \,\mathrm{d}r = 0\,. \tag{4.36}$$

Omitting the details we get

$$T = R\alpha, \qquad R = \frac{4}{3}\pi G\frac{r_2^3 - r_1^3}{h(\vartheta_3) - h(\vartheta_4)}. \tag{4.37}$$

Figures 10 and 11 show the graph of functions $\tau_{\vartheta\varphi} = \tau_{\vartheta\varphi}(\vartheta)$ and $u_\varphi(1,\vartheta) = U_\varphi(\vartheta)$. The following data were used $\vartheta_3 = \frac{\pi}{2}$, $\vartheta_4 = \frac{\pi}{6}$, $G = 10^8\,\mathrm{N/m^2}$, $\alpha = 10^{-2}\,\mathrm{rad}$, $r_1 = 0.01\,\mathrm{m}$, $r_2 = 0.02\,\mathrm{m}$. In this example

$$R = 613.28522\,\mathrm{Nm}, \qquad T = 6.1328522\,\mathrm{Nm}.$$

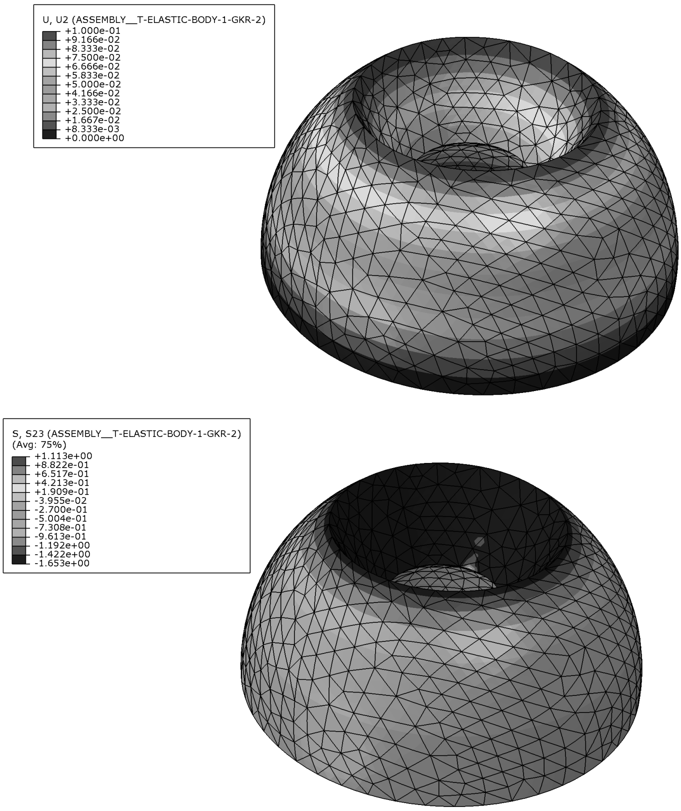

Figure 9. $U2 = u_\varphi$ and $S23 = \tau_{\varphi\vartheta}$ from FEM computations

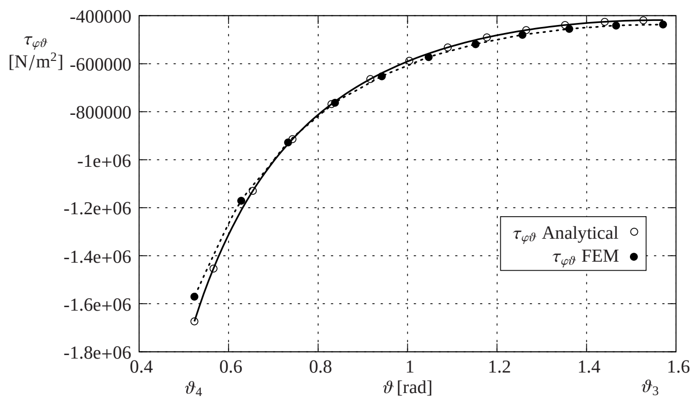

Figure 10. Analytical and FEM solutions for the shearing stresses

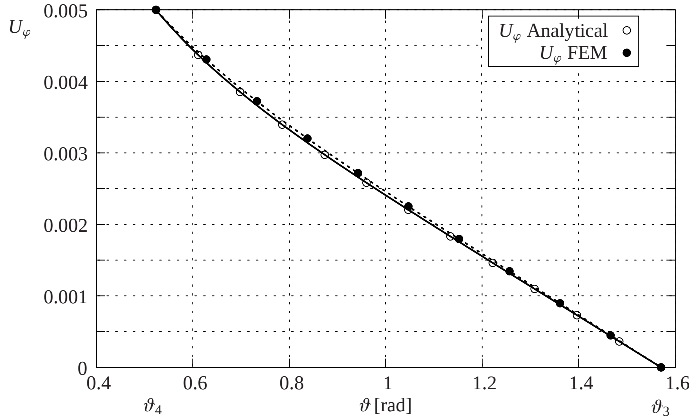

Figure 11. Analytical and FEM solutions for $u_\varphi(1, \vartheta) = U_\varphi(\vartheta)$

The results of FEM computation are represented in Figure 9. Figures 10 and 11 show the comparison of the analytical and FEM solutions. The latter are computed by the finite element software `Abaqus` using the 10-node quadratic tetrahedron hybrid finite element `C3D10H` with constant pressure approximation.

5. Conclusions

In this paper the static equilibrium of an elastic body made of incompressible and homogeneous material is investigated. We have assumed that the body considered is bounded by two spherical and two conical surfaces. We have introduced a new concept called spherical strain state (SSS). If a body is in SSS the strains and stresses are independent of the radial coordinate in a properly chosen spherical coordinate system.

The present paper is a contribution to the existing exact benchmark solutions for incompressible elastic bodies. The analytical results we have obtained for the two examples are compared with finite element solutions. They are in excellent agreement.

The Poisson number for the finite element solutions, which are computed by the software `Abaqus`, is $\nu = 0.499999$ for both examples.

Acknowledgment

This research was (partially) carried out in the framework of the Center of Excellence of Innovative Engineering Design and Technologies at the University of Miskolc and supported by the National Research, Development and Innovation Office - NKFIH, K115701.

References

1. Babuska, I. and Suri, M.: *Locking Effects in the Finite Element Approximation of Elasticity Problems.* Technical Note BN-1119. Institute for Physical Science and Technology University of Maryland, 1990.
2. Szabó, B. and Babuška, I.: *Finite Element Analysis.* John Wiley, New York, 1991.
3. Gurtin, M. E.: *The Linear Theory of Elasticity in Handbuch der Physik.* VI/2. (Ed. Flüge. S.) Springer, Berlin, 1972.
4. Slaughter, W. E.: *The Linearized Theory of Elasticity.* Birkhäuser, Boston, 2001.
5. Sokolnikoff, I. S.: *Mathematical Theory of Elasticity.* (2nd ed.) McGraw-Hill, New York, 1956.

Journal of Computational and Applied Mechanics, Vol. 11., No. 1., (2016), pp. 33–48
DOI: 10.32973/jcam.2016.003

COMPARISONS OF WELDED STEEL STRUCTURES DESIGNED FOR MINIMUM COST

József Farkas
Institute of Logistics, University of Miskolc
H-3515 Miskolc, Miskolc–Egyetemváros, Hungary
altfar@uni-miskolc.hu

[Received: February 2, 2016. Accepted: April 10, 2016]

Abstract. Cost is an important characteristic of welded structures, since welding is an expensive fabrication technology. The developed cost calculation method enables designers to predict the cost of material, assembly, welding and painting costs in the design stage. Cost comparison can select the most economical structural version. Since only optimized versions can be compared to each other realistically, a minimum cost design procedure should be performed for each version.

In the present study cost comparisons are discussed for the following welded structures: (a) a cantilever column constructed from stringer-stiffened circular cylindrical shell as well as from square box section with stiffened or cellular plates, (b) a stiffened or cellular plate supported at four corners, (c) a wind turbine tower constructed as a ring-stiffened slightly conical circular shell or as a tubular truss, (d) a ring-stiffened slightly conical shell with equidistant or non-equidistant stiffening.

Keywords: Structural optimization, welded steel structures, cost calculations, stiffened and cellular plates, conical shells

1. Introduction

Comparisons of main structural characteristics help designers to select the best versions. The large selection of structural types made from welded plates or profiles enables designers to construct load-carrying engineering structures, which fulfil not only the constraints on safety and fabrication, but also are economic. Economy is an important requirement, since welding is an expensive fabrication technology.

In order to characterize the economy of structural versions we have developed a cost calculation method mainly adaptable for welded steel structures in the design phase. Based on this cost function we have worked out a number of optimization problems for different structural types. Realistic numerical models have been used to show how to construct safe, fit for production and economic welded structures.

We have used cost comparisons in many optimization problems to find the minimum cost version. In the present paper the results of these minimum cost design studies are collected to make cost comparisons useful for designers in selecting the most suitable and competitive structural versions. Since only optimized versions can be realistic compared to each other, each version is optimized for minimum cost.

Since the detailed studies of these problems have already been published, only the main characteristics, results and discussion of the cost differences are presented here.

2. The cost calculation method

The general formula for the welding cost is as follows [1–4]:

$$K_w = k_w \left(C_1 \Theta \sqrt{\kappa \rho V} + 1.3 \sum_i C_{wi} a_{wi}^n C_{pi} L_{wi} \right) \tag{1}$$

where k_w [\$/min] is the welding cost factor, C_1 is the factor for the assembly usually taken as $C_1 = 1$ min/kg$^{0.5}$, Θ is the factor expressing the complexity of assembly, the first member calculates the time of the assembly, κ is the number of structural parts to be assembled, V is the volume, ρV is the mass of the assembled structure, the second member estimates the time of welding, C_w and n are the constants given for the specified welding technology and weld type.

Furthermore C_{pi} is the factor for the welding position (download 1, vertical 2, overhead 3), L_w is the weld length, the multiplier 1.3 takes into account the additional welding times (deslagging, chipping, changing the electrode).

Material cost is calculated as

$$K_m = k_m \rho V, \qquad k_m = 1.0 \text{ \$/kg} \tag{2}$$

where V is the volume of a structural part. The painting cost is

$$K_P = k_P S, \qquad k_P = 28.8 \times 10^{-6} \text{ \$/mm}^2 \tag{3}$$

in which S is the surface to be painted.

3. A column in compression and bending with a constraint on top sway

This structural component is used in buildings and piers of highways. Since during the large earthquake in Kobe in 1995 many highway piers were destroyed by too large horizontal seismic forces, Japanese researchers have made great efforts to work out advanced seismic-resistant structural versions. Although our studies do not contain earthquake loads, our results can be applied in the design of seismic-resistant structural versions.

We have optimized three structural versions using the same column height, loads, constraints and similar cost calculations.

3.1. Column constructed as a stringer-stiffened circular cylindrical shell.

The investigated structure is a supporting column loaded by an axial and horizontal force (Figure 1). The horizontal displacement of the top is limited for serviceability of the supported structure. Both the stiffened and unstiffened shell versions are optimized and their cost is compared to each other. In the stiffened shell outside longitudinal stiffeners of halved rolled I-section (UB) are used. The cost function is formulated according to the fabrication sequence.

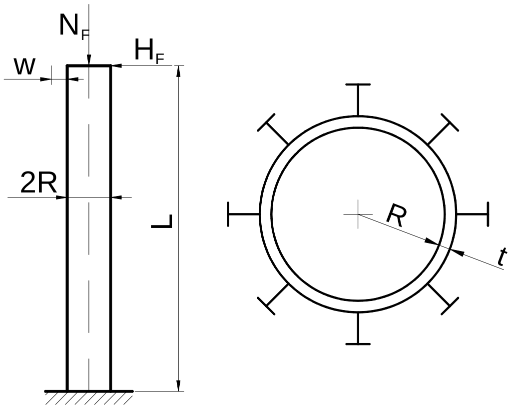

Figure 1. A cantilever column and its cross-section of stringer-stiffened circular cylindrical shell

Numerical data: The vertical load $N_F = 34000$ kN, the horizontal force $H_F = 0.1N_F$, the yield stress $f_y = 355$ MPa, $R = 1850$ mm, $L = 15$ m. The discrete values of h and the nominal size of I-beam (UB)(in the parenthesis) are as follows according to the ARCELOR catalog: 152.4 (152), 177.8 (178), 203.2 (203), 257.2 (254), 308.7 (305), 353.4 (356), 403.2 (406), 454.6 (457), 533.1 (533), 607.6 (610), 683.5 (686), 762.2 (762), 840.7 (838), 910.4 (914), 1008.1 (1016) mm. The main dimensions of some UB profiles are given in Table 3. Cost K is given in USD ($) throughout the paper.

Table 1. Results of the optimization for stiffened and unstiffened shell. The positive cost difference means savings due to stiffening. Stiffener height (h) and shell thickness (t) in mm, cost (K) in $

Stiffened					Unstiffened		Cost difference
ϕ	h	n	t	K	t	K	
400	203	5	24	56,310	22	49480	-14
500	610	5	22	56,082	22	49,480	-13
600	406	5	23	55,760	25	55,800	0
700	686	14	16	57,751	29	64,440	12
800	914	10	16	62,294	33	73,370	18
900	914	15	12	66,545	37	82,580	24
1000	914	18	11	70,571	41	92,100	30

Constraints on shell buckling (unstiffened curved panel buckling) and stringer panel buckling are formulated according to DNV design rules. Horizontal displacement on the top is limited to $L/\phi = L/400$–$L/1000$.

The optimization is performed using the Particle Swarm mathematical algorithm [4]. The results are summarized in Table 1.

The buckling stress constraint is active when the allowable horizontal displacement is L/400 – L/500 and for these cases the unstiffened shell is cheaper than the stiffened one. On the other hand, for $L/700 - L/1000$ the displacement constraint is active and the stringer-stiffened shell is cheaper than the unstiffened one. The cost savings achieved by stiffening are 12-30%.

3.2. **Columns of square box section constructed from stiffened or cellular plates.** A cantilever stub column of square box section is optimized. The column is subject to compression and bending and is constructed from four equal orthogonally stiffened and cellular side plates. The thickness and width of side plates as well as the dimensions and numbers of longitudinal stiffeners are calculated to fulfill the constraints and minimize the cost function.

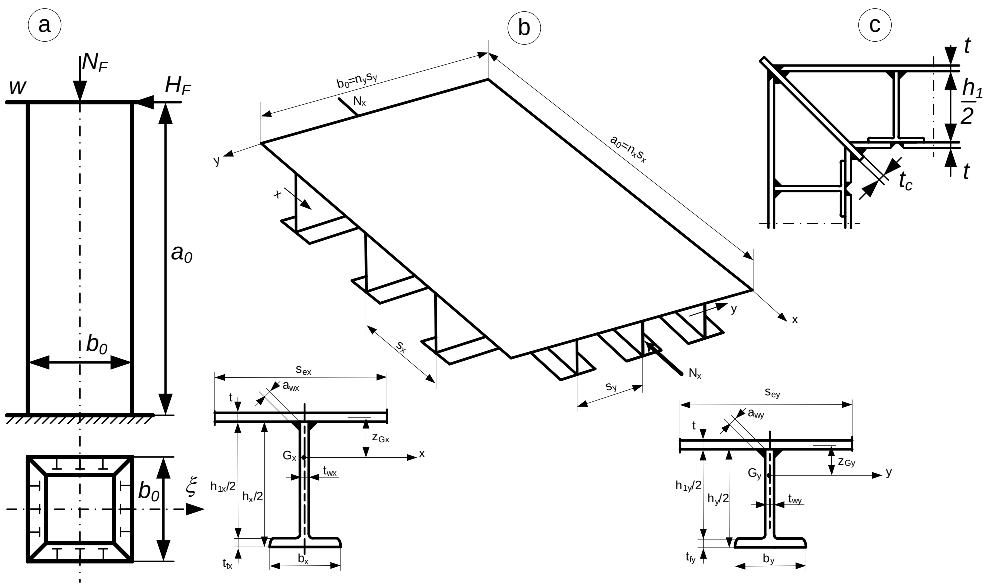

Figure 2. A cantilever column can be constructed of stiffened or cellular plates. (a) Main dimensions and loads, (b) orthogonally stiffened plate, (c) corner construction with cellular plates

The constraints on overall buckling are formulated according to the Det Norske Veritas design rules [5]. The horizontal displacement of the column top is limited. The minimum distance between stiffeners is prescribed to ease the welding of stiffeners to the base plates.

Halved rolled I-profile stiffeners are used. Their height characterizes the whole profile, since the other dimensions can be expressed by height using approximate functions derived from the data of a profile series selected from available sections.

The cost function is formulated according to the fabrication sequence.

It is possible to compare the costs of structural versions of the column with the same height, loads and constraints on stress and displacement as follows.

(1) The stringer-stiffened circular shell with a radius of 1850 mm has the minimum cost of $K = 70571$ (unstiffened $K = 92,100$ \$),
(2) The square box structure composed from orthogonally stiffened plates with an optimized width of $b_0 = 4500$ mm has the minimum cost of $K = 76,990$ \$ (see [4]),
(3) The cellular box structure loaded by a slightly different compression force (30000 instead of 34000 kN) with an optimized width of $b_0 = 4700$ mm has the minimum cost of $K = 60,430$ \$.

It can be concluded that the cellular box column is the most economic structural version, since cellular plates have much higher torsional stiffness that the plates stiffened on one side.

4. Stiffened or cellular square plates supported at four corners

4.1. **The stiffened square plate.** A square plate is investigated subject to uniformly distributed normal static load, supported at four corners, stiffened by a square symmetrical orthogonal grid of ribs. Halved rolled I-section stiffeners are used welded to the base plate by double fillet welds (Figure 3) [4,6].

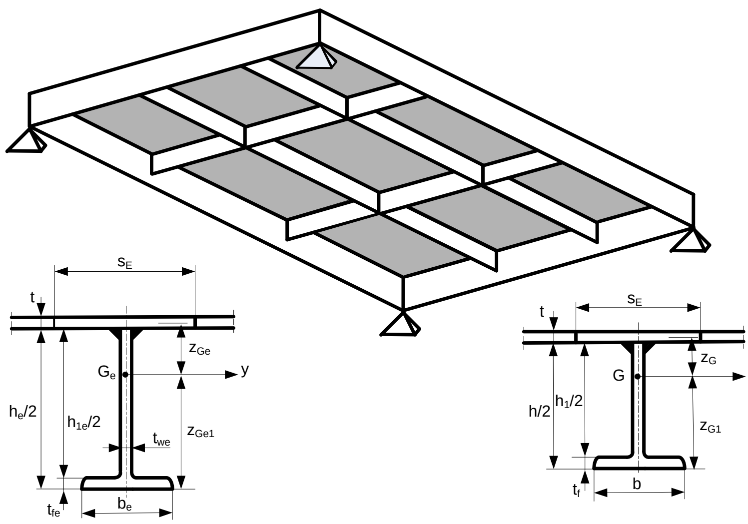

Figure 3. A stiffened square plate supported at four corners. Cross-sections of external (a) and internal (b) stiffeners of halved rolled I-section

The bending moments are calculated using the force method for torsionless gridworks with different numbers of stiffeners. Constraints on stress in the base plate and in stiffeners as well as on deflection of edge beams and of internal stiffeners are formulated. The cost function includes material, welding and painting costs and is formulated according to the fabrication sequence.

The unknowns are the base plate thickness (t), the heights of edge (h_e) and internal (h) stiffeners and the number of internal stiffeners (n).

Numerical data: Yield stress of steel $f_y = 355$ MPa, $f_{y1} = f_y/1.1 = 322$, elastic modulus $E = 2.1 \times 10^5$ MPa, edge length of the base plate $L = 18.0$ m, factored load intensity $p_0 = 0.0015$ N/mm^2, load intensity considering the self mass

$$p = p_0 + \rho_0 \frac{V}{L^2}, \tag{4}$$

where density of steel $\rho = 7.85 \times 10^{-6}$ kg/mm^3, $\rho_0 = 7.85 \times 10^{-5}$ N/mm^3, admissible deflection $w_{adm} = L/300 = 60$ mm, factor for the complexity of assembly $\Theta = 3$, factor for the complexity of painting $\Theta_F = 3$, cost factors: $k_m = 1.0$ \$/kg, $k_w = 1.0$ \$/min, $k_P = 14.4 \times 10^{-6}$ \$/mm^2. The ranges of unknowns: $t = 4$–40 mm, h and $h_e = 152$–1008.1 mm.

Results obtained for discrete variables are summarized in Table 2.

Table 2. Results obtained by Particle Swarm Optimization for discrete variables. Dimensions and deflections in mm, stresses in the external fibres for edge and internal stiffeners in MPa, costs (K) in \$. The minimum cost is marked by bold letters

n	h_e	h	t	σ_{e1}	σ_e	σ_1	σ	w_e	w	K
3	1016	607.6	14	208	310	112	106	36.1	47.6	118,500
4	1016	607.6	9	109	286	205	285	51.6	51.7	**106,800**
5	1008.1	762.2	12	142	233	301	299	45.9	42.7	134,200

4.2. **The cellular square plate.** Cellular plates can be applied in various structures e.g. in floors and roofs of buildings, in bridges, ships, machine structures, etc. Cellular plates have the following advantages over the plates stiffened on one side: (a) because

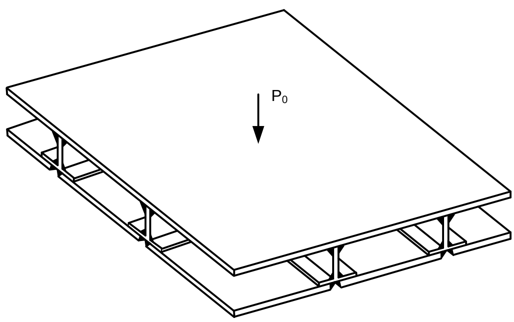

Figure 4. A square cellular plate

of their large torsional stiffness the plate thickness can be decreased, which results in a decrease in welding cost, (b) their planar surface is more suitable for corrosion protection, (c) their symmetric welds do not cause residual distortion.

In a previous study [7] it was shown that cellular plates can be calculated as isotropic ones and bending moments and deflections can be determined by using classic results of isotropic plates for various load and support types.

In the present study a cellular plate is designed which is supported at four corners and subject to a uniformly distributed normal load.

In order to guarantee a suitable fabrication procedure halved rolled I-section stiffeners are used, their web is welded to the upper base plate by double fillet welds and the bottom base plate parts are welded to the stiffener flanges also by fillet welds (Figure 4).

Structural characteristics to be changed (variables):

- number of stiffeners in one direction (square symmetry) n,
- thicknesses of the upper and bottom base plates t_1 and t_2,
- height of the rolled I-section stiffener h.

Other dimensions of UB profiles are given in Table 3. Note that for these dimensions approximate formulae can be applied as well.

Available series of rolled I-sections: UB profiles selected according to the ARCELOR catalog [8] (necessary for the optimization).

Table 3. Selected UB profiles according to the ARCELOR catalogue

UB profile	h	b	t_w	t_f
610 × 229 × 113	607.6	228.2	11.1	17.3
686 × 254 × 140	683.5	253.7	12.4	19.0
762 × 267 × 173	762.2	266.7	14.3	21.6
838 × 292 × 194	840.7	292.4	14.7	21.7
914 × 305 × 224	910.4	304.1	15.9	23.9
1016 × 305 × 349	1008.1	302.0	21.1	40.0

Numerical data: Plate edge length: $L = 18$ m, factored load intensity $p_0 = 150$ kg/m^2 = 0.0015 N/mm^2, yield stress of steel $f_y = 355$ MPa, elastic modulus $E = 2.1 \times 10^5$ MPa, Poisson ratio $\nu = 0.3$, steel density $\rho = 7.85 \times 10^{-6}$ kg/mm^3, $\rho_0 = 7.85 \times 10^{-5}$ N/mm^3.

Optimization and results: In the optimization process the optimum values of variables are sought that fulfil the design and fabrication constraints and minimize the cost function. Calculation shows that the deflection constraint is always active, and the minimum cost corresponds to the minimum value of plate thickness $t_2 = 4$ mm. The results are summarized in Table 4.

It can be seen that the cost increases when h decreases, thus it is not necessary to continue with the search. The optimum is marked by bold letters. Each result given in Table 4 satisfies all the constraints.

Table 4. Optimization results. Allowable deflection is 60 mm. Dimensions and deflections in mm, stresses in MPa

h	n	t_1	t_2	σ_2	$w_{\max}$	$10^{-5}K$ \$
1008.1	3	8	7	191	57.2	1.125
	4	7	4	122	57.2	1.071
	5	**5**	**4**	**166**	**59.6**	**1.061**
	6	4	4	191	56.8	1.094
910.4	3	12	4	65	57.6	1.158
	4	10	4	60	59.1	1.121
	5	9	4	51	56.9	1.129
840.7	3	14	4	47	57.7	1.232
	4	12	4	41	58.4	1.188
	5	11	4	34	56.0	1.191
	6	10	4	30	55.0	1.195
	7	9	4	29	55.2	1.200

Comparing the two structural versions it can be concluded that the cellular plate is competitive to the plate stiffened on one side, since the costs are nearly the same (106,800 compared to 106,100 $) and the cellular construction has some advantages over the stiffened one.

5. A wind turbine tower

Steel towers for wind turbines can be constructed in various structural versions. Ring-stiffened cylindrical shells or tubular trusses are usually applied.

The cost comparison is applied now to two structural versions of a wind turbine tower. The tower is 45 m high, loaded on the top by a factored vertical force of 950 kN (self weight of the nacelle), a bending moment of 997 kNm and a horizontal force of 282 kN from the turbine operation. The tower width is limited to 2.5 m due to the rotating turbine blades of length 27 m.

Both the shell and the truss structure are constructed from 3 parts each of 15 m length with stepwise increasing widths. The shell parts are designed against shell buckling and panel ring buckling according to the design rules of the Det Norske Veritas [5]. The number of flat ring stiffeners is determined by the designer to avoid larger ovalization of the cylindrical shell. The 3 shell parts are joined by bolted connections.

5.1. **The ring-stiffened shell structure.** Design constraints on shell buckling and on local buckling of flat ring-stiffeners are formulated according to DNV [5] and API [9] design rules. The wind load acting on the shell tower is calculated according to Eurocode 1 Part 2-4 [10]. To avoid shell ovalization a minimum number of 5 and a maximum number of 15 stiffeners is prescribed. In the shell buckling constraint an imperfection factor as proposed by Farkas [3] is used, which expresses the effect of radial shell deformation due to shrinkage of circumferential welds.

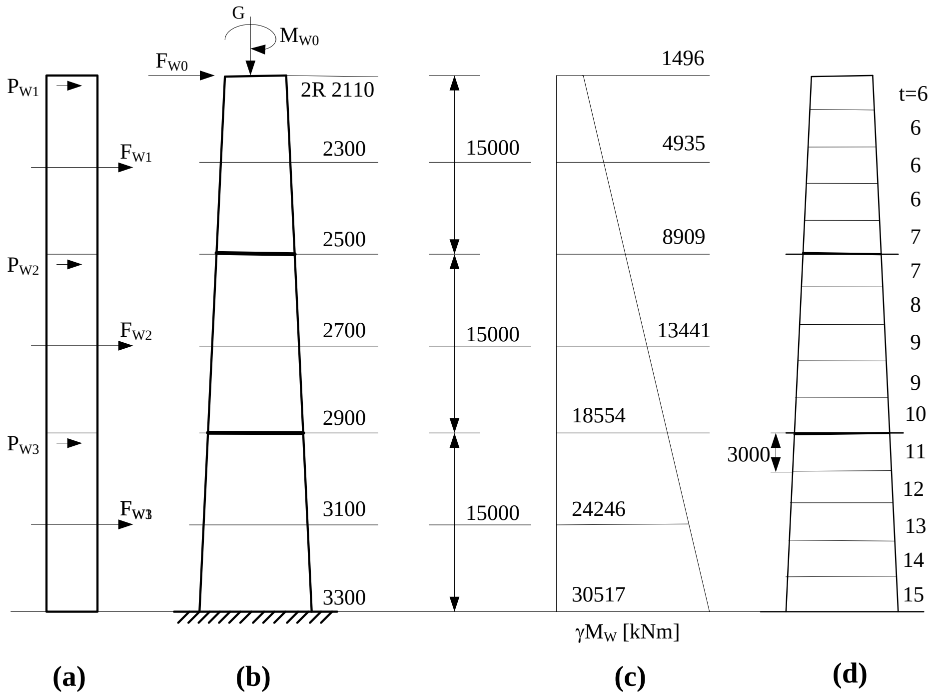

Figure 5. A wind turbine tower constructed as a ring-stiffened circular slightly conical shell. (a) wind loads, (b) diameters of the shell, (c) bending moments, (d) shell thicknesses

The optimization has been performed using Rosenbrock's search algorithm [1]. The optimal values of the shell thickness (t) for $n = 5$, which comply with the design constraints and minimize the cost function, are given in Figure 5d. The minimal masses and costs are summarized in Table 5.

Table 5. Summary of masses (kg) and costs ($)

Shell part	Mass	Cost without K_p	K_p	Total K
top	5398	12096	6440	18,536
middle	9472	19772	7603	27,373
bottom	15648	30941	8778	39,719
total	30518	62809	22821	85,628

5.2. **The tubular truss structure.** The truss is statically determinate. The distance between parallel chords in the upper part of the tower is limited because of the rotating blades (Figure 6).

Thus, in the optimization procedure the inclination angle or the larger constant chord distance and the member dimensions of the lower tower part are sought that minimize the structural volume and fulfill the design constraints.

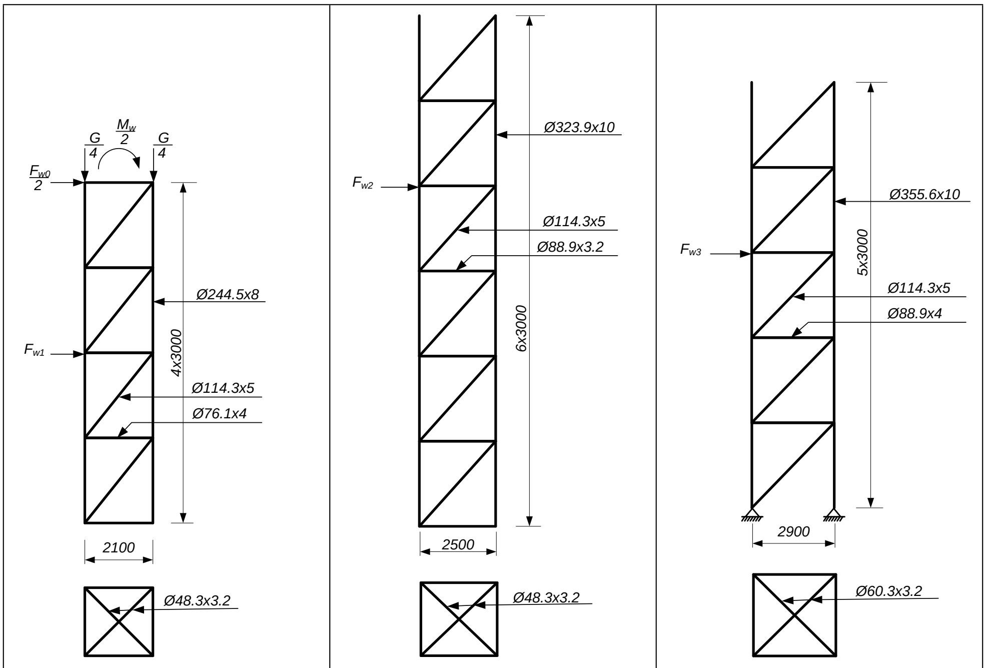

Truss of the top tower part	Truss of the middle tower part	Truss of the bottom tower part

Figure 6. A wind turbine tower constructed as a tubular truss

The constraints relate to the buckling strength of circular hollow section (CHS) members and to the local strength of welded tubular joints. Seismic behavior is not considerred. In the numerical problem the loads from wind acting on the turbine and from the nacelle mass are selected from the literature. With the member forces an iterative suboptimization method is used for the calculation of compression member dimensions.

The cross-section of the truss can be quadratic or triangular. In the case of a triangular cross-section the whole horizontal load should be carried by a truss plane, since the horizontal load direction is variable. Therefore the quadratic cross-section is used. In this case only the half value of the horizontal load is acting on a truss plane.

The tubular truss structure consists of three parts with different but constant width. The four truss planes are stiffened by horizontal diaphragms constructed from two struts.

Both structural versions are checked for eigenfrequency and fatigue [11]. The details of the cost calculation are summarized in Table 6, where G – mass, K_m – material cost, K_{CG} – cost of cutting and grinding of the tubular member ends, K_A – cost of assembly, K_w – cost of welding, K_P – cost of painting, K – total cost.

Table 6. Costs in \$ of the tubular tower, the surface A_P to be painted in mm^2

Part	G kg	K_m	K_{CG}	K_A	K_w	$A_{Px}10^{-6}$	K_P	K
Top	3437	4139	1936	1180	2514	72.46	2087	11,856
Middle	7395	9096	2867	1965	3108	130.11	3747	20,783
Bottom	6701	8643	2551	1629	2353	116.17	3346	18,522
Total	17533	21878	7354	4774	7975	318.74	9180	51,161

The comparison of the two structural versions (Tables 5 and 6) shows that the tubular truss has smaller mass (17533 compared to 30518 kg), smaller surface to be painted and is much cheaper than the shell structure (51,161 compared to 85,628 \$). This difference is caused by the much lower mass and surface of the tubular truss version.

6. A ring-stiffened slightly conical shell loaded by external pressure

Conical shells are applied in numerous structures, e.g. in submarine and offshore structures, aircraft, tubular structures, towers and tanks, etc. Their structural characteristics

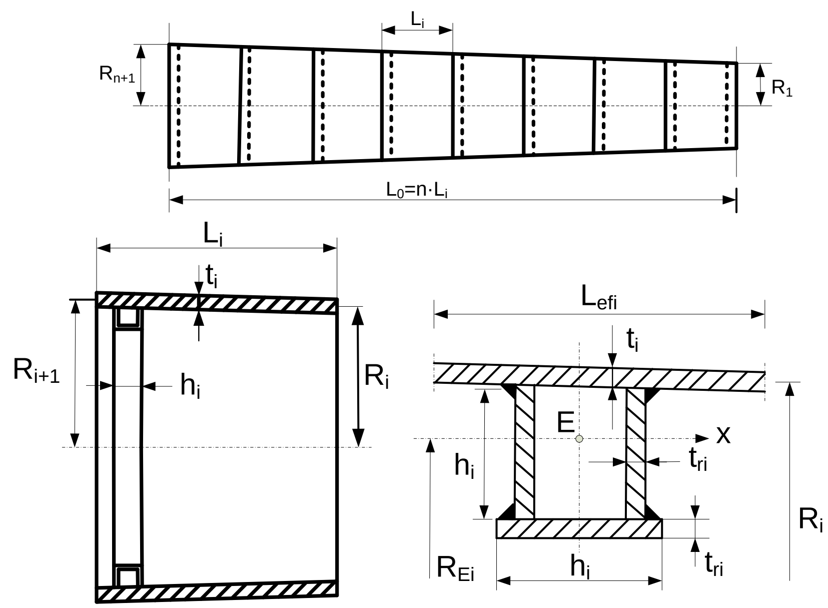

Figure 7. A ring-stiffened slightly conical shell with equidistant stiffening. Ring stiffener of welded box section

are as follows:

- Material: steels, Al-alloys, fiber-reinforced plastics.
- Geometry: slightly conical (transition parts between two circular shells), strongly conical (storage tank roofs), truncated.
- Stiffening: ring-stiffeners, stringers, combined, equidistant, non-equidistant.

- Stiffener profile: flat, box, T-, L-, Z-shape,
- Loads: external pressure, axial compression, torsion, combined.
- Fabrication technology: welding, riveting, bolting, gluing.

In the present study we select the following structural characteristics: steel, slightly conical shell, ring stiffeners of welded square box section to avoid tripping, equidistant and non-equidistant stiffening, external pressure, welding. Design rules of Det Norske Veritas [5, 12] are applied for shell and stiffener buckling constraints.

In the case of equidistant stiffening the variables to be optimized are as follows: number of shell segments (n) (Figure 7), shell thicknesses (t_i), dimensions of ring-stiffeners (h_i, t_{ri}). The number of stiffeners is n+1, since stiffeners should be used at the ends of the shell, thus, two stiffeners are used in the first shell segment.

In the case of non-equidistant stiffening [13] the variables to be optimized are as follows: length of shell segments for a given shell thickness (Figure 1), dimensions of ring-stiffeners (h_i, t_{ri}). The ring stiffeners are placed at a small distance from the circumferential welds connecting two segments to allow the inspection of welds: this is marked in Figure 1 by dotted lines.

The optimization process for the equidistant stiffening has the following parts:

(a) design of thicknesses for each shell segment given by two radii (R_i and R_{i+1}) using the shell buckling constraint,
(b) design of ring stiffeners for each shell segment using the stiffener buckling constraint,
(c) cost calculation for each shell segment and for the whole shell structure.

These design steps should be carried out for a series of segment numbers. On the basis of calculated costs the optimum solution corresponding to the minimum cost can be determined.

The optimization process for the non-equidistant stiffening has the following parts:

(d) design of each shell segment length for a given shell thickness using the shell buckling constraint,
(e) design of ring stiffeners for each shell segment using the stiffener buckling constraint,
(a) cost calculation for each shell segment and for the whole shell structure.

These design steps should be carried out for a series of shell thicknesses. On the basis of calculated costs the optimum solution corresponding to the minimum cost can be determined.

Numerical data (Figure 7) : Total shell length $L = 15000$ mm, side radii $R_{\min} = R_1 = 1850$ and $R_{\max} = R_{n+1} = 2850$ mm, yield stress of steel $f_y = 355$ MPa, with a safety factor for yield stress $f_{y1} = f_y/1.1$, external pressure intensity $p = 0.5$ MPa, safety factor for loading $y_b = 1.5$, Poisson ratio $\nu = 0.3$, elastic modulus $E = 2.1 \times 10^5$ MPa.

Results of the optimization for equidistant stiffening: The detailed calculations are carried out for numbers of shell segments $n = 3 - 15$. The corresponding material and total costs are summarized in Table 7.

Table 7. The material and total costs in $ for investigated numbers of shell segments. The optima are marked by bold letters

n	3	4	5	6	8	10	12	15
K_m	48,540	43,540	40,350	36,830	33,390	31,390	**29,840**	31,192
K	85,390	82,360	81,430	**79,210**	80,260	82,120	84,811	95,818

It can be seen that the optimum number of shell segments for material cost is $n_{\text{Mopt}} = 12$ and for total cost $n_{\text{opt}} = 6$. This difference is caused by the fact that the fabrication (assembly, welding and painting) cost represents a large amount of total cost. The cost data show that forming the plate elements into shell shape, welding and painting make up a significant part of the fabrication cost.

In order to characterize the dimensions of the optimum structure, the main data are given in Table 8.

Table 8. Main dimensions (in mm) of the optimum shell structure

i	R_i	t_i	h_i	t_{ri}
1	1850	18	121	4
2	2017	19	132	4
3	2184	20	143	5
4	2351	20	156	5
5	2518	21	155	5
6	2685	22	153	5
7	2852	23	152	6

Results of the optimization for non-equidistant stiffening: The detailed calculations are carried out for shell thicknesses $t_i = 14 - 20$ mm. The corresponding material and total costs are summarized in Table 9.

Table 9. The material and total costs in $ for investigated shell thicknesses. The optima are marked in bold letters

t_i	K_m	K
14	**28,490**	82,280
16	29,620	76,150
18	32,390	**75,040**
20	38,170	80,120

It can be seen that the optimum shell thickness for material cost is 14 and for total cost 18 mm. This difference is caused by the fact that the fabrication (assembly, welding and painting) cost represents a large amount of total cost. The cost data show that forming the plate elements into shell shape, welding and painting make up a significant part of the fabrication cost.

In order to characterize the dimensions of the optimum structure, the main data are given in Table 10.

Table 10. Main dimensions (in mm) of the optimum shell structure ($t = 18$ mm)

R_i	L_i	h_i	t_{ri}
1850	2630	121	4
2025	2376	134	4
2183	2189	146	5
2329	2044	158	5
2465	1927	170	5
2593	1831	182	6
2715	1750	194	6
2832	(1680)	207	7

Comparison of the two structural versions (Tables 9 and 10) shows that the non-equidistant stiffening produces more economic solution than that of the equidistant one: material costs 28,490 vs 29,340 \$ and total costs 75,040 vs 79,210 \$.

7. A simply supported sectorial plate with different stiffenings subject to uniformly distributed normal load

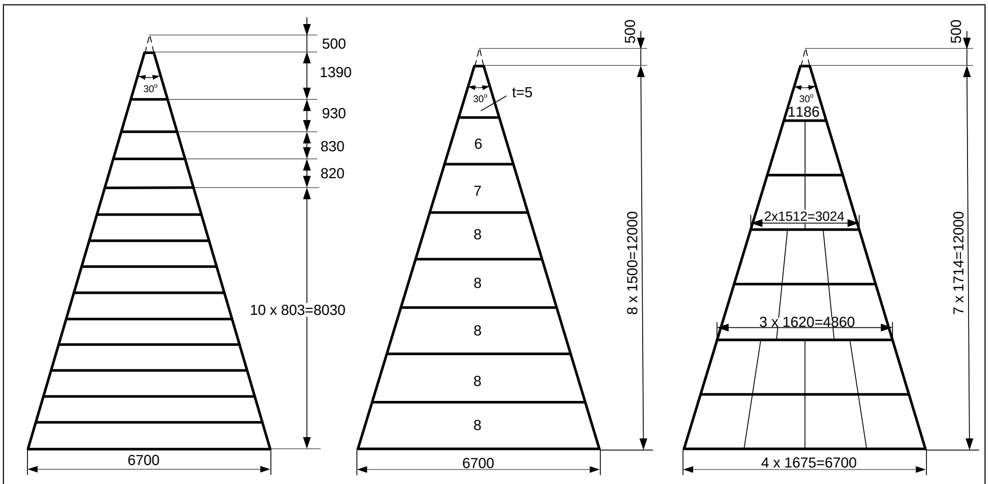

(a) Tangential non-equidistant stiffening with constant plate thickness	(b) Equidistant stiffening with stepwise varied plate thickness	(c) Combined equidistant tangential and radial stiffening

Figure 8. Stiffened sectorial plates

Halved rolled I-section stiffeners are used [14]. Comparing the costs of the different structural solutions, it can be concluded that in the present numerical problem the lowest total cost corresponds to equidistant tangential stiffening with variable base plate thickness ($n = 8$, $K = 6,320$ \$).

A similarly low total cost can be achieved by non-equidistant tangential stiffening with constant base plate thickness ($t = 4mm$, $K = 6,437$ \$).

Equidistant tangential stiffening combined with radial stiffeners needs much higher total cost ($t = 6$, $K = 7,730$ \$).

The lowest mass (or material cost) corresponds to non-equidistant tangential stiffening with constant base plate thickness ($t = 4$ mm, $K_m = 2,094$ \$) followed by combined stiffening ($t = 4$ mm, $K_m = 2,456$ \$). The solution giving the lowest total cost needs larger material cost ($n = 8$, $K_m = 3,077$ \$). These data show that the fabrication costs (welding and painting cost) significantly affect the total cost.

The comparison with the cost of the unstiffened sectorial plate shows that the stiffened version is much more economic than the unstiffened one.

8. Conclusions

The developed cost calculation method makes it possible to select the most economic structural version. Cost comparison is presented in the case of four welded steel structural types. The compared versions are optimized for minimum cost with the same conditions (loads, constraints, some main dimensions, cost calculation method).

In the case of a cantilever column loaded by compression and bending with a constraint on top sway, the square box section constructed from cellular plates is the most economic version.

A square plate supported at four corners subject to a uniform normal load can be constructed as an orthogonally stiffened plate or a cellular plate with nearly the same cost. The cellular plate is competitive to the plate stiffened on one side because of its high torsional stiffness.

The comparison of two versions of a wind turbine tower shows that the cost of a tubular truss structure is much lower than that of the slightly conical circular shell, because the tubular truss version has much lower mass and surface.

In the case of a slightly conical ring-stiffened shell subject to external pressure the non-equidistant stiffening is more economic than the equidistant one, since the shell thicknesses influence the cost significantly. For the investigated stiffened sectorial plates the lowest total cost corresponds to equidistant tangential stiffening with variable base plate thickness.

References

1. Farkas, J. and Jármai, K.: *Analysis and Optimum Design of Metal Structures.* Balkema, Rotterdam, Brookfield, 1997.
2. Jármai, K. and Farkas, J.: Cost calculation and optimization of welded steel structures. *Journal of Constructional Steel Research*, **50**, (1999), 115–135.
3. Farkas, J. and Jármai, K.: *Economic Design of Metal Structures.* Millpress, Rotterdam, 2003.

4. Farkas, J. and Jármai, K.: *Design and Optimization of Metal Structures.* Horwood Publishing, Chichester, UK, 2008.
5. Det Norske Veritas (DNV): *Buckling strength analysis.* Classification Notes No. 30. 1. Høvik, Norway. 1985.
6. Farkas, J., Jármai, K., and Snyman, J. A.: Global minimum cost design of a welded square stiffened plate supported at four corners. In *7th World Congress on Structural and Multidisciplinary Optimization*, Paper AO381. Seoul, Korea, 2007. Abstract p. 84. CD ROM.
7. Farkas, J. and Jármai, K.: Optimum design and cost comparison of a welded plate stiffened on one side and a cellular plate both loaded by uniaxial compression. *Welding in the World*, **50**(3-4), (2006), 45–51.
8. Sales program. Commercial sections. Arcelor Mittal. Long Carbon Europe. 2007.
9. American Petroleum Institute (API): Bulletin 2U. *Bulletin on stability design of cylindrical shells.* 2nd ed. Washington,. 2000.
10. Eurocode 1. Part 2-4. Wind loads. ENV 1991-2-4. 1999.
11. Farkas, J. and Jármai, K.: Cost comparison of a tubular truss and a ring-stiffened shell structure for a wind turbine tower. In J. A. Packer and S. Willibald (eds.), *Tubular Structures XI. Proc. 11th Int. Symposium and IIW Int. Conf. on Tubular Structures, Québec City, Canada*, Taylor & Francis, London, 2006, pp. 341–349.
12. Det Norske Veritas: *Buckling strength of shells.* Recommended Practice DNV-RP-C202. Høvik, Norway, 2002. 1999.
13. Farkas, J. and Jármai, K.: Minimum cost design of a conical shell – external pressure, non-equidistant stiffening. In R. O. et al. (ed.), *Eurosteel 2008 5th European Conference on Steel and Composite Structures Graz Austria. Proceedings*, Brussels, ECCS European Convention for Constructional Steelwork, Vol.B., 2008, pp. 1539–1544.
14. Farkas, J. and Jármai, K.: Minimum cost design of a welded stiffened steel sectorial plate. *Steel Construction*, **2**(2), (2009), 131–137.
15. Farkas, J. and Jármai, K.: Optimum design of a welded stringer-stiffened steel cylindrical shell subject to axial compression and bending. *Welding in the World*, **49**(5-6), (2005), 115–135.
16. Farkas, J. and Jármai, K.: Minimum cost design of a square box column composed from orthogonally stiffened welded steel plates. In J. Farkas and K. Jármai (eds.), *Design, Fabrication and Economy of Welded Structures. Int. Conf. Proc.*, Chichester, UK, Horwood Publishing, 2008, Miskolc, Hungary, pp. 61–70.

Journal of Computational and Applied Mechanics, Vol. 11., No. 1., (2016), pp. 49–66
DOI: 10.32973/jcam.2016.004

HYPERSINGULAR BOUNDARY INTEGRAL FORMULATIONS FOR PLANE ELASTICITY IN TERMS OF FIRST-ORDER STRESS FUNCTIONS

Sándor Szirbik
Institute of Engineering Mechanics, University of Miskolc
H-3515 Miskolc, Miskolc–Egyetemváros, Hungary
sandor.szirbik@uni-miskolc.hu

[Received: February 26, 2016. Accepted: April 25, 2016]

Abstract. In this paper the hypersingular integral equation method in the dual system of plane elasticity is developed and applied to mixed boundary value problems providing that the region under consideration is simply connected. The accuracy of stress calculations on the boundary is greatly increased if one applies hypersingular integral equations instead of using the traditional computational techniques of the boundary element method. In contrast to earlier results which formulate the hypersingular integral equations in the primal system of elasticity, we attack the plane problems in a dual formulation in which the stress functions of order one and the rigid body rotation are the fundamental variables. It is a further advantage of the dual formulation that the stress components can be obtained directly from the stress functions of order one. There is therefore no need for Hooke's law, which should be used when we determine the stress components on the boundary from displacements. The numerical examples presented prove the efficiency of this technique.

Mathematical Subject Classification: 74S15, 45F15
Keywords: Dual formulation, stress functions of order one, strain boundary conditions, hypersingular formulation in the dual system

1. Introduction

The theory of the boundary integral equations with hypersingular kernels in the primal system of elasticity is well developed and there are a number of problems – these include some problems of fracture mechanics – for the solution of which they are successfully applied. Guiggiani at al. [1] is, in all probability, one of the first papers devoted to this issue. The authors came to the conclusion that a deep analysis of the hypersingular formulation provides an opportunity to increase the accuracy of the stress components computed at interior points and points on the contour. Later on this technique was developed further for 2D and 3D problems in the primal system of elasticity [2–4].

The boundary integral equations of the direct method in the dual system of plane elasticity are established in [5] and [6]. These works formulate the dual boundary integral equations for plane problems in terms of stress functions of order one and the rigid body rotation.

The paper is organized into six sections. Section 2 outlines the most important preliminaries, i.e., it presents the dual integral equations of the direct method and clarifies what the boundary conditions are for the stress functions. The concept of the strain boundary conditions is also introduced. When using the direct boundary element method one has to compute weakly and strongly singular integrals. This is the main reason for obtaining partly inaccurate results for the stresses at points close to the boundary. Surprisingly the efficiency of the numerical solutions could be increased by using an appropriately chosen hypersingular formulation [1, 2]. Section 3 deals with the issue of how to introduce the hypersingular integral formulation for those boundary value problems in which the governing equations are given in terms of stress functions of order one. The necessary equations are set up in a suitable form in Section 4 which is devoted to some important computational issues so that we can develop an appropriate algorithm for the stress computations. Section 5 presents the applicability of the algorithm for a simple and a bit more difficult problem. The last section is a summary of the results. Some longer formulae are presented in Appendix A.

2. Preliminaries

Throughout this paper x_ρ and y_ρ are rectangular Cartesian coordinates referred to the same origin O. (Greek)[Latin] subscripts are assumed to have the range (1, 2)[1,2,3]. For subscripts repeated twice, the summation convention is applied. In accordance

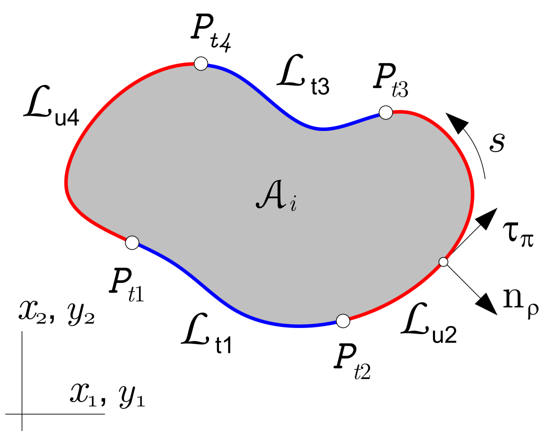

Figure 1. The inner region $\mathcal{A}_i$

with the notations introduced, $\delta_{\rho\lambda}$ is the Kronecker symbol, derivatives with respect to y_ρ are denoted by the subscript ρ preceded by a coma and $\epsilon_{\rho\pi 3}$ is the permutation symbol.

Consider a simply connected inner region $\mathcal{A}_i$. The contour $\mathcal{L}_o$ of the region can be divided into two parts denoted by $\mathcal{L}_t$ and $\mathcal{L}_u$. We shall assume that $[\mathcal{L}_t]$ $\{\mathcal{L}_u\}$ is the union of those arcs on which [stress functions (obtainable from prescribed tractions)] {strain boundary conditions (derivatives of displacements with respect to the arc coordinate)} are imposed. If the number of arcs on the boundary is four they are denoted by $\mathcal{L}_{t1}$, $\mathcal{L}_{t3}$ and $\mathcal{L}_{u2}$, $\mathcal{L}_{u4}$, respectively. The quantities that are prescribed on the boundary are denoted by hatted letters: $\hat{u}_\lambda$ and $\hat{t}_\lambda$ are the displacements and stresses (tractions) prescribed on the boundary. Let $y = (y_1, y_2)$ and $x = (x_1, x_2)$ be the source point and field point.

The three dual Somigliana formulae for the inner region are of the form

$$\mathfrak{u}_k(y) = \oint_{\mathcal{L}_o} \mathfrak{U}_{k\lambda}(x,y)\mathfrak{t}_\lambda(x)\,\mathrm{d}s_x - \oint_{\mathcal{L}_o} \mathfrak{T}_{k\lambda}(x,y)\mathfrak{u}_\lambda(x)\,\mathrm{d}s_x \qquad y \in \mathcal{A}_i\,, \tag{2.1a}$$

$$c_{\kappa\lambda}(y)\mathfrak{u}_\lambda(y) = \oint_{\mathcal{L}_o} \mathfrak{U}_{\kappa\lambda}(x,y)\mathfrak{t}_\lambda(x)\,\mathrm{d}s_x - \oint_{\mathcal{L}_o} \mathfrak{T}_{\kappa\lambda}(x,y)\mathfrak{u}_\lambda(x)\,\mathrm{d}s_x \qquad y \in \mathcal{L}_o\,, \tag{2.1b}$$

$$0 = \oint_{\mathcal{L}_o} \mathfrak{U}_{\kappa\lambda}(x,y)\mathfrak{t}_\lambda(x)\,\mathrm{d}s_x - \oint_{\mathcal{L}_o} \mathfrak{T}_{\kappa\lambda}(x,y)\mathfrak{u}_\lambda(x)\,\mathrm{d}s_x \qquad y \notin \mathcal{A}_i \cup \mathcal{L}_o\,, \tag{2.1c}$$

in which the stress functions of order one $\mathfrak{u}_\lambda$ – this vector is also referred to as dual displacement vector – and the rigid body rotation $\mathfrak{u}_3 = \varphi$ constitute the vector $\mathfrak{u}_k$,

$$[\mathfrak{U}_{kl}(x,y)] = \mathfrak{K}_1 \begin{bmatrix} -2\ln R - 3 - 2\dfrac{r_2 r_2}{R^2} & 2\dfrac{r_1 r_2}{R^2} & \dfrac{2}{\mu}(1-\nu)\dfrac{r_1}{R^2} \\ 2\dfrac{r_2 r_1}{R^2} & -2\ln R - 3 - 2\dfrac{r_1 r_1}{R^2} & \dfrac{2}{\mu}(1-\nu)\dfrac{r_2}{R^2} \\ \dfrac{2}{\mu}(1-\nu)\dfrac{r_1}{R^2} & \dfrac{2}{\mu}(1-\nu)\dfrac{r_2}{R^2} & 0 \end{bmatrix}, \tag{2.2a}$$

$$\mathfrak{K}_1 = \frac{\mu}{4\pi(1-\nu)} \tag{2.2b}$$

is the fundamental solution of order one, the distance between the points x_ρ and y_ρ is R, the position vector is defined as $r_\rho = x_\rho - y_\rho$, s is the arc coordinate on $\mathcal{L}_o$ (the positive direction on $\mathcal{L}_o$ is the one which leaves the region on the left side), $\mathfrak{t}_\lambda(x)$ stands for the derivative $-du_\lambda/ds$ taken on the boundary (here u_λ is the displacement vector) – this quantity is also referred to as the dual stress vector –, μ and ν are the shear modulus of elasticity and the Poisson number, respectively,

$$
[\mathfrak{T}_{l\lambda}(x,y)] = \mathfrak{D}(R)\begin{bmatrix} \begin{matrix} n_1 r_1\left(4\dfrac{r_2^2}{R^2}-2(3-2v)\right) \\ +n_2 r_2\left(4\dfrac{r_2^2}{R^2}-2(3-2v)\right)\end{matrix} & \begin{matrix} -n_2 r_1\left(4\dfrac{r_2^2}{R^2}+2(1-2v)\right) \\ -n_1 r_2\left(4\dfrac{r_1^2}{R^2}-2(1-2v)\right)\end{matrix} \\ \\ \begin{matrix} -n_1 r_2\left(4\dfrac{r_1^2}{R^2}+2(1-2v)\right) \\ -n_2 r_1\left(4\dfrac{r_2^2}{R^2}-2(1-2v)\right)\end{matrix} & \begin{matrix} n_2 r_2\left(4\dfrac{r_1^2}{R^2}-2(3-2v)\right) \\ +n_1 r_1\left(4\dfrac{r_1^2}{R^2}-2(3-2v)\right)\end{matrix} \\ \\ \begin{matrix} -n_1\dfrac{2}{\mu}(1-\nu)\dfrac{r_1^2-r_2^2}{R^2} \\ -n_2\dfrac{4}{\mu}(1-\nu)\dfrac{r_1 r_2}{R^2}\end{matrix} & \begin{matrix} -n_1\dfrac{4}{\mu}(1-\nu)\dfrac{r_1 r_2}{R^2} \\ +n_2\dfrac{2}{\mu}(1-\nu)\dfrac{r_1^2-r_2^2}{R^2}\end{matrix} \end{bmatrix}
$$

$$
\mathfrak{D}(R) = \frac{1}{8\pi(1-\nu)R^2} \qquad (2.3)
$$

is the fundamental solution of order two, n_ρ is the outer unit normal, $c_{\kappa\lambda}(y)$ depends on the angle formed by the tangents to the contour at y ($c_{\kappa\lambda}(y) = \delta_{\kappa\lambda}/2$ if the contour is smooth at y). $\mathfrak{U}_{\kappa\lambda}(x,y)$ and $\mathfrak{T}_{\kappa\lambda}(x,y)$ are weakly and strongly singular. Integral equation (2.1b) is that of the direct method for inner regions in the dual system of plane elasticity: the unknowns are $\mathfrak{u}_\lambda(x)$ on $\mathcal{L}_u$ and $\mathfrak{t}_\lambda(x)$ on $\mathcal{L}_t$ [5, 6]. The line integrals in (2.1b) should be taken in principal value.

Equation (2.1a) should be associated with appropriate boundary conditions. One can readily check that the stress function vector (the dual displacement vector) on the arcs of $\mathcal{L}_{ti}$ is of the form

$$
\hat{\mathfrak{u}}_\rho(s) = \int_{P_{ti}}^{s} \hat{t}_\rho(\sigma)\mathrm{d}\sigma \qquad s\in\mathcal{L}_{ti} \qquad i = 1,\ 3\ , \qquad (2.4)
$$

where – in accordance with all that has been said earlier – the hatted letters denote the prescribed values. Consequently, equation

$$
\mathfrak{u}_\rho(s) = \hat{\mathfrak{u}}_\rho(s) + C_\rho^{(ti)} \qquad s\in\mathcal{L}_{ti} \qquad i = 1,\ 3 \qquad (2.5)
$$

is the traction boundary condition. Observe that the quantities $C_\rho^{(ti)}$ in equation (2.5) are undetermined constants of integration.

The so-called strain boundary conditions on the arcs on $\mathcal{L}_{ui}$ have the following form:

$$
\frac{\mathrm{d}\hat{u}_\lambda}{\mathrm{d}s} = n_\rho[\epsilon_{\rho\pi 3}e_{\pi\lambda} - \delta_{\rho\lambda}\varphi_3] \qquad s\in\mathcal{L}_{ui} \qquad i = 2,\ 4\ , \qquad (2.6)
$$

where $\hat{u}_\lambda(s)$ is the vector of the prescribed displacements on $\mathcal{L}_{ui}$ and $e_{\kappa\lambda}$ are the in-plane components of the strain tensor.

If tractions (stress functions) are imposed on the whole contour $\mathcal{L}_o$ ($\mathcal{L}_t \equiv \mathcal{L}_o$), the compatibility condition in the large

$$
\int_{\mathcal{L}_o} n_\rho[\epsilon_{\rho\pi 3}e_{\pi\lambda} - \delta_{\rho\lambda}\varphi_3]\mathrm{d}s = 0 \qquad (2.7)
$$

should also be satisfied. If tractions (stress functions) are imposed only on the arcs $\mathcal{L}_{t1}$, $\mathcal{L}_{t3}$ of the contour $\mathcal{L}_o$, the supplementary conditions of single valuedness to be satisfied are

$$\int_{\mathcal{L}_{ti}} n_\rho[\epsilon_{\rho\pi 3} e_{\kappa\lambda} - \delta_{\rho\lambda}\varphi_3]\mathrm{d}s - \hat{u}_\lambda|_{P_{ti}}^{P_{t,i+1}} = 0 \qquad i = 1,\, 3\;, \tag{2.8}$$

where the extremities of the arc $\mathcal{L}_{ti}$ are denoted by P_{ti} and $P_{t,i+1}$, respectively.

If the compatibility field equation

$$\epsilon^{\kappa\rho 3} e_{\lambda\kappa;\rho} + \varphi^3_{.;\lambda} = \epsilon^{\kappa\rho 3}\left(e_{\lambda\kappa;\rho} - \epsilon_{\lambda\kappa 3}\varphi^3_{.;\rho}\right) = 0 \qquad\qquad x \in A_i \tag{2.9}$$

is fulfilled then the supplementary compatibility conditions (2.8) are not independent – one can be omitted [7]. Since no stresses belong to constant stress functions, we can also set two constants (one vector $C_\rho^{(ti)}$) to zero .

In this way, we have as many independent conditions of single valuedness (2.8) as there are undetermined integration constants $C_\rho^{(ti)}$ in the traction boundary condition (2.5).

The outer region A_e is understood as the part of the coordinate plane outside the closed curve $\mathcal{L}_o$ – see Figure 1. We shall assume that the stresses at infinity denoted by

$$t_{11}(\infty),\; t_{12}(\infty) = t_{21}(\infty),\; t_{22}(\infty)$$

are all constants. We shall also assume that the rigid body rotation vanishes at infinity:

$$\varphi_3(\infty) = 0\;. \tag{2.10}$$

The stresses at infinity can be obtained from the stress functions

$$\tilde{\mathfrak{u}}_\lambda(x) = \epsilon_{\alpha 3\rho} x_\alpha t_{\lambda\rho}(\infty) + c_\lambda(\infty)\;, \tag{2.11}$$

where there belong no stresses to the constant stress function vector $c_\lambda(\infty)$.

The three dual Somigliana formulae for the outer region are of the form

$$\mathfrak{u}_k(y) = \tilde{\mathfrak{u}}_\lambda(y) + \oint_{\mathcal{L}_o} \mathfrak{U}_{k\lambda}(x,y)\mathfrak{t}_\lambda(x)\,\mathrm{d}s_x - \oint_{\mathcal{L}_o} \mathfrak{T}_{k\lambda}(x,y)\mathfrak{u}_\lambda(x)\,\mathrm{d}s_x \quad y \in \mathcal{A}_e\;, \tag{2.12a}$$

$$c_{\kappa\lambda}(y)\mathfrak{u}_\lambda(y) = \tilde{\mathfrak{u}}_\lambda(y) + \oint_{\mathcal{L}_o} \mathfrak{U}_{\kappa\lambda}(x,y)\mathfrak{t}_\lambda(x)\,\mathrm{d}s_x - \oint_{\mathcal{L}_o} \mathfrak{T}_{\kappa\lambda}(x,y)\mathfrak{u}_\lambda(x)\,\mathrm{d}s_x \quad y \in \mathcal{L}_o\;, \tag{2.12b}$$

$$0 = \tilde{\mathfrak{u}}_\lambda(y) + \oint_{\mathcal{L}_o} \mathfrak{U}_{\kappa\lambda}(x,y)\mathfrak{t}_\lambda(x)\,\mathrm{d}s_x - \oint_{\mathcal{L}_o} \mathfrak{T}_{\kappa\lambda}(x,y)\mathfrak{u}_\lambda(x)\,\mathrm{d}s_x \quad y \notin \mathcal{A}_e \cup \mathcal{L}_o\;. \tag{2.12c}$$

3. Hypersingular integral equations in the dual system of plane elasticity

If we would like to use hypersingular equations in the dual system, the partial derivatives of equation (2.1c) with respect to the coordinates y_ρ of the source point y should be known. In order to obtain appropriate formulae, a small neighborhood of the source point y should be removed from the region of integration: this way we can avoid calculating singular integrals – the kernels are singular at the point $x = y$. Assume that the small circular domain $\mathcal{A}_\epsilon$ with the source point as its center is removed from the original region $\mathcal{A}_i$. Consequently, the new contour consists of two arcs (i) $\mathcal{L}_\varepsilon$ left from $\mathcal{L}_o$ after the removal of the small circle with radius ε and (ii) the circular arc s_ϵ.

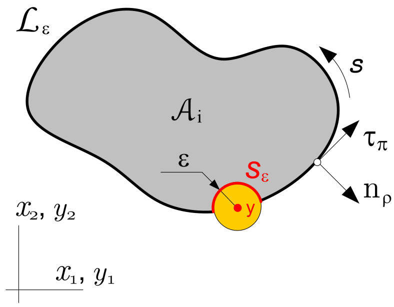

Figure 2. The boundary curve $\mathcal{L}_\varepsilon \cup s_\epsilon$

Under this condition equation (2.1c) can be written in the form

$$0 = \lim_{\varepsilon \to 0} \left\{ \int_{\mathcal{L}_\varepsilon} [\mathfrak{U}_{k\lambda}(x,y)\mathfrak{t}_\lambda(x) - \mathfrak{T}_{k\lambda}(x,y)\mathfrak{u}_\lambda(x)]\, \mathrm{d}s_x + \right. \\ \left. + \int_{s_\varepsilon} [\mathfrak{U}_{k\lambda}(x,y)\mathfrak{t}_\lambda(x) - \mathfrak{T}_{k\lambda}(x,y)\mathfrak{u}_\lambda(x)]\, \mathrm{d}s_x \right\} . \quad (3.1)$$

After deriving equation (3.1) with respect y_ρ, we have

$$\lim_{\varepsilon \to 0} \left\{ \int_{\mathcal{L}_\varepsilon} [\mathfrak{U}_{k\lambda,\rho}(x,y)\mathfrak{t}_\lambda(x) - \mathfrak{T}_{k\lambda,\rho}(x,y)\mathfrak{u}_\lambda(x)]\, \mathrm{d}s_x + \right. \\ \left. + \int_{s_\varepsilon} \mathfrak{U}_{k\lambda,\rho}(x,y)\mathfrak{t}_\lambda(x) - \mathfrak{T}_{k\lambda,\rho}(x,y)\mathfrak{u}_\lambda(x)\, \mathrm{d}s_x \right\} = 0\,, \quad (3.2)$$

where the derivatives $\mathfrak{U}_{k\lambda,\rho}$ are given below:

$$\mathfrak{U}_{k\lambda,1}(x,y)] = \mathfrak{K}_1 \begin{bmatrix} 2r_1 - \dfrac{4r_1r_2^2}{R^2} & -2r_2 + \dfrac{4r_1^2r_2}{R^2} \\ -2r_2 + \dfrac{4r_1^2r_2}{R^2} & 6r_1 - 4\dfrac{r_1^3}{R^2} \\ \dfrac{2}{\mu}(1-\nu)\dfrac{r_1^2 - r_2^2}{R^2} & \dfrac{2}{\mu}(1-\nu)\dfrac{2r_1r_2}{R^2} \end{bmatrix} , \quad (3.3)$$

$$[\mathfrak{U}_{k\lambda,2}(x,y)] = \mathfrak{K}_1 \begin{bmatrix} 6r_2 - \dfrac{4r_2^3}{R^2} & -2r_1 + \dfrac{4r_1r_2^2}{R^2} \\ -2r_1 + \dfrac{4r_1r_2^2}{R^2} & 2r_2 - 4\dfrac{r_1^2r_2}{R^2} \\ \dfrac{2}{\mu}(1-\nu)\dfrac{2r_1r_2}{R^2} & \dfrac{2}{\mu}(1-\nu)\dfrac{r_2^2-r_1^2}{R^2} \end{bmatrix} . \tag{3.4}$$

We have also determined the derivatives $\mathfrak{T}_{\kappa\lambda,\rho}$. The results are presented in Appendix A – see equations (A.1). Due to the derivation, the order of singularity of the kernels is increased, i.e., $\mathcal{D}_{k\rho\lambda} = \mathfrak{U}_{k\lambda,\rho}$ has a singularity of order one, while the singularity of $\mathcal{S}_{k\rho\lambda} = \mathfrak{T}_{k\lambda,\rho}$ is that of order two.

Assume further that the stress functions of order one are continuous and differentiable in the neighborhood of the point y. Then it holds with a good accuracy that

$$\mathfrak{u}_\lambda(x) = \mathfrak{u}_\lambda(y) + \mathfrak{u}_{\lambda,\delta}(y)(x_\delta - y_\delta) + O(r^{1+\alpha}) , \tag{3.5}$$

where O is the ordo symbol. It is also not too difficult to check that the displacement derivative $\mathfrak{t}_\lambda$ in the vicinity of the source point assumes the form

$$\mathfrak{t}_\lambda(x) = -\frac{\partial u_\lambda}{\partial s} \cong -u_{\lambda,\pi}(y)\tau_\pi(x) = -u_{\lambda,\pi}(y)\epsilon_{3\rho\pi}n_\rho(x) , \tag{3.6}$$

where the outward unit normal n_ρ is taken at the point x and τ_π is the unit tangent.

Making use of these approximations, we can rewrite equation (3.2) in the form

$$\begin{aligned} \lim_{\varepsilon\to 0}\Bigg\{ \int_{\mathcal{L}_\varepsilon} [\mathcal{D}_{k\rho\lambda}\mathfrak{t}_\lambda(x) - \mathcal{S}_{k\rho\lambda}\mathfrak{u}_\lambda(x)]\, \mathrm{d}s_x + \int_{s_\varepsilon} \mathcal{D}_{k\rho\lambda}[\mathfrak{t}_\lambda(x) + u_{\lambda,\pi}(y)\tau_\pi(x)]\, \mathrm{d}s_x - \\ - \int_{s_\varepsilon} \mathcal{S}_{k\rho\lambda}[\mathfrak{u}_\lambda(x) - \mathfrak{u}_{\lambda,\delta}(y)(x_\delta - y_\delta) - \mathfrak{u}_\lambda(y)]\, \mathrm{d}s_x - \int_{s_\varepsilon} \mathcal{S}_{k\rho\lambda}\mathrm{d}s_x\mathfrak{u}_\lambda(y) - \\ - \int_{s_\varepsilon} \mathcal{D}_{k\rho\lambda}u_{\lambda,\pi}(y)\tau_\pi(x)\mathrm{d}s_x - \int_{s_\varepsilon} \mathcal{S}_{k\rho\lambda}\mathfrak{u}_{\lambda,\delta}(y)(x_\delta - y_\delta)\mathrm{d}s_x \Bigg\} = 0 . \end{aligned} \tag{3.7}$$

Observe that the second integral in the first line and the first integral in the second line are equal to zero if we take their limits. The value of the last integral in the second line can be manipulated into the form

$$\lim_{\varepsilon\to 0}\left\{ \int_{s_\varepsilon} \mathcal{S}_{k\rho\lambda}\mathrm{d}s_x\mathfrak{u}_\lambda(y) \right\} = \lim_{\varepsilon\to 0}\left\{ \frac{b_{k\rho\lambda}(y)}{\varepsilon}\mathfrak{u}_\lambda(y) \right\} . \tag{3.8}$$

This formula clearly shows that the limit of the above integral – due to the fact that the kernel is singular – is unbounded and depends also on the value of $b_{\kappa\rho\lambda}(y)$. However, if the source point y is an internal point, then $b_{\kappa\rho\lambda}(y) = 0$ – the proof is omitted here. Therefore, if we take the limit of the last two integrals in (3.7), we have

$$\lim_{\varepsilon\to 0}\left\{ \int_{s_\varepsilon} \mathcal{D}_{k\rho\lambda}u_{\lambda,\pi}(y)\tau_\pi(x)\mathrm{d}s_x + \int_{s_\varepsilon} \mathcal{S}_{k\rho\lambda}\mathfrak{u}_{\lambda,\delta}(y)(x_\delta - y_\delta)\mathrm{d}s_x \right\} = d_{k\rho\alpha\beta}(y)\mathfrak{u}_{\alpha,\beta}(y) , \tag{3.9}$$

where $d_{\kappa\rho\alpha\beta}(y)\mathfrak{u}_{\alpha,\beta} = 0.5\mathfrak{u}_{\kappa,\rho}$ if the contour $\mathcal{L}_o$ is smooth at the source point y. Finally, we obtain

$$\lim_{\varepsilon\to 0}\left\{\int_{\mathcal{L}_\varepsilon}\left[\mathcal{D}_{k\rho\lambda}\mathfrak{t}_\lambda(x)\ -\mathcal{S}_{k\rho\lambda}\mathfrak{u}_\lambda(x)\right]\,\mathrm{d}s_x\right\} = \lim_{\varepsilon\to 0}\left\{\frac{b_{k\rho\lambda}}{\varepsilon}\mathfrak{u}_\lambda(y)\right\} + d_{k\rho\alpha\beta}(y)\mathfrak{u}_{\alpha,\beta}(y)\ . \tag{3.10}$$

or by rearranging it we get

$$\frac{1}{2}\mathfrak{u}_{k,\rho}(y) + \lim_{\varepsilon\to 0}\left\{\int_{\mathcal{L}_o}\left[\mathcal{S}_{k\rho\lambda}\mathfrak{u}_\lambda(x) - \mathcal{D}_{k\rho\lambda}\mathfrak{t}_\lambda(x)\,\right]\,\mathrm{d}s_x + \frac{b_{k\rho\lambda}}{\varepsilon}\mathfrak{u}_\lambda(y)\right\} = 0\ . \tag{3.11}$$

Let us introduce the following notations:

$$\fint_{\mathcal{L}_o}\mathcal{D}_{k\rho\lambda}\mathfrak{t}_\lambda(x)\mathrm{d}s_x = \lim_{\varepsilon\to 0}\int_{\mathcal{L}_o}\mathcal{D}_{k\rho\lambda}\mathfrak{t}_\lambda(x)\mathrm{d}s_x \tag{3.12}$$

and

$$\bbint_{\mathcal{L}_o}\mathcal{S}_{k\rho\lambda}\mathfrak{u}_\lambda(x)\mathrm{d}s_x = \lim_{\varepsilon\to 0}\left\{\int_{\mathcal{L}_o}\mathcal{S}_{k\rho\lambda}\mathfrak{u}_\lambda(x)\mathrm{d}s_x + \frac{b_{k\rho\lambda}}{\varepsilon}\mathfrak{u}_\lambda(y)\right\}\ . \tag{3.13}$$

Making use of the notations introduced, equation (3.11) can be rewritten in the same form as in the primal system of elasticity:

$$\frac{1}{2}\mathfrak{u}_{k,\rho}(y) = \fint_{\mathcal{L}_o}\mathcal{D}_{k\rho\lambda}\mathfrak{t}_\lambda(x)\mathrm{d}s_x - \bbint_{\mathcal{L}_o}\mathcal{S}_{k\rho\lambda}\mathfrak{u}_\lambda(x)\mathrm{d}s_x\ . \tag{3.14}$$

Assume further that the contour $\mathcal{L}_o$ is divided into n_{be} boundary elements, which have three nodes and are denoted by $\mathcal{L}_e$. With the previous notations, the corresponding formula for computing the elements of the stress tensor at the boundary point y is rewritten into this form:

$$\begin{aligned} t_{\psi\kappa}(y) = \epsilon_{\psi\rho 3}\mathfrak{u}_{\kappa,\rho}(y) = 2\epsilon_{\psi\rho 3}&\left\{\sum_{e=1}^{n_{be}}\int_{\mathcal{L}_e}\mathcal{D}_{\kappa\rho\lambda}\left(x,y\right)\mathfrak{t}^e_\lambda\mathrm{d}s_x - \right.\\ &\left. - \sum_{e=1,e\neq m}^{n_{be}}\int_{\mathcal{L}_e}\mathcal{S}_{\kappa\rho\lambda}\left(x,y\right)\mathfrak{u}^e_\lambda\mathrm{d}s_x - I^m_{\kappa\rho\lambda}\mathfrak{u}^m_\lambda\right\}\ . \end{aligned} \tag{3.15}$$

Here the upper index e is the number of the boundary element considered. The element that contains the source point y is denoted by the upper index m. $I^m_{\kappa\rho j}$ stands for the line integral with the hypersingular kernel.

4. Numerical evaluation of the hypersingular integral

Assume that the nodal values of the variables are known from the solution of the direct boundary integral equation method. The nodal values $\mathfrak{u}^a_\lambda$ and $\mathfrak{t}^a_\lambda$ $(a = 1,\dots,3)$, which belong to element e and local node number a are given in the matrix form

$$[\mathfrak{u}^e_j]^T = \left[\ [\mathfrak{u}^1_\lambda]^T\quad [\mathfrak{u}^2_\lambda]^T\quad [\mathfrak{u}^3_\lambda]^T\ \right] = \left[\ \mathfrak{u}^1_1\quad \mathfrak{u}^1_2\quad \mathfrak{u}^2_1\quad \mathfrak{u}^2_2\quad \mathfrak{u}^3_1\quad \mathfrak{u}^3_2\ \right] \tag{4.1}$$

and

$$[\mathfrak{t}^e_j]^T = \left[\ \mathfrak{t}^1_1\quad \mathfrak{t}^1_2\quad \mathfrak{t}^2_1\quad \mathfrak{t}^2_2\quad \mathfrak{t}^3_1\quad \mathfrak{t}^3_2\ \right] \tag{4.2}$$

on the e-th element ($j = 1, \dots, 6$). It is obvious that the approximations of the vectors $\mathfrak{u}_\lambda$ and $\mathfrak{t}_\lambda$ on the e-th element take the form:

$$\mathfrak{u}_\lambda = N_{\lambda j}(\xi)\mathfrak{u}_j^e \,, \qquad \mathfrak{t}_\lambda = N_{\lambda j}(\xi)\mathfrak{t}_j^e \,, \tag{4.3}$$

in which e identifies the element and

$$[N_{\lambda j}(\xi)] = \begin{bmatrix} N^1(\xi) & 0 & N^2(\xi) & 0 & N^3(\xi) & 0 \\ 0 & N^1(\xi) & 0 & N^2(\xi) & 0 & N^3(\xi) \end{bmatrix} \tag{4.4}$$

is the shape function matrix constituted by the quadratic Lagrange polynomials

$$N^1(\xi) = \frac{1}{2}\xi(\xi-1), \qquad N^2(\xi) = 1-\xi^2, \qquad N^3(\xi) = \frac{1}{2}\xi(\xi+1) \tag{4.5}$$

that map the element onto the interval $\xi \in [-1, 1]$ – isoparametric approximation. Making use of approximations (4.3) in (3.15), the stress tensor $t_{\psi\kappa}$ at the boundary point is calculated as follows:

$$t_{\psi\kappa}(\eta) = 2\epsilon_{\psi\rho 3}\left\{\sum_{e=1}^{n_{be}} \int_{\mathcal{R}^e} \mathcal{D}_{\kappa\rho\lambda}(\xi,\eta)\, N_{\lambda j}(\xi) J(\xi)\mathrm{d}\xi \mathfrak{t}_j^e - \right.$$
$$\left. - \sum_{e=1, e\neq m}^{n_{be}} \int_{\mathcal{R}^e} \mathcal{S}_{\kappa\rho\lambda}(\xi,\eta)\, N_{\lambda j}(\xi) J(\xi)\mathrm{d}\xi \mathfrak{u}_j^e - I^m_{\kappa\rho j}\mathfrak{u}_j^m \right\} . \tag{4.6}$$

Here $J(\xi)$ is the Jacobian, $\mathcal{R}^e$ is the map of $\mathcal{L}_e$ on the interval $[-1, 1]$. The meaning of $\mathcal{R}^m_\varepsilon$ can be read off from Figure 3 which also shows the map of $\mathcal{L}_e$ on the axis ξ.

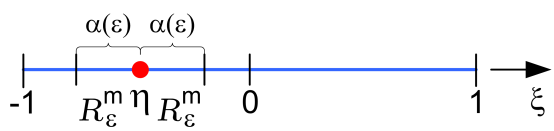

Figure 3. The interval $\mathcal{R}^m_\varepsilon$

The length of $\mathcal{R}^m_\varepsilon$ is denoted by $\alpha(\varepsilon)$, while η is the image of the source point y on this interval. The line integral containing the hypersingularity can be given in the following form:

$$I^m_{\kappa\rho j} = \int_{\mathcal{R}^m} \mathcal{S}_{k\rho\lambda}(\xi,\eta)\, N_{\lambda j}(\xi) J(\xi)\mathrm{d}\xi = \int_{\mathcal{R}^m} F^m_{\kappa\rho j}(\xi,\eta)\mathrm{d}\xi \,. \tag{4.7}$$

To determine the power series of $\mathcal{S}_{\kappa\rho\lambda}(\xi,\eta)$ in ξ, we have to utilize the equations

$$\frac{r_\lambda}{R} = \frac{A_\lambda}{A} sgn(\delta) + \left[\frac{B_\lambda}{A} - \frac{A_\lambda C}{A^3}\right]\frac{\delta}{sgn(\delta)} + O(\delta^2) \tag{4.8}$$

and

$$\frac{1}{R^2} = \frac{1}{A^2\delta^2} - 2\frac{C}{A^4\delta} + O(1) \,, \tag{4.9}$$

in which $\delta = \xi - \eta$. The constants A_λ and B_λ are derived from the first two terms of the Taylor series of the position vector r_λ in the vicinity of the source point:

$$r_\lambda = x_\lambda(\xi) - y_\lambda(\eta) = 0 + \underbrace{\left.\frac{\partial x_\lambda}{\partial \xi}\right|_{\xi=\eta}}_{A_\lambda} \underbrace{(\xi-\eta)}_{\delta} + \underbrace{\frac{1}{2!}\left.\frac{\partial^2 x_\lambda}{\partial \xi^2}\right|_{\xi=\eta}}_{B_\lambda} (\xi-\eta)^2 + \ldots =$$

$$= A_\lambda \delta + B_\lambda \delta^2 + O(\delta^3) \ , \quad (4.10)$$

where

$$A_\lambda = (x^1_\lambda - 2x^2_\lambda + x^3_\lambda)\eta + \frac{1}{2}(x^3_\lambda - x^1_\lambda) \ , \quad B_\lambda = \frac{1}{2}(x^1_\lambda - 2x^2_\lambda + x^3_\lambda) \quad (4.11)$$

are constants at η. $A = \sqrt{\sum A^2_\lambda}$ and $C = \sum A_\lambda B_\lambda$. The power series of the shape function matrix is then

$$N_{\lambda j}(\xi) = \left. N_{\lambda j}(\xi)\right|_{\xi=\eta} + \left.\frac{\mathrm{d}}{\mathrm{d}\xi} N_{\lambda j}(\xi)\right|_{\xi=\eta} (\xi-\eta) + O(\delta^2) =$$

$$= {}^0N_{\lambda j}(\eta) + {}^1N_{\lambda j}(\eta)\delta + O(\delta^2) \ , \quad (4.12)$$

in which the elements are given by

$${}^0N^1(\eta) = \frac{1}{2}\eta(\eta-1), \qquad {}^0N^2(\eta) = 1-\eta^2, \qquad {}^0N^3(\eta) = \frac{1}{2}\eta(\eta+1) \quad (4.13)$$

$${}^1N^1(\eta) = \frac{1}{2}(\eta-1), \qquad {}^1N^2(\eta) = -2\eta, \qquad {}^1N^3(\eta) = \frac{1}{2}(\eta+1) \ . \quad (4.14)$$

The product of the Jacobian and the vector n_ρ can also be given in the following forms:

$$J_1(\xi) = n_1 J(\xi) = A_2 + 2B_2\delta + O(\delta^2) \ , \quad (4.15)$$

$$J_2(\xi) = n_2 J(\xi) = -A_1 - 2B_1\delta + O(\delta^2) \ . \quad (4.16)$$

After substituting power series (4.8)-(4.16) into integral (4.7), the integrand $F^m_{\kappa\rho j}(\xi,\eta)$ can be manipulated in a Laurent series in the vicinity of the source point η:

$$F^m_{\kappa\rho j}(\xi,\eta) = \frac{{}^{-2}F^m_{\kappa\rho j}(\eta)}{(\xi-\eta)^2} + \frac{{}^{-1}F^m_{\kappa\rho j}(\eta)}{\xi-\eta} + O(1) \ , \quad (4.17)$$

where ${}^{-1}F^m_{\kappa\rho j}(\eta)$ and ${}^{-2}F^m_{\kappa\rho j}(\eta)$ are constant values at a fixed $\eta \in (-1,1)$. Subtracting the first two terms of the power series from $F^m_{\kappa\rho j}(\xi,\eta)$ in equation (4.7) and investigating the terms obtained separately, three line integrals are resulted:

$$I^m_{\kappa\rho j} = \lim_{\varepsilon\to 0}\int_{\mathcal{R}^m - 2\mathcal{R}^m_\varepsilon} \left\{ F^m_{\kappa\rho j}(\xi,\eta) - \left[\frac{{}^{-2}F^m_{\kappa\rho j}(\eta)}{(\xi-\eta)^2} + \frac{{}^{-1}F^m_{\kappa\rho j}(\eta)}{\xi-\eta}\right]\right\}\mathrm{d}\xi +$$

$$+ \lim_{\varepsilon\to 0}\int_{\mathcal{R}^m - 2\mathcal{R}^m_\varepsilon} \frac{{}^{-2}F^m_{\kappa\rho j}(\eta)}{(\xi-\eta)^2}\mathrm{d}\xi + \lim_{\varepsilon\to 0}\int_{\mathcal{R}^m - 2\mathcal{R}^m_\varepsilon} \frac{{}^{-1}F^m_{\kappa\rho j}(\eta)}{\xi-\eta}\mathrm{d}\xi = {}^0I^m_{\kappa\rho j} + {}^{-2}I^m_{\kappa\rho j} + {}^{-1}I^m_{\kappa\rho j} \ . \quad (4.18)$$

Observe that the integrand of ${}^0I^m_{\kappa\rho j}$ is a polynomial function without singular terms. Its limit therefore assumes the following form:

$${}^0I^m_{\kappa\rho j} = \int_{-1}^{1} \left\{ F_{\kappa\rho\lambda}(\xi,\eta) - \left[\frac{{}^{-2}F^m_{\kappa\rho j}(\eta)}{(\xi-\eta)^2} + \frac{{}^{-1}F^m_{\kappa\rho j}(\eta)}{\xi-\eta}\right]\right\}\mathrm{d}\xi \ . \quad (4.19)$$

This integral is regular and can be calculated numerically by using the standard integration techniques. We have chosen a 14 node Gaussian quadrature rule for the interval $[-1,1]$. The second and third terms on the right side of (4.18) can be determined analytically. To this end we have to use the following expansion of α – see Figure 3 – in the powers of ε:

$$\alpha(\varepsilon)=\frac{\varepsilon}{A}-\frac{C}{A^4}\varepsilon^2 sgn(\alpha)+O(\varepsilon^3)\,. \tag{4.20}$$

After dividing $\mathcal{R}^m$ into two subintervals $[-1,-\alpha]$ and $[\alpha,1]$ at the singular point η and making use of series (4.20) we can determine the limit of the last two integrals in equation (4.18). After some hand calculations, we obtain the following analytical result

$$\begin{aligned}{}^{-1}I^m_{\kappa\rho j}&=\lim_{\varepsilon\to 0^-}\left\{\int_{-1}^{\eta-\alpha}\frac{{}^{-1}F^m_{\kappa\rho j}(\eta)}{\xi-\eta}\mathrm{d}\xi\right\}+\lim_{\varepsilon\to 0^+}\left\{\int_{\eta+\alpha}^{1}\frac{{}^{-1}F^m_{\kappa\rho j}(\eta)}{\xi-\eta}\mathrm{d}\xi\right\}=\\&={}^{-1}F^m_{\kappa\rho j}(\eta)\ln\left|\frac{1-\eta}{-1-\eta}\right|\,.\end{aligned} \tag{4.21}$$

Likewise, the last integral in equation (4.18) can also be given in a closed form:

$$\begin{aligned}{}^{-2}I^m_{\kappa\rho j}&=\lim_{\varepsilon\to 0^-}\left\{\int_{-1}^{\eta-\alpha}\frac{{}^{-2}F^m_{\kappa\rho j}(\eta)}{(\xi-\eta)^2}\mathrm{d}\xi\right\}+\lim_{\varepsilon\to 0^+}\left\{\int_{\eta+\alpha}^{1}\frac{{}^{-2}F^m_{\kappa\rho j}(\eta)}{(\xi-\eta)^2}\mathrm{d}\xi\right\}=\\&={}^{-2}F^m_{\kappa\rho j}(\eta)\left(\frac{1}{-1-\eta}-\frac{1}{1-\eta}\right)\,.\end{aligned} \tag{4.22}$$

Consequently, formulae (4.19), (4.21) and (4.22) can be used to determine the value of the hypersingular integrals over the element containing the hypersingularity.

It is obvious that these integrals can easily be calculated and thus they can given in closed form. After collecting partial results, the final formula for the evaluation of the hypersingular integral is given by

$$\begin{aligned}I^m_{\kappa\rho j}=&\int_{-1}^{1}F^m_{\kappa\rho j}(\xi,\eta)-\left[\frac{{}^{-2}F^m_{\kappa\rho j}(\eta)}{(\xi-\eta)^2}+\frac{{}^{-1}F^m_{\kappa\rho j}(\eta)}{\xi-\eta}\right]\mathrm{d}\xi+\\&+{}^{-2}F^m_{\kappa\rho j}(\eta)\left(-\frac{1}{1-\eta}+\frac{1}{-1-\eta}\right)+{}^{-1}F^m_{\kappa\rho j}\ln\left|\frac{1-\eta}{-1-\eta}\right|\,,\end{aligned} \tag{4.23}$$

where $\eta\in(-1,1)$. In those cases where $\eta=-1$ or $\eta=1$ the previous derivation leads to the following formula:

$$\begin{aligned}I_{\kappa\rho j}=&\sum_{m=1}^{2}\left\{\int_{-1}^{1}F^m_{\kappa\rho\lambda}(\xi,\eta)-\left[\frac{{}^{-2}F^m_{\kappa\rho j}(\eta)}{(\xi-\eta)^2}+\frac{{}^{-1}F^m_{\kappa\rho j}(\eta)}{\xi-\eta}\right]\mathrm{d}\xi-\right.\\&\left.-{}^{-2}F^m_{\kappa\rho j}(\eta)\left(\frac{\gamma_m}{\beta_m^2}sgn(\delta)+\frac{1}{2}\right)+{}^{-1}F^m_{\kappa\rho j}\ln\left|\frac{2}{\beta_m}\right|sgn(\delta)\right\}\,.\end{aligned} \tag{4.24}$$

The calculation program, written in Fortran90, has been developed for the numerical solution using the formulae of [6] and equations (4.23), (4.24).

5. Numerical examples

Problem 1. We shall consider a circular region with radius $R = 10\,\mathrm{mm}$. The material properties are $\mu = 8 \cdot 10^4\,\mathrm{MPa}$, $\nu = 0.3$.

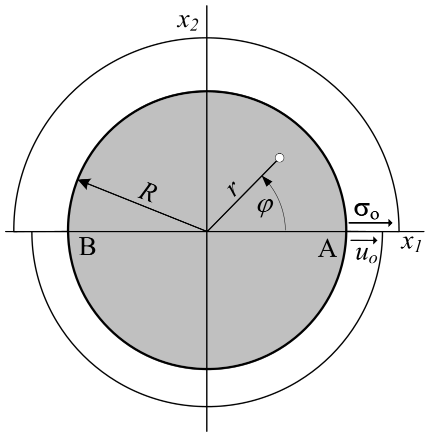

Figure 4. A circular region

On the arc AB of the contour for which the angle $\varphi \in [0, \pi]$ the normal stress is $\sigma_o = 100\,\mathrm{MPa}$ and there is no shear stress. On the arc BA of the contour $u_o = (1 - 2\nu)\sigma_o r_o / 2\mu$ is the radial displacement and there is no displacement in the circumferential direction – see Figure 4. One can check with ease that these solutions determine a homogenous state of stress. At the points of the region $\mathcal{A}_i$ the exact solutions for the stresses are as follows:

$$\sigma_1 = \sigma_2 = \sigma_o = 100\ [\mathrm{MPa}], \qquad \tau_{12} = \tau_{21} = 0\ .$$

Table 1 below shows how the accuracy of numerical results at a boundary point is increased if we increase the number of boundary elements n_{be}.

Table 1: Solutions for stress components

n_{be}	σ_1 [MPa]	$\tau_{12} = \tau_{21}$ [MPa]	σ_2 [MPa]
8	99.86512	$-6.04096 \cdot 10^{-3}$	99.88720
16	99.98509	$-6.17259 \cdot 10^{-4}$	99.98576
32	99.99821	$-4.42785 \cdot 10^{-5}$	99.99823
64	99.99978	$-2.74219 \cdot 10^{-6}$	99.99957

Problem 2. Though the contour $\mathcal{L}_o$ and the material are the same as in the previous examples the region under consideration is the outer one, for which a constant stress state $\sigma_1(\infty) = 100$ MPa, $\tau_{12}(\infty) = \tau_{21}(\infty) = \sigma_2(\infty) = 0$ is prescribed at infinity. The inner boundary is free of displacement constraints.

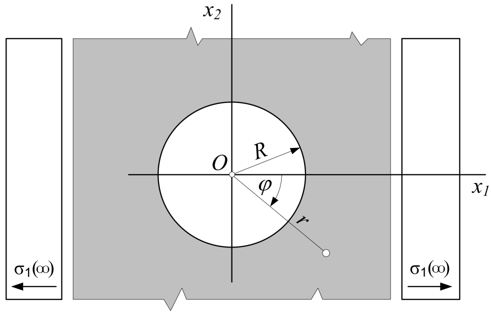

Figure 5. Outer region bounded by a circle

It is well known that the formulae

$$\sigma_r = \frac{\sigma_1(\infty)}{2}\left[\left(1-\frac{r_o^2}{r^2}\right)+\left(1+\frac{3r_o^4}{r^4}-\frac{4r_o^2}{r^2}\right)\cos 2\varphi\right], \tag{5.1a}$$

$$\sigma_\varphi = \frac{\sigma_1(\infty)}{2}\left[\left(1+\frac{r_o^2}{r^2}\right)-\left(1+\frac{3r_o^4}{r^4}\right)\cos 2\varphi\right], \tag{5.1b}$$

$$\tau_{r\varphi} = \frac{\sigma_1(\infty)}{2}\left[\left(1-\frac{3r_o^4}{r^4}+\frac{2r_o^2}{r^2}\right)\sin 2\varphi\right]. \tag{5.1c}$$

written in polar coordinates give the exact solution to this problem – see [8] or [9]. The exact solution on the whole boundary curve is computed from (5.1) in the coordinate system (x_1, x_2):

$$\sigma_1 = \sigma_1(\infty)\,[1-2\cos 2\varphi]\sin^2\varphi\,, \tag{5.2a}$$

$$\sigma_2 = \sigma_1(\infty)\,[1-2\cos 2\varphi]\cos^2\varphi\,, \tag{5.2b}$$

$$\tau_{12} = \tau_{21} = \sigma_1(\infty)\,[1-2\cos 2\varphi]\sin\varphi\cos\varphi \tag{5.2c}$$

The contour was divided into 16 equidistant elements. The diagrams below show the stresses as function φ along the circle in clockwise direction.

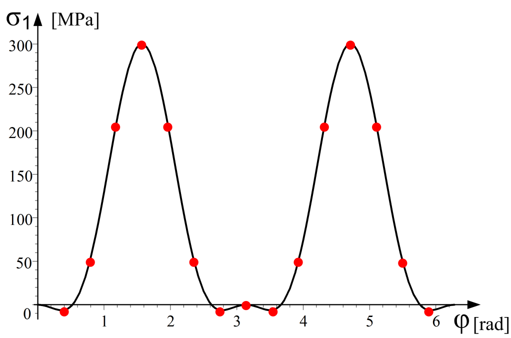

Figure 6. Exact and numerical solution – σ_1 as function φ

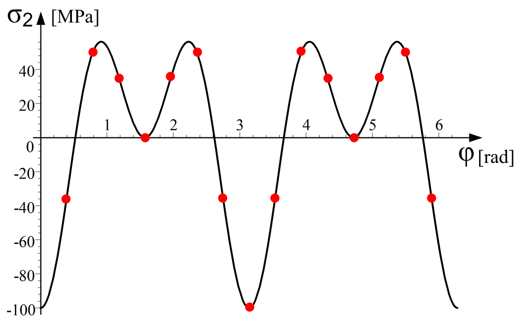

Figure 7. Exact and numerical solution – σ_2 as function φ

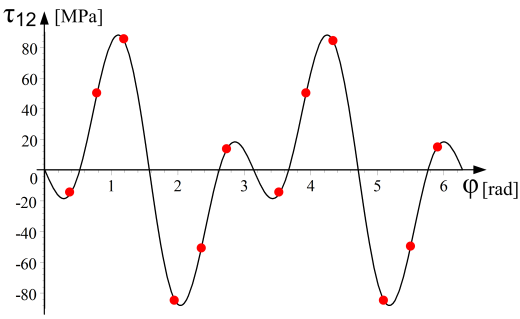

Figure 8. Exact and numerical solution – τ_{12} as function φ

Table 2 below represents the numerical results obtained at various boundary points.

Table 2: Solutions for stress components

φ	$\sigma_1[MPa]$		$\tau_{12} = \tau_{21}[MPa]$		$\sigma_2[MPa]$	
$\pi/8$	-6.085	-6.066	-14.679	-14.645	-35.346	-35.355
$\pi/4$	50.026	50.00	50.047	50.00	50.072	50.00
$3\pi/8$	206.169	206.07	85.457	85.355	35.353	35.355
$\pi/2$	300.196	300.00	0.00	0.00	-0.072	0.00

The numerical results show a good agreement with the analytical results that appear in the second columns.

6. Concluding remarks

This paper is concerned with a hypersingular boundary integral formulation in the dual system of plane elasticity. Our main objective was to present a method by which the stress components on the boundary can be computed with high accuracy both in the plane region and on its boundary. We have developed the hypersingular boundary integral equation (HBIE) method in the dual system of plane elasticity providing that (i) the region under consideration is a simply-connected one, (ii) there are no body forces, (iii) the contour consists of two arcs on which tractions and displacements are prescribed, respectively. The line of thought is based on a technique developed by Guiggiani et al. [1] for the primal system of plane elasticity.

It has been proven that the formulae for calculating the stresses on the boundary can be given in closed forms. The hypersingular integrals in these formulae can be resolved into two parts. The first one should be computed numerically – this computation results in, however, a very small numerical error. The second part can be given in a closed form. Consequently, in contrast to the conventional stress calculation, which uses polynomial approximations for the derivatives and thus might lead to significant errors both in the formalism and in the numerical results in the vicinity of the boundary, the stress calculation method suggested in this paper in the dual system is much more reliable and accurate due to the way we handle the hypersingular integrals.

A program has been developed in Fortran 90 for the numerical computations. The results shown demonstrate that the accuracy of the computations is increased in the dual formulations if we use hypersingular integral equations.

Acknowledgements. The described work was carried out as part of the TÁMOP-4.2.1.B-10/2/KONV-2010-0001 project in the framework of the New Hungarian Development Plan. The realization of this project is supported by the European Union, co-financed by the European Social Fund.

References

1. Guiggiani, M., Krishnasamy, G., Rizzo, F. J., and Randolphi, T. J.: Hypersingular boundary integral equations: a new approach to their numerical treatment. IABEM Symposium, 1990.
2. Guiggiani, M.: Direct evluation of hypersingular integrals in 2D BEM, (7th GAMM Seminar on Numerical techniques for Boundary Element Method, Kiel, Germany, 1991). In W. Hackbusch (ed.), *Notes in Numerical Fluid Mechanics*, 1992, pp. 23–34.
3. Hildenbrand, J. and Kuhn, G.: Numerical computation of hypersingular integrals and application to the boundary integral equation for the stress tensor. *Engineering Analysis with Boundary Elements*, **10**, (1992), 209–217.
4. Guiggiani, M.: Hypersingular formulation for boundary stress evaluation. *Engineering Analysis with Boundary Elements*, **13**(2), (1994), 169–179.
5. Szeidl, G.: *Dual problems of continuum mechanics (derivation of defining equations, single valuedness of mixed boundary value problems, boundary element method for plane problems).* Habilitation Booklets of the Miskolc University (in Hungarian), Faculty of Mechanical Engineering, University of Miskolc, Department of Mechanics, 1997.
6. Szeidl, G.: Boundary integral equations for plane problems in terms of stress functions of order one. *Journal of Computational and Applied Mechanics*, **2**(2), (2001), 237–261.
7. Szeidl, G.: *Problems of Continuum Mechanics in a Dual Formulation (Derivation of the definig equations, Single valuedness of mixed boundary value problems, Boundary element*

method for plane problems). Thesis for the degree of Doctor of Science awarded by the Hungarian Academy of Sciences (in Hungarian), 2004.

8. Timoshenko, S. and Goodier, J. N.: *Theory of Elasticity.* McGraw-Hill, 1951.
9. Muskhelisvili, I. I.: *Some Fundamental Problems of Mathematical Theory of Elasticity.* Publisher NAUKA, 1966.

Appendix A.

A.1. **Derivatives of the fundamental solution of order two.** Making use of equation (2.3), we can determine the derivatives $\mathcal{S}_{k\rho\lambda} = \mathfrak{T}_{\kappa\lambda,\rho}$. The results are presented below:

$$\mathcal{S}_{111} = \mathfrak{D}(R)\left\{\frac{1}{R^2}\left[n_1 r_2\left(16\frac{r_1^2 r_2}{R^2} + 4(1-2\nu)r_2\right) + n_2 r_1\left(16\frac{r_2^3}{R^2} - 4(3-2\nu)r_2\right)\right] - \right.$$
$$\left. - \left[n_1\left(4\frac{r_1^2}{R^2} + 2(1-2\nu)\right)\right]\right\} \tag{A.1a}$$

$$\mathcal{S}_{112} = \mathfrak{D}(R)\left\{-\frac{1}{R^2}n_1 r_2\left(16\frac{r_1^3}{R^2} - 4(3-2\nu)r_1\right) - \frac{1}{R^2}n_2 r_1\left(16\frac{r_1 r_2^2}{R^2} + 4(1-2\nu)r_1\right) + \right.$$
$$\left. + n_2\left(4\frac{r_2^2}{R^2} + 2(1-2\nu)\right)\right\} \tag{A.1b}$$

$$\mathcal{S}_{211} = \mathfrak{D}(R)\left\{-\frac{1}{R^2}n_1 r_2\left(16\frac{r_1^3}{R^2} - 4(1+2\nu)r_1\right) - \frac{1}{R^2}n_2 r_1\left(16\frac{r_1^3}{R^2} - 4(1-2\nu)r_1\right) + \right.$$
$$\left. + n_2\left(4\frac{r_2^2}{R^2} - 2(1-2\nu)\right)\right\} \tag{A.1c}$$

$$\mathcal{S}_{212} = \mathfrak{D}(R)\left\{\frac{1}{R^2}n_2 r_2\left(16\frac{r_1^3}{R^2} - 4(5-2\nu)r_1\right) + \frac{1}{R^2}n_1 r_1\left(16\frac{r_1^3}{R^2} - 4(5-2\nu)r_1\right) - \right.$$
$$\left. - n_1\left(4\frac{r_1^2}{R^2} - 2(3-2\nu)\right)\right\} \tag{A.1d}$$

$$\mathcal{S}_{121} = \mathfrak{D}(R)\left\{\frac{1}{R^2}n_1 r_1\left(16\frac{r_2^3}{R^2} - 4(5-2\nu)r_2\right) + \frac{1}{R^2}n_2 r_2\left(16\frac{r_2^3}{R^2} - 4(5-2\nu)r_2\right) - \right.$$
$$\left. - n_2\left(4\frac{r_2^2}{R^2} - 2(3-2\nu)\right)\right\} \tag{A.1e}$$

$$\mathcal{S}_{122} = \mathfrak{D}(R)\left\{-\frac{1}{R^2}n_2 r_1\left(16\frac{r_2^3}{R^2} - 4(1+2\nu)r_2\right) - \frac{1}{R^2}n_1 r_2\left(16\frac{r_1^2 r_2}{R^2} - 4(1-2\nu)r_2\right) + \right.$$
$$\left. + n_1\left(4\frac{r_1^2}{R^2} - 2(1-2\nu)\right)\right\} \tag{A.1f}$$

$$\mathcal{S}_{221} = \mathfrak{D}(R)\left\{\frac{1}{R^2}\left[-n_1 r_2\left(16\frac{r_1^2 r_2}{R^2} + 4(1-2\nu)r_2\right) - n_2 r_1\left(16\frac{r_2^3}{R^2} - 4(3-2\nu)r_2\right)\right] + \right.$$
$$\left. + n_1\left(4\frac{r_1^2}{R^2} + 2(1-2\nu)\right)\right\} \tag{A.1g}$$

$$\mathcal{S}_{222} = \mathfrak{D}(R)\left\{\frac{1}{R^2}\left[n_1 r_2\left(16\frac{r_1^3}{R^2} - 4(3-2\nu)r_1\right) + n_2 r_1\left(16\frac{r_1 r_2^2}{R^2} + 4(1-2\nu)r_1\right)\right] - \right.$$
$$\left. -n_2\left(4\frac{r_2^2}{R^2} + 2(1-2\nu)\right)\right\} \quad \text{(A.1h)}$$

where $\mathfrak{D}(R) = 1/\ 8\pi(1-\nu)R^2$ and the normal n_ρ is taken at the point x.

A.2. **Series expansion of the hypersingular integrand $F^m_{\kappa\rho j}(\xi,\eta)$.** Applying the power series (4.8)-(4.11), we can determine the series expansion of the matrix $\mathcal{S}_{\kappa\rho\lambda}$ at η as follows:

$$\mathcal{S}_{\kappa\rho\lambda}(\xi,\eta)J(\xi) = {}^0a_{\kappa\rho\lambda} + {}^1a_{\kappa\rho\lambda}\delta + O(\delta^2)\,, \quad \text{(A.2)}$$

in which

$${}^0a_{111} = \frac{A_2}{A^2}\left(4A_1^2 + \left(2A_1^2 + 2A_2^2 - A^2\right)\mathfrak{K}_3\right) \quad \text{(A.3a)}$$

$${}^1a_{111} = -\left(\frac{2}{A^4}4CA_1^2A_2 + 8A_1A_2^3B_1 - 8A_1^2A_2^2B_2 - 8A^2A_1A_2B_1 + \right.$$
$$\left. + \left(A^4B_2 + 2CA_2^3 + 2CA_1^2A_2 - A^2A_1^2B_2 - 4A^2A_2^2B_2 - 3A^2A_1A_2B_1\right)\mathfrak{K}_3\right) \quad \text{(A.3b)}$$

$${}^0a_{112} = \frac{A_1}{A^2}\left(4A_2^2 + \left(2A_1^2 + 2A_2^2 - A^2\right)\mathfrak{K}_3\right) \quad \text{(A.3c)}$$

$${}^1a_{112} = -\frac{2}{A^4}\left(4CA_1A_2^2 + 8A_1^3A_2B_2 - 8A_1^2A_2^2B_1 - 8A^2A_1A_2B_2 + \right.$$
$$\left. + \left(A^4B_1 + 2CA_1^3 + 2CA_1A_2^2 - 4A^2A_1^2B_1 - A^2A_2^2B_1 - 3A^2A_1A_2B_2\right)\mathfrak{K}_3\right) \quad \text{(A.3d)}$$

$${}^0a_{211} = \frac{A_1}{A^2}\left(4A_2^2 - \left(2A_2^2 + 2A_1^2 - A^2\right)\mathfrak{K}_3\right) \quad \text{(A.3e)}$$

$${}^1a_{211} = \frac{2}{A^4}\left(-4CA_1A_2^2 - 8A_1^3A_2B_2 + 8A_1^2A_2^2B_1 + 8A^2A_1A_2B_2 + \right.$$
$$\left. + \left(A^4B_1 + 2CA_1^3 + 2CA_1A_2^2 - 4A^2A_1^2B_1 - A^2A_2^2B_1 - 3A^2A_1A_2B_2\right)\mathfrak{K}_3\right) \quad \text{(A.3f)}$$

$${}^0a_{212} = \frac{A_2}{A^2}\left(4A^2 - 4A_1^2 + A_3^2\mathfrak{K}_3\right) \quad \text{(A.3g)}$$

$${}^1a_{212} = \frac{2}{A^4}\left(4A^4B_2 + 8A_1^4B_2 + 4CA_1^2A_2 - 8A_1^3A_2B_1 - 12A^2A_1^2B_2 + 4A^2A_1A_2B_1 + \right.$$
$$\left. + \left(A^4B_2 - A^2A_1^2B_2 + A^2A_1A_2B_1\right)\mathfrak{K}_3\right) \quad \text{(A.3h)}$$

$$a^0_{121} = -\frac{A_1}{A^2}\left(4A^2 - 4A_2^2 + A_3^2\mathfrak{K}_3\right) \quad \text{(A.3i)}$$

$${}^1a_{121} = -\frac{2}{A^4}\left(4A^4B_1 + 8A_2^4B_1 + 4CA_1A_2^2 - 8A_1A_2^3B_2 - 12A^2A_2^2B_1 + 4A^2A_1A_2B_2 + \right.$$
$$\left. + \left(A^4B_1 - A^2A_2^2B_1 + A^2A_1A_2B_2\right)\mathfrak{K}_3\right) \quad \text{(A.3j)}$$

$$a^0_{122} = -\frac{A_2}{A^2}\left(4A_1^2 - \left(2A_2^2 + 2A_1^2 - A^2\right)\mathfrak{K}_3\right) \quad \text{(A.3k)}$$

$${}^1a_{122} = -\frac{2}{A^4}\left(-4CA_1^2A_2 - 8A_1A_2^3B_1 + 8A_1^2A_2^2B_2 + 8A^2A_1A_2B_1 + \right.$$
$$\left. + \left(A^4B_2 - A^2A_1^2B_2 - 4A^2A_2^2B_2 + 2CA_2^3 + 2CA_1^2A_2 - 3A^2A_1A_2B_1\right)\mathfrak{K}_3\right) \quad \text{(A.3l)}$$

$${}^0a_{221} = -\frac{A_2}{A^2}\left(4A_1^2 + \left(2A_1^2 + 2A_2^2 - A^2\right)\mathfrak{K}_3\right) \quad \text{(A.3m)}$$

$$
{}^{1}a_{221} = \frac{2}{A^4}\big(4CA_1^2A_2 + 8A_1A_2^3B_1 - 8A_1^2A_2^2B_2 - 8A^2A_1A_2B_1 + \\
+ \big(A^4B_2 + 2CA_2^3 + 2CA_1^2A_2 - A^2A_1^2B_2 - 4A^2A_2^2B_2 - 3A^2A_1A_2B_1\big)\,\mathfrak{K}_3\big) \tag{A.3n}
$$

$$
{}^{0}a_{222} = -\frac{A_1}{A^2}\left(4A_2^2 + \left(2A_1^2 + 2A_2^2 - A^2\right)\mathfrak{K}_3\right) \tag{A.3o}
$$

$$
{}^{1}a_{222} = \frac{2}{A^4}\big(4CA_1A_2^2 + 8A_1^3A_2B_2 - 8A_1^2A_2^2B_1 - 8A^2A_1A_2B_2 + \\
+ \big(A^4B_1 + 2CA_1^3 + 2CA_1A_2^2 - 4A^2A_1^2B_1 - A^2A_2^2B_1 - 3A^2A_1A_2B_2\big)\,\mathfrak{K}_3\big) \tag{A.3p}
$$

where $\mathfrak{K}_2 = 1/\ 8\pi(1-\nu)$ and $\mathfrak{K}_3 = 2(1-2\nu)$. In addition, exploiting equations (4.12)-(4.16), the Laurent series of $F^m_{\kappa\rho j}(\xi,\eta)$ in accordance with equation (4.17) is given in this form:

$$
F^m_{\kappa\rho j}(\xi,\eta) = \mathcal{S}_{\kappa\rho\lambda}(\xi,\eta)J(\xi)N_{\lambda j}(\xi) = \underbrace{\left[\frac{1}{A^2\mathfrak{K}_2}\,{}^{0}a_{\kappa\rho\lambda}\,{}^{0}N_{\lambda j}(\eta)\right]}_{{}^{-2}F^m_{\kappa\rho j}(\eta)}\delta^{-2} + \\
+ \underbrace{\left[\left(\frac{1}{A^2\mathfrak{K}_2}\,{}^{1}a_{\kappa\rho\lambda} - \frac{2C}{A^4\mathfrak{K}_2}\,{}^{0}a_{\kappa\rho\lambda}\right){}^{0}N_{\lambda j}(\eta) + \frac{1}{A^2\mathfrak{K}_2}\,{}^{0}a_{\kappa\rho\lambda}\,{}^{1}N_{\lambda j}(\eta)\right]}_{{}^{-1}F^m_{\kappa\rho j}(\eta)}\delta^{-1} + O(1) \tag{A.4}
$$

Journal of Computational and Applied Mechanics, Vol. 11., No. 1., (2016), pp. 67–76
DOI: 10.32973/jcam.2016.005

FE MODELLING OF A COUPLED THERMAL-ELASTIC-PLASTIC ANALYSIS IN A RAIL-WHEEL CONTACT

Péter. T. Zwierczyk and Károly Váradi
Department of Machine and Product Design
Budapest University of Technology and Economics
H-1111 Budapest, Műegyetem rkp. 3., Hungary
z.peter@gt3.bme.hu, varadik@eik.bme.hu

[Received: September 7, 2015. Accepted: December 18, 2015]

Dedicated to Professor Barna Szabó on the occasion of his eightieth birthday and to Professor Imre Kozák on the occasion of his eighty-fifth birthday

Abstract. The aim of our analyses was to model the process of the thermal micro-crack development on and under a railway wheel tread, equipped only with a disk brake during an intensive braking procedure. Considering the fact that the thermal micro-crack development is a complex problem, a multistage finite element modelling technique was developed. Using the new modelling approach, the heat and the thermal stress development can be observed between the wheel and the rail using thermal and coupled thermal-elastic-plastic FE simulations.

Keywords: Micro-crack development, heat and thermal stresses

1. Introduction

During intensive wheel-braking of the railway vehicles it appears that the wheel slides on the rail. While the macroscopic sliding speed is restricted it is not eliminated by the WSP (Wheel Slide Protection System). Through the sliding process considerable heat

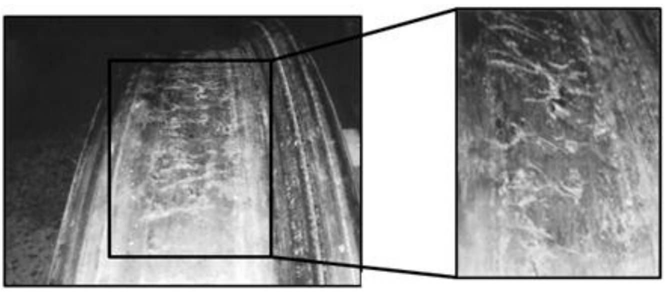

Figure 1. Highlighted thermal cracks on the surface of the wheel tread [1]

[1]Photo courtesy of BUTE Department of Aeronautics, Naval Architecture and Railway Vehicles

is generated between the connecting parts. This heat may cause micro-cracks on and under the wheel tread. These phenomena can be observed not only on vehicles equipped with brake pads but also on those with a disk brake. A great of research is focusing on the heat development between the wheel and the rail and the different defects of the railway wheels using various calculation methods. In order to analyse the contact temperature and the temperature fields of components in a relative sliding motion Knothe and Liebelt [1] used Laplace transformations combined with the method of Green's functions. They reduced the three-dimensional problem, as an approximation, to a two-dimensional one. Tanvir [2] also applied the Laplace transformation method to the determine the temperature on and under the wheel tread. A new mathematical model was developed to investigate the temperature distribution, in the case of rolling contact and at different slips, between the wheel and the rail by Spiryagin et al. [3]. Their investigation involved the one- and the so-called two-point contact cases as well.

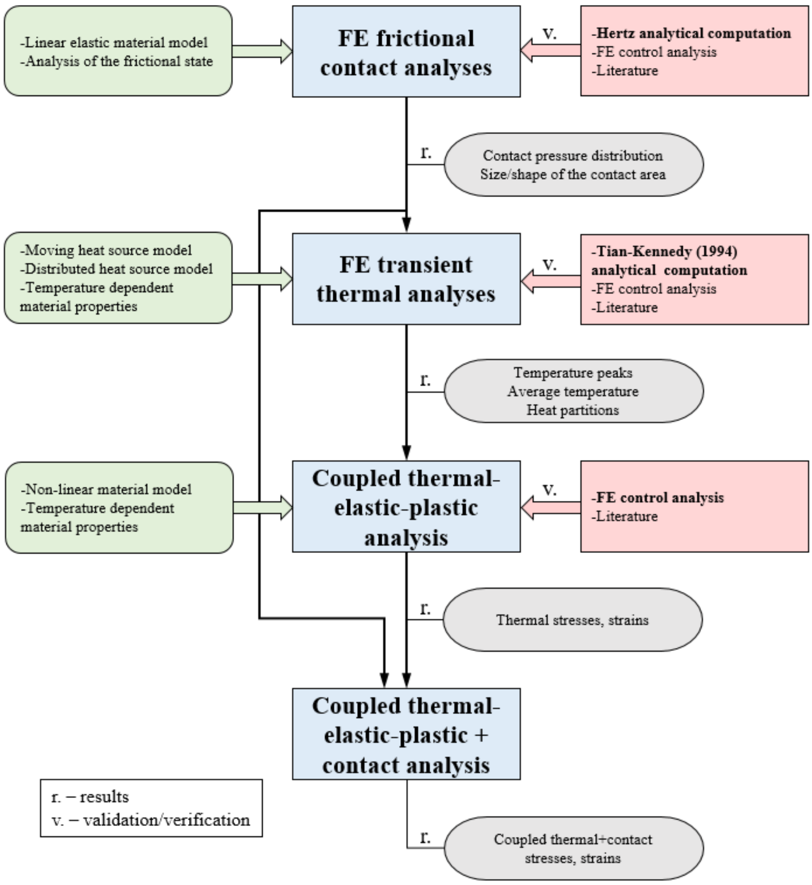

Figure 2. The schematic structure of the multistage FE modelling method [4, 5]

Beside the analytical calculation methods many authors used numerical models to analyse the temperature distribution. Gupta et al. [6] used both two- and three-dimensional FE models to analyse the temperature rise and distribution on and under the tread of a locomotive wheel in the case of different combinations of creep and adhesion. Ertz and Knothe [7] computed the maximum surface temperature during rolling contact with sliding friction between the wheel and the rail with semi-analytical and numerical methods. In addition they created a comparison of the previous results. Kennedy et al. [8], to determine the temperature distribution and the heat partition between the elements in frictional contact, used a transient FE model. Furthermore, the results were compared with many analytical solutions. Sábitz and Zobory [9] as well as Sábitz and Kolonits [10] also used FEM to investigate the temperature distribution on the surface of the wheel tread.

The finite element method is also popular in the case of the examination of the stress field caused by the temperature distribution. Wu et al. [11] using two-dimensional FEM model, analysed the residual stress and strain distributions on and under a rail head in the case of different loading cases and passes with or without thermal load. Furthermore Sábitz and Zobory [12], Peng et al. [13] and Peng et al. [14] also used the finite element method to investigate the thermal stress distribution in the case of a tread braked wheel in the same cases, allowing for the so-called "rail chill" effect. The finite element method is also used as a tool to investigate wheel defects (e.g. thermal fatigue cracks, rolling contact fatigue, etc.) together with experimental investigations. Makino et al. [15] analysed shelling as a typical rolling fatigue crack with FE method and with two cylindrical specimens. Similarly Kabo [16], Ringsberg and Lindbäck [17] and Pletz et al. [18] chose FEM to examine rolling fatigue during different situations. An experimental test equipment was used by Handa et al. [19] to examine the tread thermal crack development and propagation. The analysis involved not only the wheel–rail contact but also the tread breaking process. The same test apparatus was used by Handa and Morimoto [20] to investigate the dominant factor of thermal crack development and the possible countermeasures.

In our research a multistage finite element model was developed to investigate the complete background of the thermal micro-crack development on and under a wheel tread, equipped only with a cdisk brake under an intensive braking process. For the elaboration the ANSYS Workbench V14.5 software was used.

2. The structure of the multistage finite element model

Taking into consideration that the problem under examination is so complicated, the problem has been divided into several smaller tasks with several partial FE models. The analysis of the contact and the frictional state of a wheel–rail connection and the heat and the thermal stress generation between them were examined separately. To verify the new FE modelling method and validate the results, analytical and/or numerical methods were used at each model stage. The schematic structure of our multistage FE modelling method can be seen in Figure 2.

In the first stage a frictional contact analysis was performed using a simplified segmented wheel-rail geometry. During the calculation half a model was used. In the following stages the size of the models were also modified. In the course of the thermal and the coupled analyses, a 14°-piece of a railway wheel with simplified geometry and a 175-mm long rail, compliant with the UIC 60E1 profile standard (both also segmented) were examined (Zwierczyk and Váradi [21]).

In the different computational steps, different basic contact assumptions were used. During the computation of the contact, real-life contact conditions, an elliptical contact patch and parabolic contact pressure distribution (analytical models), caused by the bodies in contact, were taken into consideration. During the transient thermal and the coupled transient thermal-elastic-plastic analyses the previously computed elliptical contact area was considered to be rectangular with uniform pressure distribution to compute the heat source. Through the combined thermal and contact analysis the formerly described rectangular contact patch with uniform pressure distribution (due to the heat source) and a parabolic pressure distribution (obtained from the contact computation) were used (Zwierczyk [4]).

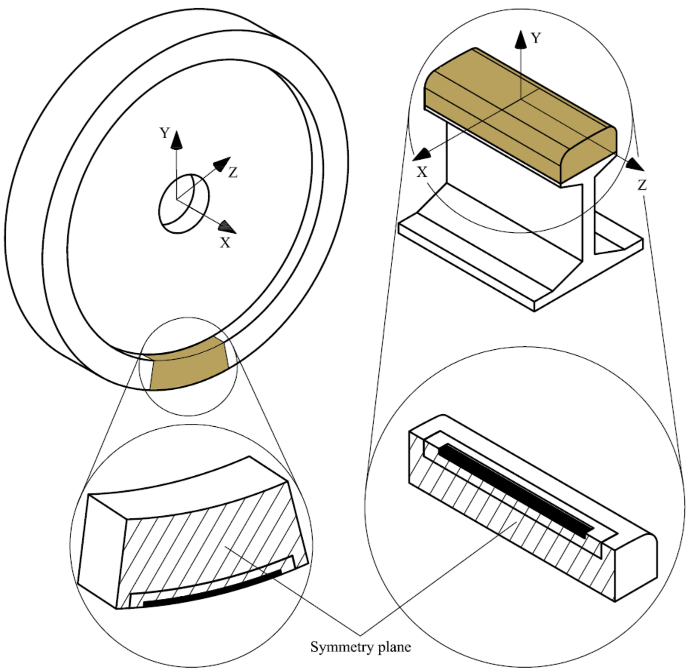

Figure 3. The initial geometries, used during the thermal and the coupled analyses [4]

3. The results

As a result of the frictional contact analysis the size and the shape of the contact zone, furthermore the distribution of the contact pressure, which was essential to the examination of the temperature field were determined. The significant size of the contact ellipse radiuses and the contact pressure distribution can be seen in Figure 5. Besides, the complete slipping procedure of the wheel on the rail could also be investigated, also with the displacement of the contact patch within the contact zone (Zwierczyk and Váradi [21]). As was mentioned before, all stages were validated and/or

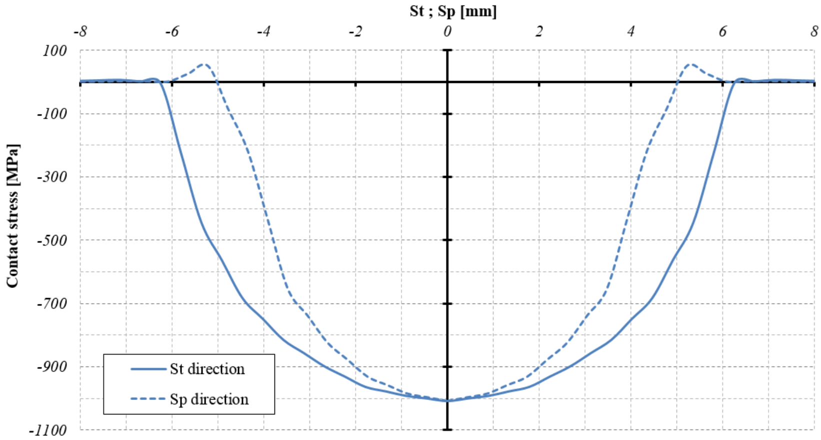

Figure 4. Contact pressure distribution and the size of the contact patch on the wheel tread (St; Sp illustrated in Figure 7) (Zwierczyk and Váradi [21]

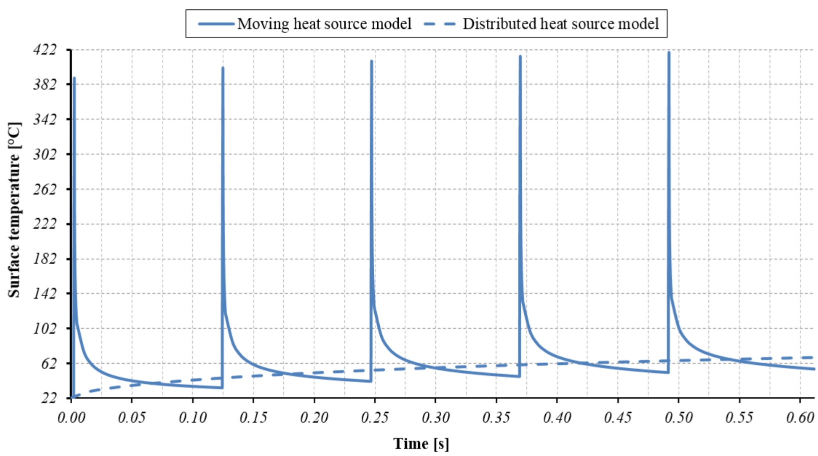

Figure 5. Temperature distribution vs. time on the wheel side during 5 revolutions (Zwierczyk [4])

verified with different analytical and numerical methods. In the case of the contact pressure and the size of the contact patch the Hertz theory was used to validate the results. To verify the slipping procedure and the displacements, a simplified FE control model was built (Zwierczyk [4]).

In the next step thermal analyses were performed both the wheel and the rail. Moving and distributed heat source models were built (distributed heat source models provide the "average temperature" during each revolution while moving heat source models provide information about the temperature development moment by moment in the vicinity of the contact area). As a result of these analyses the temperature distribution on and under wheel and the rail tread, furthermore the average base temperature of both of the contacting elements were determined (Zwierczyk and Váradi [22]; Zwierczyk and Váradi [23]). The heat sources were calculated using the previous contact pressure and contact patch. The thermal computation validation is based on Tian at al's [5] analytical solution, some of the results were compared with experimental data and measurement results from the literature.

For the third stage of Figure 2, a coupled thermal-elastic-plastic FE analysis was performed. With the help of this stage the stress field caused by the temperature distribution could be calculated. Figure 7 shows the von Mises stress distribution under the wheel tread. As can be seen in the figure, in the t12 time instant when heat source is just passing through the sampling line, the von Mises stress reaches the yield strength and a small plastic zone appears on and under the surface of the wheel tread. The verification of the model was elaborated by a control FE computation using submodels.

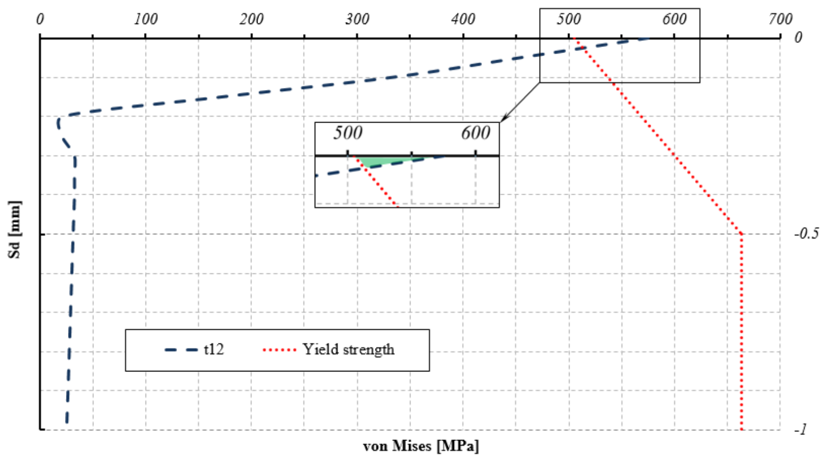

Figure 6. Distribution of von Mises stress below the tread (Sd illustrated in Figure 7) during the 1st revolution (the thin dotted line represents the yield strength as a function of temperature, t12 indicates the time instant when the von Mises stress reaches its maximum)

In the last stage a combine contact-thermal-elastic-plastic model was elaborated using the contact pressure, calculated in the first stage. The contact pressure was applied as a load together with the heat source, as can be seen in Figure 7. Results show that because of the common effect of the thermal and mechanical load the previously computed plastic zone becomes larger and reaches deeper layers of the wheel as can be seen in Figure 8. This plastic zone may contribute to the development and the

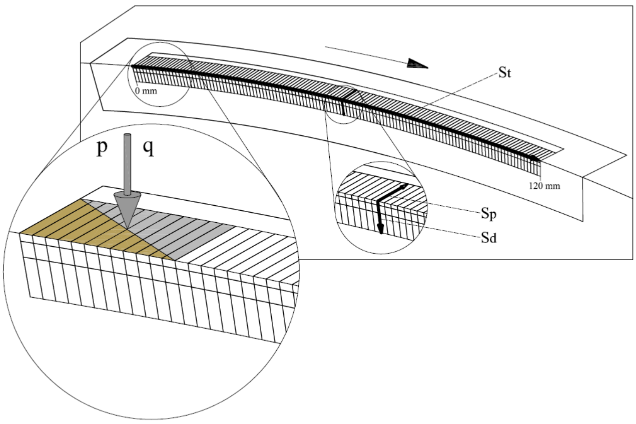

Figure 7. Method of entering heat flux and contact pressure together and the locations of the sample lines (p-contact pressure; q-heat source; sample line St according to the direction of sliding; sample line Sd in the direction of depth; sample line Sp in direction across the tread) (Zwierczyk [4])

appearance of the micro-cracks on and under the surface. The calculation method was verified with control FE analyses and the results were compared with measurements which are available in the literature.

4. Conclusions

The joint effect of contact and thermal stresses was studied with transient thermal-elastic-plastic FE models. The coupled stress state caused plastic behavior in deeper layers compared to the "pure" thermal stress computations. The former stress maximums migrated from the surface to deeper layers (0.2–0.3 mm under the surface). The results show that the two independent effects, i.e. the "pure" thermal stress and contact stress generation, should be analysed at the same instant because of their joint impact on micro-crack development. Our intention was to present the numerical algorithm (i.e. multistage FE modelling method), introduced in [24]. The thermal aspect of the thesis was published in [22]. The coupled aspect of the transient thermal and the non-linear thermal stress analysis was published in [21]. Combined contact+thermal stress results have not been published yet. Each stage of the multistage FE modelling

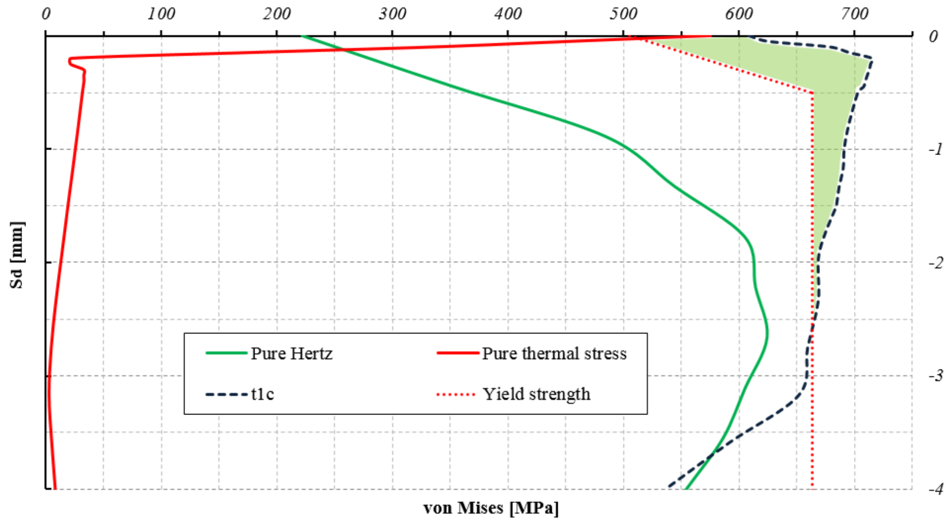

Figure 8. Distribution of von Mises stress below the tread (Sd illustrated in Figure 7) under different loading conditions during the 1st revolution (the red dotted line represents the yield strength as a function of temperature, t1c represents the common effect of the thermal and mechanical load)

method was validated and/or verified with analytical and numerical analyses, furthermore the results were confronted with the results of measurements which can be found in the literature. The results shows that with the help of these coupled models the background of this thermo-mechanical problem can be investigated using a normal personal computer.

References

1. Knothe, K. and Liebelt, S.: Determination of temperatures for sliding contact with applications for wheel-rail systems. *Wear*, **189**, (1995), 91–99.
2. Tanvir, M. A.: Temperature rise due to slip between wheel and rail—an analytical solution for hertzian contact. *Wear*, **61**, (1980), 295–308.
3. Spiryagin, M., Lee, K. S., Yoo, H. H., Kashura, O., and Popov, S.: Numerical calculation of temperature in the wheel–rail flange contact and implications for lubricant choice. *Wear*, **268**, (2010), 287–293.
4. Zwierczyk, P. T.: *Thermal and stress analysis of a railway wheel rail rolling sliding contact.* Ph.D. thesis, Budapest University of Technology and Economics, 2015.
5. Tian, X., Kennedy, J., and Francis, E.: Average flash temperatures in sliding contacts. *J. Tribol.*, **116**, (1994), 167–174.
6. Gupta, V., Hahn, G. T., Bastias, P. C., and Rubin, C. A.: Calculations of the frictional heating of a locomotive wheel attending rolling plus sliding, 4th International

Conference on Contact Mechanics and Wear of Rail-Wheel Systems. *Wear*, **191**, (1996), 237–241.

7. Ertz, M. and Knothe, K.: A comparison of analytical and numerical methods for the calculation of temperatures in wheel/rail contact. *Wear*, **253**, (2002), 498–508.
8. Kennedy, T. C., Plengsaard, C., and Harder, R. F.: Transient heat partition factor for a sliding railcar wheel. *Wear*, **261**, (2006), 932–936.
9. Sábitz, L. and Zobory, I.: On simulating the thermal conditions of martensite formation on railway wheel treads. In *Proceedings of the Second International Conference on Railway Technology: Research, Development and Maintenance*, Civil-Comp Press, Stirilingshire, Scotland, 2014, pp. 103–113.
10. Sábitz, L. and Kolonits, F.: Finite element and analytical computation of flash temperature. *Civ. Eng.*, **58**, (2014), 267–278.
11. Wu, L., Wen, Z., Li, W., and Jin, X.: Thermo-elastic–plastic finite element analysis of wheel/rail sliding contact. In *Proceedings of the 8th International Conference on Contact Mechanics and Wear of Rail/Wheel Systems, Florence*, 2011, pp. 437–443.
12. Sábitz, L. and Zobory, I.: Finite element modelling of the thermoelastic processes in tread-braked wheels, Conference on Railway Bogies and Running Gears, Budapest, Hungary, 2010. pp. 103–113.
13. Peng, D., Jones, R., and Constable, T.: A study into crack growth in a railway wheel under thermal stop brake loading spectrum. *Eng. Fail. Anal.*, **25**, (2012), 280–290.
14. Peng, D., Jones, R., and Constable, T.: An investigation of the influence of rail chill on crack growth in a railway wheel due to braking loads. *Eng. Fract. Mech.*, **98**, (2012), 1–14.
15. Makino, T., Kato, T., and Hirakawa, K.: The effect of slip ratio on the rolling contact fatigue property of railway wheel steel. *Int. J. Fatigue*, **36**, (2012), 68–79.
16. Kabo, K.: Material defects in rolling contact fatigue — influence of overloads and defect clusters. *Int. J. Fatigue*, **24**, (2002), 887–894.
17. Ringsberg, J. W. and Lindbäck, T.: Rolling contact fatigue analysis of rails including numerical simulations of the rail manufacturing process and repeated wheel-rail contact loads. *Int. J. Fatigue*, **25**, (2003), 547–558.
18. Pletz, M., Daves, W., Yao, W., Kubin, W., and Scheriau, S.: Multi-scale finite element modelling to describe rolling contact fatigue in a wheel–rail test rig. *Tribol. Int.*, **80**, (2014), 147–155.
19. Handa, K., Kimura, Y., and Mishima, Y.: Surface cracks initiation on carbon steel railway wheels under concurrent load of continuous rolling contact and cyclic frictional heat. *Wear*, **268**, (2010), 50–58.
20. Handa, K. and Morimoto, F.: Influence of wheel/rail tangential traction force on thermal cracking of railway wheels. *Wear*, **289**, (2012), 112–118.
21. Zwierczyk, P. T. and Váradi, K.: Frictional contact fe analysis in a railway wheel-rail contact. *Periodica Polytechnica Mech. Eng.*, **58**, (2014), 93–99.
22. Zwierczyk, P. T. and Váradi, K.: Thermal stress analysis of a railway wheel in sliding-rolling motion. *J. Tribol*, **136**, (2014), 031401–1 – 031401–8.

23. Zwierczyk, P. T. and Váradi, K.: Thermal analysis of a railway wheel-rail connection in sliding/rolling motion. The Tenth International Symposium on Tools and Methods of Competitive Engineering (TMCE 2014), Budapest, Hungary, 2014, pp. 1405–1412.

24. Zwierczyk, P. T.: *Thermal and stress analysis of a railway wheel rail rolling sliding contact*. Ph.D. thesis, Budapest University of Technology and Economics, 2015.

Journal of Computational and Applied Mechanics, Vol. 11., No. 1., (2016), pp. 77–94
DOI: 10.32973/jcam.2016.006

INVESTIGATION OF THE APPLICABILITY AND EFFICIENCY OF DIFFERENT MATHEMATICAL MODELING AND NUMERICAL SIMULATION METHODS FOR SOIL–TOOL INTERACTION

András Zachár, István Keppler and István Oldal
Institute of Mechanics and Machinery, Szent István University
Páter K. u. 1., H-2103 Gödöllő, Hungary
Oldal.Istvan@gek.szie.hu

[Received: September 18, 2015. Accepted: February 22, 2016]

Dedicated to Professor Barna Szabó on the occasion of his eightieth birthday and to Professor Imre Kozák on the occasion of his eighty-fifth birthday

Abstract. Three different mathematical modeling and numerical simulation approaches – the Finite Volume Method (FVM-CFD), Smoothed-Particle Hydrodynamics-Finite Element Method (SPH-FEM) and the Discrete Element Method (DEM) – are used to predict the draft forces of a plow moldboard interacting with cohesive granular material. In situ draft force and pressure field measurement data and simulation results are compared to investigate the efficiency of the applied mathematical models and numerical methods to predict the behavior of the soil flow around the studied plow moldboard. In the case of SPH-FEM modeling three-dimensional explicit dynamic computations have been carried out in AUTODYN ANSYS Workbench 12 environment. The soil has been modeled as SPH solid body. Failure behavior of the soil has been described with the Drucker-Prager model. In the case of DEM modeling, the soil has been described as an assembly of large number of individual particles. For modeling the mechanical behavior of the soil, the Hertz-Mindlin with bonding contact model was used. The micromechanical parameters describing the granular assembly have been determined by a calibration method based on the standard shear test. In the case of FVM-CFD modeling a three dimensional, multiphase flow computations have been carried out in the Ansys CFX 11 environment. The developed soil stress and pressure field on the surface of the plow moldboard and the induced draft force have been studied to gain more information about the entire physical process. The rheological behavior of the soil has been characterized as a Bingham plastic model. Comparison of the efficiency of different simulation approaches has been carried out to gain information on the efficiency of the different mathematical modeling techniques and the numerical calculations.

Keywords: Soil-tool interaction, finite volume method, smoothed-particle hydrodynamics method, discrete element method

1. Nomenclature

Latin symbols

$A(\mathbf{r})$	arbitrary scalar or vector field of a physical quantity (SPH)
$\langle A(\mathbf{r})\rangle$	approximation of the field variable (SPH)

c	cohesion (Pa) (SPH)
C_h, C_j	speed of sound at the i-th and j-th particles (m s^{-1}) (SPH)
E	specific internal energy (J) (SPH)
E_0, E_1, E_3	Young's moduli (GPa) (DEM)
F_{TD}	total draft exerted on the tillage tool (N)
G_0, G_1, G_3	equivalent sheer stresses (GPa) (DEM)
h	smoothing length (m) (SPH)
k	mean viscosity value of the non-Newtonian material model (Pa s) (CFD)
m_i	mass of th i-th elements (kg) (SPH)
$n, m = 1, 2, 3$	indices for spatial directions
$\mathbf{r}_i$	mass center of the i-th element
u^n, u^m	spatial components of the velocity vector (m/s) (SPH, CFD)
x^m	spatial coordinate (m) (SPH, CFD)
$w(\mathbf{u}, h)$	interpolation kernel function (SPH)
Greek symbols	
α	share angle (deg)
β	rake angle (deg)
γ	sheer strain rate of the soil (s^{-1}) (CFD)
$\delta(\mathbf{r})$	Dirac delta function (SPH)
ϕ	angle of internal friction
η	dynamic viscosity of the fluid (air, soil) (N s m^{-2}, Pa s) (CFD)
μ_r, μ_ρ	coefficient of the rolling and static friction (DEM)
ρ	density function of the fluid (air, soil) (kg/m^3) (CFD, SPH)
σ	normal stress (Pa) (SPH)
σ^{nm}	an element of the Cauchy stress tensor (Pa) (SPH)
τ	shear strength (Pa) (SPH)
τ_0	yield stress (soil) (Pa) (CFD)

2. Introduction

The study of tillage tool interaction on different types of soil is an important phase of tool design and development. The total draft of a tillage tool is an important factor of the overall efficiency of soil tillage. Moldboard plowing is one of the most important and most energy consuming processes of agricultural production; for this reason adequate knowledge on draft forces and the developing pressure field on the surface of the tillage tool is necessary to improve the efficiency of the design process. Until now large amount of research has been conducted to study the dependency of draft force on the soil properties and tillage tool geometry. Generally three different properties are used to characterize the efficiency of a tillage tool, according to Karmakar and Kushwaha et al. [1]. These are the draft to operate the tillage tool – in this case the plow – the soil loosened and the total energy requirement. Several different attempts have been carried out in the last couple of decades to develop an analytical description of the soil tool interaction and formulation of the draft force. According to Godwin's review [2] the following two components of the soil forces must be taken into account:

the horizontal (draft) force that is required to pull the tool through the soil and the vertical force, which assists or prevents the tool's penetration into the soil. These forces are the function of rake angle β, tine depth d, tool width w and tillage velocity v. Most of the analytical predictions of draft forces acting on wide tines are based on the equation presented by Godwin and O'Dogherty [3] which is sometimes referred as the Universal Earthmoving Equation

$$F = \left(\gamma d^2 N_\gamma + cdN_c + c_a dN_{ca} + qdN_q + \frac{\gamma v^2}{g} dN_a\right) w \tag{1}$$

where F is the draft force, γ is the specific weight of soil, g is the gravitational acceleration, c is cohesion, c_a is adhesion, q is surcharge pressure and v is the working velocity. N_γ, N_c, N_{ca}, N_q and N_a are dimensionless factors. According to Onwualu and Watts [4] the average deviation of the analytically predicted draft force from the experimental one varies from 6% to 160%. The aim of this study is to test the applicability of different soil modeling methodology and numerical approaches simulating the soil moldboard plow interaction. This paper presents a comparison and evaluation of the studied mathematical models and numerical methods simulating a plowing process.

3. Mathematical models

3.1. **Main features of the two models considered.** The mechanical behavior of agricultural soils is an extremely difficult area of research due to the complexity of soil parameters and operating conditions. Two basically different mathematical modeling approaches exist to describe the behavior of soil flow: these are continuum and discrete element modeling. The continuum model is based on the Eulerian modeling concept of the solid and fluid material assembled with infinitely small deformable and flexible cubes. The discrete element method is based on Lagrangian description, i.e., the mechanical interaction and motion of the individual particles is modeled.

3.2. **Finite volume method (continuum modeling).** Many different studies have shown that agricultural soils are approximately show brittle fracture mechanical behavior during soil tillage (see Chandler [5], Aluko and Chandler [6]). Several other studies hypothesized different type of soil mechanical behavior: the visco-elastic model has been used and studied by Kocher and Summers [7], the hypo-elastic model has been investigated by Rosa and Wulfsohn [8] and the elastic- perfectly plastic model has been tested by Mouazen and Neményi [9]. Soil failure and pressure patterns for flat cutting blades in soils of different strengths have been examined by Elijah and Weber [10] to gain more knowledge about the soil cutting blade interaction. Finite element modeling of the interaction of the cutting edge of tillage implements with soil has been conducted and the results compared with previously measured tillage forces (see Fielke [11]). In several different investigations the method of computational fluid dynamics (CFD) has been used to model soil tillage tool interaction. Formato et al. [12] determine a virtual material able to quantitatively reproduce the distribution of pressure field on the working surface of a plow. Karmakar et al. [1] report a successful application of the Bingham plastic model to investigate the interaction between the soil and a flat tillage tool in a wide range of tool operating velocities. The physical problem is a steady, three-dimensional flow of a two-phase fluid where the first one is the air and the other one is the soil phase. The momentum equation of the fluid is based on the three-dimensional Navier-Stokes equations. A simple finite volume method is applied to solve the momentum and continuity equations. The dependent variables that describe the present flow situation are the pressure P and the velocity components U_1, U_2, U_3 in the x_1, x_2, x_3 directions, respectively. The following set of partial differential equations for U_1, U_2, U_3 and P as functions of x_1, x_2, x_3 describes the flow field around the moldboard plow in steady state flow condition.

(a) Continuity equation. By using tensorial notations in a Cartesian coordinate system for the continuity equation we can write

$$\frac{\partial \rho}{\partial t} + \frac{\partial}{\partial x_i} \rho U_i = 0 \,. \tag{2}$$

(b) Momentum equations. The following equation system is the representation of the momentum equations in the Cartesian coordinate system:

$$\frac{\partial}{\partial t} \rho U_j + \frac{\partial}{\partial x_i} \rho U_j U_i = -\frac{\partial P}{\partial x_j} + \frac{\partial}{\partial x_i} \left(\eta \frac{\partial U_j}{\partial x_i} \right) \tag{3}$$

Here η is the dynamic viscosity and ρ stands for the density.

(c) Applied material models. Modeling the mechanical behavior of different soil types is a difficult task because of the extreme complexity of soil structure. Mechanical properties of different soil types depend on the soil texture, moisture content, soil compaction level and several other factors occurring in the field. The applied material model in the numerical calculations is the Bingham plastic model, which considers the cohesion effect of the soil. A Bingham plastic substance is a viscoplastic material that behaves as a rigid body at low stresses (below the yield stress). Above the yield stress the Bingham plastic material flows as a viscous fluid. Bingham plastic materials require two distinct parameters, the yield stress and the plastic viscosity. Equation (4) shows the mathematical formulation of the Bingham fluids:

$$\gamma = \frac{\partial U_i}{\partial n} = \begin{cases} 0 \quad , & |\tau_{i,j}| < \tau_0 \,, \\ \dfrac{\tau_{i,j} - \tau_0}{\eta} , & |\tau_{i,j}| \geqslant \tau_0 \end{cases} \tag{4}$$

where τ_0 is the yield stress of the soil, η is the plastic viscosity and $\partial U_i / \partial n$ is the shear strain rate.

(d) Domain discretization and the applied computational grids. A schematic diagram of the plow indicating one of the applied grids for the computational domain is shown in Figure 1. The size of the calculation domain is chosen so that the wall effect can be neglected and some test calculations have been

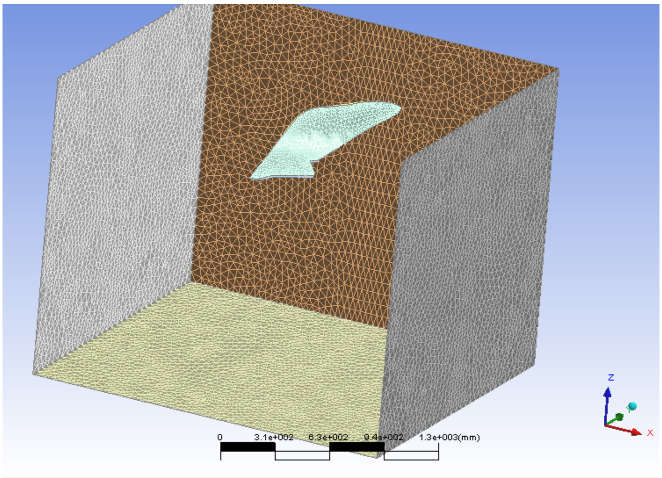

Figure 1. Computational domain

carried out to check the independence of the numerical result from the horizontal and vertical size of the domain. A careful check for the grid-independence of the numerical calculation has been created to ensure the accuracy and validity of the numerical calculations. Four different grids have been used to check the grid independence of the numerical scheme. The total draft of the plow has been applied to test the grid independence of the numerical calculations.

Table 1. Draft force and its relative error on the grids studied

Studied grids	I.	II.	III.	IV.
(Number of cells)	332 5486	591 6506	731 7622	1259 1842
Draft force F [N]	4208.17	4191.27	4178.19	4176.81
Relative error of the force F $100 \left\lvert \frac{F_{\text{coarser}} - F_{\text{finest grid}}}{F_{\text{finest grid}}} \right\rvert \%$	0.750	0.346	0.033	–

The generated grid is much finer near the leading edge of the plow-share than near the outer boundary of the computational domain. Comparison of the results of the calculation on the different grids is shown in Table 1.

Relative error was calculated according to the assumption that the result of the finest grid is approximately ideal. The calculated results show that the difference between the induced draft forces on the finest grids is less than 0.03%. This means that a grid resolution for the applied calculation domain finer than the third (III) grid is acceptable to produce physically realistic calculation results independent from the numerical grid.

(e) Multiphase flow computation, initial and boundary conditions. The investigated flow situation is a free surface flow problem which is a special case of multiphase flow computation where the fluids are separated by a distinct resolved interface. Both fluids (soil and air) share a common flow field. The working fluids are not mixed in the micro-scale rather they are mixed on a macroscopic scale with a discernible interface between the fluids. A homogeneous multiphase model has been incorporated into the flow simulation because the interface between the two fluids remains well defined and none of the dispersed phase becomes entrained in the continuous phase. The soil flow on the upstream side of the plow is subcritical and the downstream conditions are not known but can be estimated. Simulation of free surface flow usually requires defining boundary and initial conditions to set up appropriate pressure and volume fraction fields. Simulating the soil-tool interaction the following conditions are set. At the inlet boundary the volume fraction above the free surface is 1 for air and 0 for soil and below the free surface it is 0 for air and 1 for soil. Furthermore the height of the soil at the inlet and outlet locations is defined with $h_{\mathrm{in}} = 0.3$ m and $h_{\mathrm{out}} = 0.3$ m. With the defined height of the soil in the computation domain the inlet, outlet and initial pressure distribution can be specified $P_{up} = \rho_{\mathrm{soil}}\, g\, h_{\mathrm{in}}$, $P_d = \rho_{\mathrm{soil}}\, g\, h_{\mathrm{out}}$ where P_{up} and P_d are the upstream and downstream pressure at the inlet and outlet. The initial velocity field is zero everywhere in the calculation domain. A uniform, constant velocity profile is assumed at the inlet position. The gradient of the velocity profile is assumed to be zero at the end of the outlet location. A free-slip boundary condition has been applied at the bottom and the left and right wall of the computational domain. At the top of the calculation domain a free-surface boundary condition is specified. The initial values of the air and soil volume fraction are also supplied with an assumption that the virtual field contains a furrow before the plow in the appropriate location.

3.3. **Discrete element method (discrete element modeling).** By the use of Discrete Element modeling technique (DEM), the problem is solved by applying and solving the equation of motion on each individual particle of the bulk material assembly [13]. For modeling the mechanical behavior of the soil, EDEM has been applied as a discrete element software using “the Hertz-Mindlin with bonding” contact model [14]. In this model, the particles are glued with a finite sized bond. In the discrete element model from the beginning of the simulation until “turning on the bonded contacts” the simulation evaluates the contact forces according to the Hertz-Mindlin no slip contact model: the material and interaction parameters have their effect on the normal- and tangential forces. The normal force has the following form

$$F_n = \frac{4}{3} E_0 \delta^{\frac{3}{2}} \sqrt{R_0} - 2\sqrt{\frac{5}{6}} \frac{\ln C_r}{\sqrt{\ln^2 C_r + \pi^2}} \sqrt{2E_0}\, \sqrt[4]{R_0 \delta} \sqrt{m_0} v_{\mathrm{nrel}} \tag{5}$$

where

$$\frac{1}{E_0} = \frac{1-\nu_1^2}{E_1} + \frac{1-\nu_2^2}{E_2}$$

is the equivalent Young modulus of the two interacting soil particles and δ is the overlap between these two soil particles. This normal overlap represents the normal deformation of a particle. The normal overlap δ between two particles i and j at positions x_i and x_j (where $x_j - x_i$ is the distance measured on the line connecting the centers of the two overlapping particles) with radii R_i and R_j is defined as: $\delta = R_i + R_j - (x_j - x_i)$.

$$R_0 = \frac{R_1 R_2}{R_1 + R_2} \quad \text{and} \quad m_0 = \frac{m_1 m_2}{m_1 + m_2}$$

are the equivalent radius and mass while v_{rel} is the relative velocity of the soil particles. The tangential force is given by the following equation

$$F_t = -8G_0\sqrt{R_0\delta}\delta_t - 2\sqrt{\frac{5}{6}}\frac{\ln C_r}{\sqrt{\ln^2 C_r + \pi^2}}\sqrt{2G_0}\sqrt[4]{R_0\delta}\sqrt{m_0}v_{\mathrm{trel}} \tag{6}$$

where

$$\frac{1}{G_0} = \frac{2-\nu_1}{G_1} + \frac{2-\nu_2}{G_2}$$

is the equivalent shear modulus of the two interacting soil particles, δ_t is the tangential overlap between the two particles and v_{trel} is the tangential component of the relative velocity of the soil particles. The tangential overlap is the tangential displacement of the contact point up to the point at which the contact ends or the particle begins to roll or slip. The tangential overlap represents the tangential deformation of a particle. The tangential force is limited by the Coulomb friction $\mu_s F_n$ where μ_s is the coefficient of static friction. The moment from rolling friction is $M_r = -\mu_r F_N R_i \omega_i$, where R_i is the distance of the contact point from the centre of the i-th soil particle and ω_i is the unit angular velocity vector, which is a dimensionless quantity representing only the direction of rotation of the i-th soil particle. μ_r is the coefficient of rolling friction. The tangential force also has moment on the particle: $M_t = F_t R_i$. From $t > t_{\mathrm{bond}}$ (from that time when bonding is "turned on", i.e., the particles are glued together) the bonding forces/moments acting on the particles are set to zero initially, and after that are incremented every time step:

$$\delta F_n = -v_n S_n A \delta t\,, \quad \delta F_t = -v_t S_t A \delta t\,, \quad \delta M_n = -\omega_n S_t J \delta t\,, \quad \delta M_t = -\omega_t S_n \frac{J}{2}\delta t \tag{7}$$

where

$$A = R_B^2 \pi\,, \quad J = \frac{1}{2} R_b^4 \pi\,.$$

R_B is the radius of the bonding glue, S_n, S_t are the normal and shear stiffness per unit area, δt is the time step, v_n, v_t are the normal and tangential velocities of the particles and ω_n, ω_t are the normal and tangential components of the angular velocity vector. The bond is broken when the normal and tangential stresses exceed some predefined value:

$$\sigma_{\max} < -\frac{F_n}{A} + \frac{2M_t}{J}R_B\,, \quad \tau_{\max} < -\frac{F_t}{A} + \frac{M_t}{J}R_B\,. \tag{8}$$

These bonding forces/torques are added to the standard Hertz-Mindlin forces. During the simulations, the linear and angular momentum theorem is used to write the equation of motion for all the individual particles, resulting in a large number of differential equations to be solved in a sufficiently large number of time steps. The applied time step has great impact on the stability of the numerical calculation. For the simulation 25% of the Rayleigh-type time step has been selected:

$$\delta t = 0.25 T_R = 0.25 \cdot (0.1631\nu + 0.8766)^{-1}\, \pi R \left(\frac{\rho_p}{G_p}\right)^{\frac{1}{2}} . \tag{9}$$

3.4. **Smoothed-particle hydrodynamics method.** The smoothed particle hydrodynamics method was originally invented by Monaghan and Gingold [15] for astrophysical applications. The SPH method has been successfully applied to several different impact problems since that, for example ballistic impact problems have been investigated by Hayhurst et al. [16], a pseudo-spring based fracture model of impact dynamics was studied by Chakraborty and Shaw [17], and it was applied to study complex fluid-solid surface interactions (see Yang et al. [18]). The SPH method has been found to be useful to study soil flow behavior and interaction with other bodies or fluids. Bui et al. [19] carried out a numerical simulation to investigate the soil–water interaction by the SPH method. Lu et al. [20] created a comparative study of a buried structure in soil subjected to blast load. SPH is effective and accurate at modeling material deformation as well as adaptable in terms of specific material models and besides to solve computational fluid dynamic problems, it can be also applied solving continuum mechanics problems with large deformations like machining problems. Calamaz et al. [21] studied the tool wear effect through a comparison between experiments and SPH numerical modeling of machining hard materials. Agricultural application is a new area of SPH application.

The basic concept of SPH is that the method does not use finite elements and mesh during discretization. SPH model contains only particles. These particles are not bodies (like discrete elements) but interpolation points (like nodes of a finite element). SPH involves the motion of a set of points. Points have masses and velocity and these values are known. Any field can be described with Dirac delta function:

$$A(\mathbf{r}) = \int A(\mathbf{r}')\, \delta(\mathbf{r} - \mathbf{r}')\, \mathrm{d}\mathbf{r}' \tag{10}$$

Function $\langle A(\mathbf{r})\rangle$ is an approximation of this field

$$\langle A(\mathbf{r})\rangle = \int A(\mathbf{r}')\, w(\mathbf{r} - \mathbf{r}', h)\, \mathrm{d}\mathbf{r}' \tag{11}$$

where $w(\mathbf{u}, h)$ is an interpolation kernel function with the following properties:

$$\int w(\mathbf{u}, h)\, \mathrm{d}\mathbf{u} = 1 \tag{12a}$$

$$w(\mathbf{u}, h) \xrightarrow[h \to 0]{\delta} (\mathbf{u}) \tag{12b}$$

$$w(\mathbf{u}, h) = 0 \quad \text{if} \quad |\mathbf{u}| > h \tag{12c}$$

where h is the smoothing length. There are infinitely many possible kernels. The following manipulation, which does not change the value of integral (11), is a useful one:

$$\langle A(\mathbf{r})\rangle = \int \frac{A\left(\mathbf{r}'\right)}{\rho(\mathbf{r}')} w\left(\mathbf{r}-\mathbf{r}', h\right) \rho(\mathbf{r}')\,\mathrm{d}\mathbf{r}' \,. \tag{13}$$

Divide the body into N small volume elements. The mass of the i-th element is m_i and the mass center is $\mathbf{r}_i$. Utilizing the quantities introduced we get integral (13) in the form

$$\langle A(\mathbf{r})\rangle = \sum_{i=1}^{N} m_i \frac{A\left(\mathbf{r}_i\right)}{\rho(\mathbf{r}_i)} w\left(\mathbf{r}-\mathbf{r}_i, h\right) \,. \tag{14}$$

Conservation equations of continuum mechanics for mass, momentum and energy are

$$\frac{\mathrm{d}\rho}{\mathrm{d}t} = -\rho \frac{\partial u^m}{\partial x^m} \,, \tag{15}$$

$$\frac{\mathrm{d}U^n}{\mathrm{d}t} = -\frac{1}{\rho}\frac{\partial \sigma^{nm}}{\partial x^m} \,, \tag{16}$$

$$\frac{\mathrm{d}E}{\mathrm{d}t} = -\frac{\sigma^{nm}}{\rho}\frac{\partial u^n}{\partial x^m} \tag{17}$$

where ρ is the density, E is the specific internal energy. $n, m = 1, 2, 3$ are indices for three spatial directions. x^m is spatial coordinate, u^n, u^m are the spatial components of the velocity vector and σ^{nm} is an element of the Cauchy stress tensor.

4. Model validation

4.1. **Measurements.** It is important to verify the applicability of the different mathematical models and the entire numerical approaches to simulate the soil–plow

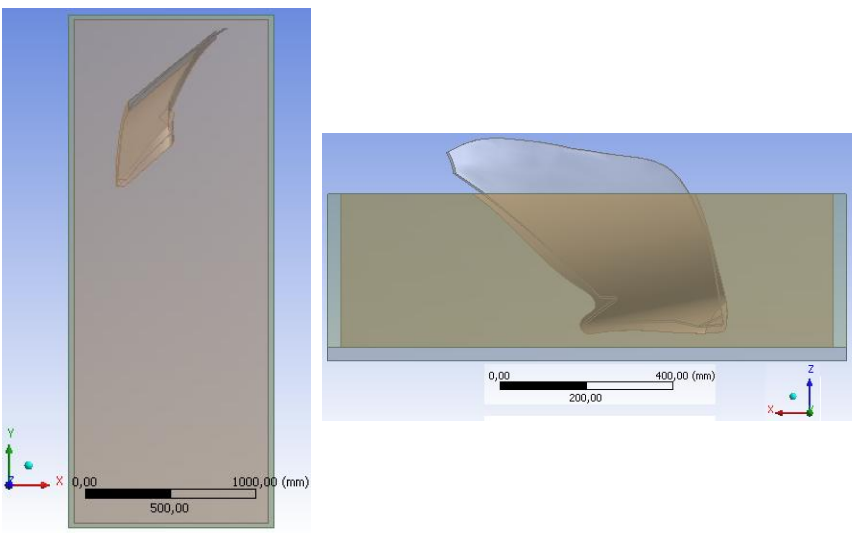

Figure 2. Experimentally studied plow moldboard

moldboard interaction. For this reason a sufficiently well presented experimental test with the appropriate results has been chosen from the available literature. Formato et al. [12] investigated experimentally and numerically a plow moldboard and compared the results. Figure 2 shows the experimentally studied plow moldboard Formato of et al. [12] The experimental test was carried out with operating velocity 2.86 m/s and working depth 0.3 m. Table 2 shows the known soil properties of the field where the experimental test was carried out. The measured draft force was 4150 N and the total pressure was monitored at 14 different points on the surface of the plow.

Table 2. Soil properties applied in the validation of the numerical calculations from Formato el al. [10]

Soil texture	Sandy loam
Sand [%]	81
Silt [%]	3
Clay [%]	16
Bulk density [kgm^{-3}]	2100
Moisture content [%]	12
Soil-Steel friction angle [deg]	0.4
Soil-Soil friction angle [deg]	0.6

4.2. **Validation of the Finite Volume CFD method.** The Bingham plastic material model has been validated by experimental tests published in the literature. The necessary mechanical properties of the soil to apply the Bingham model have not been specified: for this reason the unknown parameters have been specified by parameter identification. The known draft force and the pressure values on the surface of the moldboard have been used to specify the unknown yield stress and plastic viscosity values. Several combinations of the yield stress and plastic viscosity is examined from values $\tau_{ij} = 8$ kPa, $\eta = 0.1$ Pa s to $\tau_0 = 5$ kPa, $\eta = 1$ kPa s. Table 3 contains the values of the necessary parameters applied in the Bingham model. The calculated draft force with the specified model parameters is 4176.8 N in case of the Bingham model with visco-plastic parameters $\tau_0 = 7.1$ kPa, $\eta_0 = 0.1$ Pa s. The relative error is

$$\varepsilon_F = \frac{|F_{\text{Measured}} - F_{\text{Calculated}}|}{F_{\text{Measured}}} 100 = 0.00646 = 0.646 \quad [\%]$$

between the measured and the calculated results. The value of the soil plastic viscosity seems very small compared to the measured values $\eta \approx 50$–200 kPa presented by Karmakar and Kushwaha [22]. The main reason for the difference is that soil visco-plasticity values were measured for highly compacted conditions because Karmakar and Kushwaha [23] investigated flat tillage tool geometry where the soil is significantly compacted at the front region of the tillage tool. Zielinski et al. [24] report three orders of magnitude smaller plastic viscosity values $\eta \approx 0.05$–1 kPa for dry and wet soil with different kaolinite content. Plastic viscosity values of different types of soil with fall cone test has been measured by Mahajan and Budhu [25] and the results show that the soil viscosity values are in the range $\eta \approx 0.036$–0.328 kPa s similar to the results presented by Zielinski et al. [24]. The soil–moldboard interaction is a completely different tillage process because the soil is not compacted; it is rather loose in the case of plowing. This process further reduces the value of the visco-plastic parameters of the soil. Table 3 shows a quantitative comparison of the measured and calculated results with a simple statistical measure. Geometrical location of the control points can be seen in the second, third and fourth columns of Table 3 The following three columns show the measured and calculated pressure at those points and in the last column the relative error of the calculations is presented. Relative error of the pressure values has been calculated with the following formula

$$\varepsilon_P = \frac{|P_{\text{Measured}} - P_{\text{Calculated}}|}{P_{\text{Measured}}} 100\ [\%]\,.$$

Table 3. Comparison of the measured and the calculated results

Point	x [m]	y [m]	z [m]	Pressure [kPa]		Relative error [%]
				Measured	Calculated	Calculated
5	0.1649	0.44	0.30	23.000	20.7768	10.70
7	0.4182	0.68	0.31	12.000	12.5843	4.86
11	0.1477	0.32	0.19	24.000	21.9672	8.47
12	0.2884	0.28	0.09	28.000	25.0045	10.70
13	0.2192	0.20	0.09	30.000	27.0302	9.90
14	0.1460	0.12	0.09	32.000	33.6126	5.03

4.3. **Smoothed-particle hydrodynamics.** Figure 2 shows the computational domain with the investigated plow moldboard geometry. The greatest advantage of this method is that it is not necessary to calibrate the model if the real soil parameters are known. In this case the internal friction of soil, friction between soil and tool material, and the bulk density are known [12]. Bulk modulus, shear modulus are supposed as average soil, but the cohesion is not known. Calibration of cohesion was done by the measured draft force at a given speed [12]. Parameters for the SPH model are the following: coefficient of internal friction is $\mu_{\text{soil}} = 0.3$ coefficient of friction between soil and steel $\mu_{\text{soil-steel}} = 0.4$, bulk density of soil $\rho_p = 2100$ kgm^{-3}, bulk modulus $E_{\text{soil}} = 9.57 \times 10^6$ Pa, shear modulus $G_{\text{soil}} = 2.96 \times 10^6$ Pa, cohesion $c = 100$ Pa, particle size $h = 0.3$ m. Modeling the soil–tool interaction with the SPH model a 3m long segment of a soil bin has been used which was a width of 1.2 m, and the height was 0.385 m. A small gap is needed between the granular material (SPH model) and the solid surface of the investigated plow in the SPH discretization which can be seen in Figure 4. Boundary conditions were not specified at surface of SPH model in AUTODYN. A 30 mm thick walls were modelled at the bottom and four sides of the SPH soil model.

4.4. **Discrete element method.** *Data for the problem.* A clump of two spherical particles having 5 mm radius, with 8 mm distance between their centers was used as soil particle model. The particle size distribution in the final granular assembly modeling the soil was randomly changing between 5 mm and 7.5 mm radii. The following micromechanical parameters were calibrated for the description of the interaction between the soil particles, and between the soil particles and the tool (index p means soil particle, index t means tool material): Poisson's ratio $\nu_p = 02$, $\nu_t = 0.3$, shear modulus $G_p = 10^7$ Pa, $G_t = 8 \times 10^9$ Pa, density $\rho_p = 3200$ kg/m^3, $\rho_t = 7500$ kg/m^3. Coefficient of restitution: $C_{r,p-p} = C_{r,t-p} = 0.4$, coefficient of static friction $\mu_{p-p} = 0.9$, $\mu_{p-t} = 0.35$, coefficient of rolling friction $\mu_{r,p-p} = 0.015$, $\mu_{r,p-t} = 0.01$. For the bonded soil model we used: normal stiffness $S_n = 10^9$ Nm^{-3}, shear stiffness $S_t = 10^9$ Nm^{-3}, critical normal stress $\sigma_{\max} = 1.5 \times 10^6$ Pa, critical shear test $\tau_{\max} = 9 \times 10^5$ Pa, bonded disk radius $R_B = 0.005$ m.

Draft force prediction. For modeling the soil-tool interaction, the discrete element model of a 1 m long segment of a soil bin was used. The width of the duct was the double of the tool width, and in this direction a periodic boundary condition is used to simulate the effect of the neighboring soil particles. The use of periodic boundary in the direction perpendicular to the tool displacement direction enabled us to reduce effectively the size of the simulation domain, and in this way the simulation time requirements. The thickness of granular assembly beneath the tool was the same as the height of the tool itself. The simulation time step was set to be 25% of the Rayleigh time step, using the material parameters listed above. The simulation started with filling the calculation domain of the soil bin model with particles using

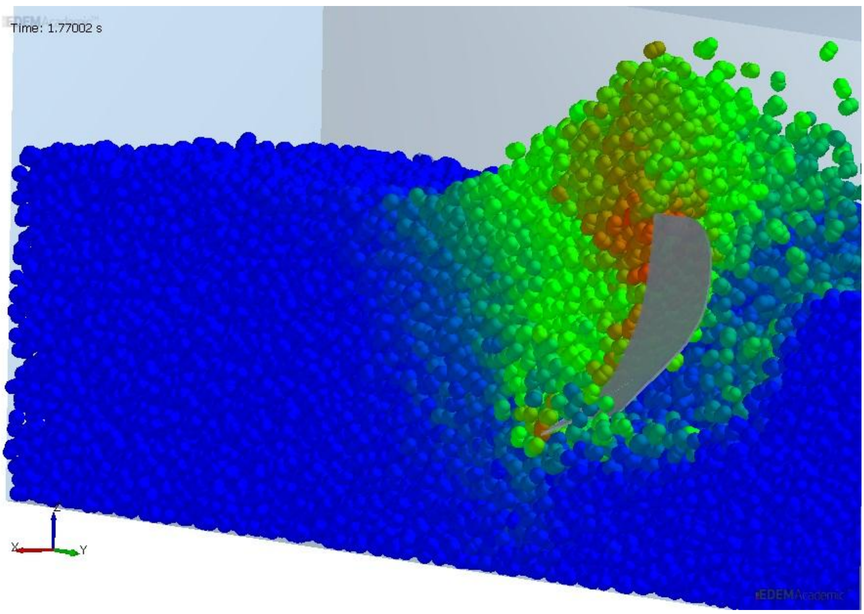

Figure 3. Soil-tool interaction DEM model, the tool geometry and the model bin are shown here, the boundary is periodic in x direction.

dropping method. We filled the bin with particles by letting their gravitational sedimentation form a randomly generated assembly initially filling the whole bin, and then settling down to a state when it was filling approximately one third of it (Figure 3). One second after this sedimentation process (this time needed to get the particles to be in a state of rest), we "turned on" the bonding model, gluing together the soil particles. After this, the tillage tool started its way through the bin. Only the forces acting in the middle third section of the model bin were used to evaluate the average draft force value, to avoid the effect of the end wall, and the effect of increasing the number of contacts during the tool's immersion in the soil.

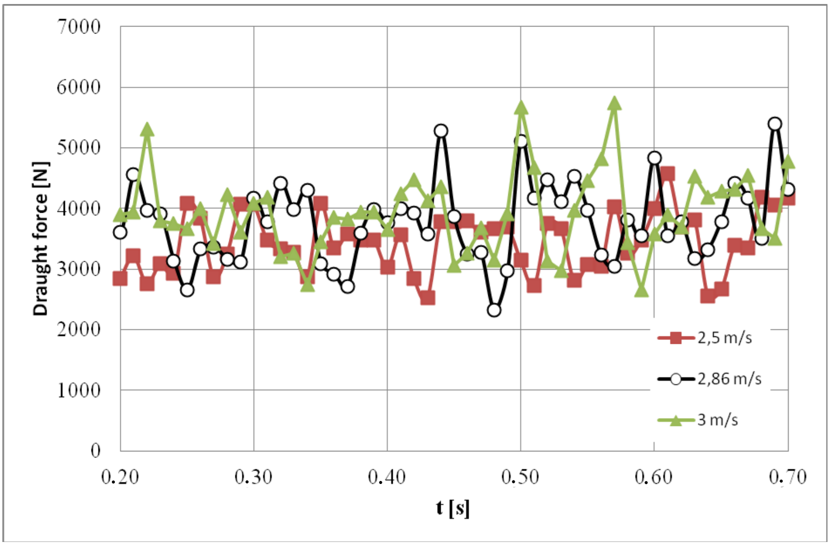

Figure 4. Sample diagram of measured and simulated draft forces

The simulated draft forces showed significantly higher deviation than the measured ones. This phenomenon is mainly caused by the large particle size used because of the restrictions in computer simulation capabilities. Sample simulation results can be seen in Figure 4. It can be seen, that the simulated draft forces are in good agreement with the measured ones [12]. The average plow forces related to different velocities are as follows:

v [m/s]	F [N]
2.00	3068.474
2.50	3445.344
2.86	3842.261
3.00	3930.810
3.50	4264.764

5. Results

5.1. **Finite volume method.** Figures 5 and 6 show some stages of the turnover of a furrow slice. It can be clearly seen that if the grid resolution is sufficiently fine in that case the soil-air interface is sharply recognizable.

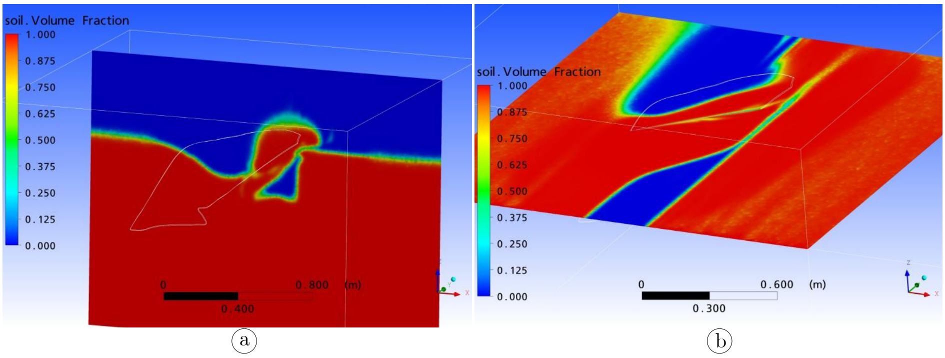

Figure 5. Perspective view of the furrow and the turn over of the furrow slice

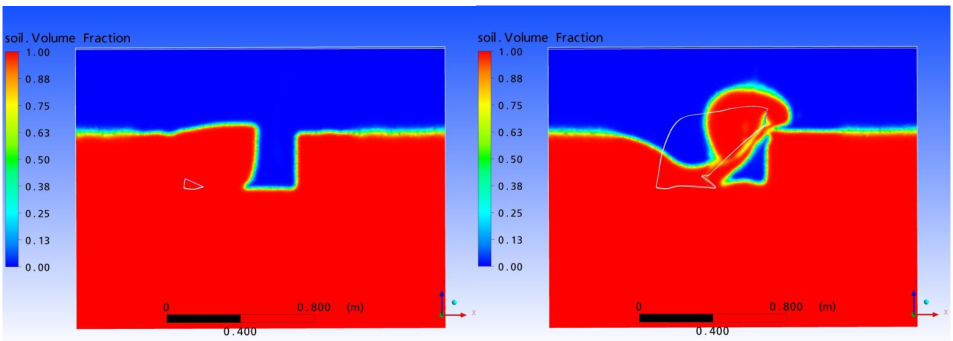

Figure 6. Front view of the furrow and the turn over of the furrow slice

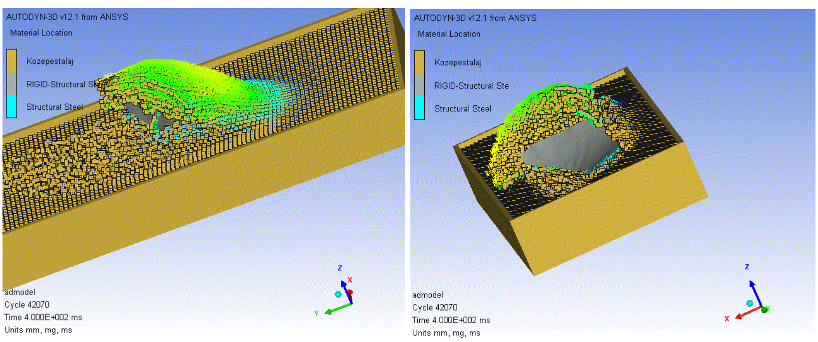

Figure 7. Perspective view of the flow movement in the case of SPH simulation

5.2. **SPH method.** Figure 7 shows the simulated deformation of SPH model of soil with 30 mm particle size. Predicted deformations are more realistic than DEM. Soil particles are much smaller than in the other two methods. Hence the SPH particles (which are not real particles) are better for prediction of deformations.

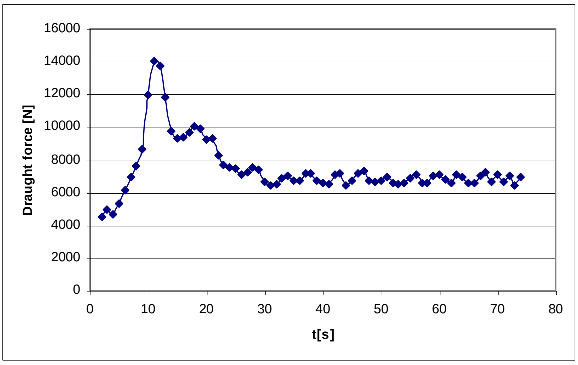

Figure 8. Sample diagram of measured and simulated draft forces

The real soil parameters are used in this method so it is not necessary to calibrate the model. But the uncalibrated model predicts higher draft forces than those measured. Another advantage of this method is prediction of transient stadium with local peak (Figure 8).

6. Conclusions

Three different mathematical modeling and numerical computation approaches have been applied to investigate the soil–tool interaction for a moldboard plow. Comparison made between the different modeling approaches to get information about the efficiency of the applied models was validated by an experimental test available from the literature. The following general conclusions can be drawn:

1. It can be stated that a validation with only a measured draft force value of a soil tillage tool is not enough to calibrate the different models correctly because of the complex behavior and structure of the soil. The models generally need a lot of measured parameters that have to be calibrated before the computation. For this reason it can be suggested that more information is needed to validate a numerical model than a single draft force value. For example pressure distribution on the surface of the tillage tool where the soil interacts with the tool or local velocity measurements of the flow field of the soil around the tillage tool can be useful additional information for model validation purposes.
2. Area of modeling possibilities: The finite volume CFD method effectively describes the flow behavior of granular materials that can be modeled by nearly spherical particles. Shortcomings: it is only capable of modeling the flow behavior of granular material which consists of nearly spherical particles with

smaller particle size than the conventional size of agricultural granular products (wheat, maize, barley, etc. The finite volume CFD method cannot be applied such granular materials where particle geometry significantly differs from spherical shape like stringy crops. It is difficult to specify correctly the physical properties of the modeled granular material. The proper value of the plastic viscosity and yield stress cannot be determined precisely because these properties are pressure dependent. For this reason the plastic viscosity and yield stress cannot be characterized with a constant value for computing soil flow. Computational requirements: the finite volume method needs significantly larger amount of computational resources, mostly operative RAM simulating sufficiently detailed interface between the soil–air and soil–tillage tool interaction compared to the other two investigated methods. The necessary calculation time takes two or even three times longer than the SPH-FEM and the DEM method.

3. Area of modeling possibilities: The Smoothed-Particle Hydrodynamics (SPH) method can be used effectively with flow cases where the flow field has a lot of separated regions. The SPH method is also sensitive to the particle size, which has to be chosen properly to avoid physically unacceptable oscillations of the solution.
4. Area of modeling possibilities: The Discrete Element Method can be considered the most widely applicable method to describe the flow process of granular materials, because it can use almost any kind of particle geometry and from physical modeling point of view it is the most realistic description of a granular material. For this reason the discrete element method is capable of effectively modeling the soil-tool interaction process. DEM is capable of simulating draft force, but the pressure distribution cannot be easily modeled by using DEM. The simulated draft forces showed significantly higher deviation than the measured ones. This phenomenon is mainly caused by the large particle size used because of the restrictions in computer simulation capabilities. There is no guarantee that the calibrated micromechanical parameters are the only ones resulting the desired draft force values. Shortcomings: the greatest problem with this modeling approach is that current computational resources cannot calculate with the same amount of particle numbers contained in a real granular material. The most difficult is the proper calibration of the DEM model. There are 12 parameters (including time step) to be properly calibrated for determining the micromechanical parameters describing the mechanical behavior of the particle assembly. By using the particle–rigid body interaction model, the reaction forces acting on the tool are not taken into account as excitations generating for example the vibration of the tool, which can cause errors in the modeling results, especially in case of easily vibrating tools. Computational requirements: computational time requirement is approximately 5 hours on a dual core P8600-2.4GHz 8GB RAM computer (this relatively short computational time was the result of low particle shear modulus). The calibration of micromechanical parameters is a significantly more time consuming procedure, because of the need for a large number of simulations to be done.

Acknowledgement. This paper was supported by the János Bolyai Research Scholarship of the Hungarian Academy of Sciences.

References

1. Karmakar, S., Kushwaha, R. L. and Lague, C.: Numerical modeling of soil stress and pressure distribution on a flat tillage tool using computational fluid dynamics. *Biosystems Engineering*, **97**(3), (2007), 407–414.
2. Godwin, R.: A review of the effect of implement geometry on soil failure and implement forces. *Soil & Tillage Research*, **97**, (2007), 331–340.
3. Godwin, R. J. and O'Dogherty, M. J.: Integrated soil tillage force prediction models. *Journal of Terramechanics*, **44**, (2007), 3–14.
4. Onwualu, A. P. and Watts, K. C.: Draught and vertical forces obtained from dynamic soil cutting by plane tillage tools. *Soil & Tillage Research*, **48**, (1998), 239–253.
5. Chandler, H. W.: The use of nonlinear fracture mechanics to study the fracture properties of soils. *Journal of Agricultural Engineering Research*, **29**, (1984), 321–327.
6. Aluko, O. B. and Chandler, H. W.: A fracture strength parameter for brittle agricultural soils. *Biosystems Engineering*, **93**(2), (2006), 245–252.
7. Kocher, M. F. and Summers, J. D.: Wave propagation theory for evaluating dynamic soil stress-strain models. *Transactions of the ASAE*, **31**(3), (1985), 683–691.
8. Rosa, U. A. and Wulfsohn, D.: Constitutive model for high speed tillage using narrow tools. *Journal of Terramechanics*, **36**, (1999), 221–234.
9. Mouazen, A. and Neményi, M.: Tillage tool design by the finite element method–part 1: finite element modeling of soil plastic behavior. *Journal of Terramechanics*, **72**, (1999), 37–51.
10. Elijah, D. L. and Weber, J. A.: Soil failure and pressure patterns for flat cutting blades. *Transactions of the ASAE*, **14**(4), (1971), 781–785.
11. Fielke, J. M.: Finite element modeling of the interaction of the cutting edge of tillage implements with soil. *Journal of Agricultural Engineering Research*, **74**, (1999), 91–101.
12. Formato, A., Faugno, S. and Paolillo, G.: Numerical simulation of soil-plough mouldboard interaction. *Biosystems Engineering*, **92**(3), (2005), 309–316.
13. Cundall, P. A. and Strack, O. D. L.: A discrete numerical model for granular assemblies. *Geotechnique*, **29**(1), (2012), 47–65.
14. DemSolutions: Edem User's Guide. 2012.
15. Monaghan, J. and Gingold, R.: Smoothed particle hydrodynamics. *Mon. Not. Roy. Astr. Soc.*, **181**, (2012), 375–389.
16. Hayhurst, C. J., Clegg, R. A., Livingstone, I. H. and Francis, N. J.: The application of sph techniques in AUTOSDYN-2d to ballistic impact problems. 16th International Symposium on Ballistics, San Francisco, CA, USA, 1966.
17. Chakraborty, S. and Shaw, A.: A pseudo-spring based fracture model for SPH simulation of impact dynamics. *International Journal of Impact Engineering*, **58**, (2013), 84–95.
18. Yang, Q., Jones, V. and McCue, L.: Free-surface flow interactions with deformable structures using an SPH–FEM mode. *Ocean Engineering*, **55**, (2012), 136–147.

19. Bui, H. H., Sako, K. and Fukagawa, R.: Numerical simulation of soil–water interaction using smoothed particle hydrodynamics (SPH) method. *Journal of Terramechanics*, **44**, (2007), 339–346.

20. Lu, Y., Wang, Z. and Chong, K.: A comparative study of buried structure in soil subjected to blast load using 2d and 3d numerical simulations. *Soil Dynamics and Earthquake Engineering*, **25**, (2005), 275–288.

21. Calamaz, M., Limido, J., Nouari, M., Espinosa, C., Coupard, D., Salaün, M., Girot, F. and Chieragatti, R.: Toward a better understanding of tool wear effect through a comparison between experiments and SPH numerical modelling of machining hard materials. *Int. Journal of Refractory Metals & Hard Materials*, **27**, (2009), 595–604.

22. Karmakar, S. and Kushwaha, R. L.: Dynamic modeling of soil-tool interaction: An overview from a fluid flow perspective. *Journal of Terramechanics*, **43**(4), (2005), 411–425.

23. Karmakar, S. and Kushwaha, R. L.: Development and laboratory evaluation of a rheometer for soil visco-plastic parameters. *Journal of Terramechanics*, **44**, (2007), 197–204.

24. Zielinski, M., Dembicki, E. and Monnet, J.: Studying slow displacements of the natural slopes using particle image velocimetry method. 18. Congres Francais de Mecanique, Grenoble, August 27-31, 2007.

25. Mahajan, S. P. and Budhu, M.: Shear viscosity of clays to compute viscous resistance. The 12th International Conference of International Association for Computer Methods and Advances in Geomechanics (IACMAG) 1-6 October, 2008, Goa, India, pp. 1516–1523.

Journal of Computational and Applied Mechanics, Vol. 11., No. 1., (2016), pp. 95–102
DOI: 10.32973/jcam.2016.007

SOME MODEL CREATION RELATED QUESTIONS OF ENGINEERING

Béla Csizmadia
Institute of Mechanics and Machinery, Szent István University
Páter K. u. 1., H-2103 Gödöllő, Hungary
Csizmadia.Bela@gek.szie.hu

[Received: September 29, 2015. Accepted: April 20, 2016]

Dedicated to Professor Barna Szabó on the occasion of his eightieth birthday and to Professor Imre Kozák on the occasion of his eighty-fifth birthday

Abstract. Model creation is the most important challenge for an engineer. Consciously or intuitively, the engineer always creates models in the course of the creative process. However this subject is not discussed – or only marginally –, in the classroom or in the literature. The aim of this article is to contribute to the more conscious model-creating work. For the sake of this, this paper formulates some underlying principles. These principles must be observed during the model-creating work, and by presenting them during the university studies we can help the students to learn this important engineering task. Three of these principles are universal statements, relating to the recognition of the world, and two of them must be considered during the creation of a correct model. Three conclusions from the underlying principles are also conducted; these are important for the technical practice. The methods of mechanical model creation are shortly discussed at the end.

Keywords: Model creation, underlying principles

1. Task of the engineer and model creation

The engineer summarizes the knowledge of predecessors in order to recognize the problems of present days and to solve them. All these things are done for the purpose of building a more human future. Thus the engineer analyzes and describes both natural and human–made reality. The only way to carry out this task is by creating models, examining and comparing their results with reality.

Ultimately, the highest task of an engineer is to properly choose models. Nowadays, tons of calculating methods are available; although it does make a great difference what kind of model we choose to apply, since we can only apply them on models.

The model is a simplified form of reality, which, regarding the observed phenomenon and the determined goal, behaves similarly to reality in some features.

So a model must be created. This can be either carried out only into an intuitive way combined with great experience. Unfortunately this 'great experience' cannot be taught, but still it is highly important to put this knowledge in an integrated form and share it. At the same time the education of model creation appears barely or not at all in the engineering studies. So to say, it is quite difficult to teach as well. The author of this paper made an attempt to fill this need. To this end the author systematized the model creation method, and tried to draw up in a teachable, learnable form. The results of this attempt are summarized in this article.

Model creation appears in two ways in practice:

(a) "paid–off way", normal way, by the use of approximations;
(b) by a lot of experience combined with intuition.

ad a. As in the traditional – manual – calculation, also in the computation calculations (FEM) there are common models, such as the truss beams, which are modeled by links, or the design of bolts according to the shear stresses or facial pressure. In these cases – in a lower or higher level – the engineer carries out a general routine in the process of solving the problem. The applied theories and methods are mentioned in the subject of mechanics, machine elements and in other technical sciences during their studies. In the wide range of application of FEM the user investigates the solution or output and not the question of the precise approximation or the proper choice of the boundary conditions. The 'that's the way we do it' way of thinking overtakes the user, and one will not be aware of the right time to use it differently.

ad b. The other wide field of the engineering model creation is when the problem is not a routine task but something new. Although too many times the "paid off way" is used, unfortunately in a wrong way. Professor Barna Szabo made a survey in the United States about the efficiency of the use of finite element programs in the industry. According to the results of this survey, approximately half of the results evaluated by finite element method were wrong. And the error was not related to the finite element program itself, the source of the error was the wrong model: it did not described the reality. This is why we need to pay attention to the model creation problem.

The aim of this paper is not to deal with modeling of a concrete problem. I would like to summarize and to give methods and general principles for active technical intellectuals in order to apply and support the most important engineering process: model creation, based on my experiences acquired during my educational and research activities.

2. General principles of model creation, a possible description of the phenomena

Randomness and order govern the universe with the same weight and emphasis. This duality is the fuel of experimental science. The lack of randomness would cause the common logic to deterministically describe the universe (and the closer – broader reality) in its complexity without the need of observation. On the other hand, if this reality did not include some kind of order and logic, then science would have never come into existence. Let us take an example to understand this duality more deeply.

The motions of gas particles in a closed vessel are entirely random, but the relation between its pressure, volume and temperature can be unequivocally determined. Randomness does not mean that there is no correlation between the motions of particles, but the initial conditions are random.

According to the unbreakable chain of randomness and order in the universe, in natural sciences – especially in engineering sciences – experimental and theoretical methods are mutually applied in research. This fact determines our knowledge about the physical world, because we can learn about the world based on two, well separated ways. One of them is direct experience, the other is the rational reasoning. Based on this, we can word the following:

1st Principle: One investigation must never be absolute according to the function of theory or experiments. Applying both at the same time will result in an adequate solution.

Nature is often said to be equal, united, and the world in it appears as a complete system, where everything is connected together. In a certain view this is true, but experiments show that even separated parts of reality can be precisely described without the knowledge of its entirety. What is the cause that gives us adequate information about the properly chosen parts? The reason is based on two peculiarity of the world: linearity and locality. A linear system – as is well known – can be easily investigated and described by two easily applied mathematical tools, addition and multiplication. However, using linear systems to determine a phenomenon is not obligatory in order to make the problem simpler. It is advised for use because it is possible. Naturally none of the systems are exactly linear. That fact raises a question: How is it possible to handle so many phenomena as a linear system? There are three reasons:

- In many cases the non-linear effects are very weak,
- The range of influence of non–linear effects is strongly determined,
- Many linear systems are not sensitive to weak perturbances.

Linearity exists in most cases, but it must be identified among the parameters.

The other peculiarity that makes the examination of the properly identified parts possible without the knowledge of the whole, is the locality. This means that in most cases the behavior of the physical systems is entirely influenced by the effects (external forces, moments, etc) of their very surroundings.

2nd Principle: Reality can be dissembled and information can be gained by only examining separated parts and not the whole.

According to these observations and the 2nd principle, the following conclusion can be drawn:

In model creation, a very important step is to make clear what we wish to measure in what function.

As we mentioned above, there are two, well-separated ways to gain information about the world. One is direct experience; the other is rational reasoning. The fall of an apple can be an example. Sensory perception, which is a direct experience, can provide measured data about the fall of an apple. It is also possible to gain more information about this phenomenon, in a different and deeper way. By the combination of Newton's laws and some mathematical skills a model can be created to investigate the falling apple. This model is not based on our sensory perception but on our mind which – by the use of the earlier universalized experiences and laws – finds the correlation between the once fallen apple and the deeper, comprehensive physical processes. Now the examination of the mechanical model is possible with the applied physical-mathematical model. Although it is unseen, still – in its abstract way – it is able to provide information about reality in a higher, more general way. At the same time these laws were and are created by people based on their sensory perceptions. The 3rd principle is applied to these natural laws. Here it must be highly emphasized that natural laws were not made by mankind but discovered. The laws are independent, and they always existed.

3rd Principle: Natural principles are absolute and irrespective of space, entirely valid in time, and it is possible to involve them in a mathematical form. They are independent of the observer, and the condition of the phenomena. The parts of nature are not abstract mathematical formations.

Thus if we engineers create a model by observing a phenomenon and we lay down new formulas, these are not natural laws. They do not operate in every case. This conclusion provides a new principle to engineer researchers:

According to the given results and the model, the limits of applicability of the model must be determined.

3. Basic principles of model creation

Creating a model raises one question: abstraction. Abstraction is not solely an engineering activity or method but a fundamental skill of humanity. Let us explain it with an example. If a father tells his child – who probably does not even talk – to sit down on a chair in a foreign environment, the child will most likely go to a chair and sit on it. Not on a pillow, ground or a couch, but on a chair. He will sit on a chair even if he has never seen that chair before, irrespectively of whether the chair has three or four legs, with or without a back, upholstered or not, smooth, fret worked, wooden or iron, etc.

Basically he recognizes the chair as an abstracted concept, and he does not look for a certain object. Abstraction is also the fundamental existence of mathematics. In order to say 'five stones and two stones are seven stones' we have to neglect the form, material structure and color. The concept of stone must be abstracted, where the stones are isolated substances.

Obviously the concept of the examined or observed object or phenomenon must be determined by taking into consideration the observing purpose. Let us investigate this statement with another simple example. If we wish to analyze a chair, furniture or other wooden structure, different denotations must be addressed to each of them.

All of them have different models. Some peculiarities are highlighted and concerned dominant and others are neglected according to the purpose of modeling.

When we examine a phenomenon, not only the phenomenon itself, but the aim of our investigation is also important. The limits of applicability must also be taken into account based on this.

4th Principle: The model is also determined by the aim of investigation.

Ultimately let us talk in general about the relation of model and reality. As we have already declared, the model is a simplified form of reality which behaves similarly to reality in some features. Similarly, but not entirely exactly! The difference is the error of the model creation. What is the origin of this error or difference between the model and reality? Firstly, the model describes the order of reality and neglects its randomness. Secondly, the model only takes into account order determining parameters respective to the chosen observing aims, so we are not talking about an entire analogy. Thirdly, there can be differences in the calculations of the created model, since there are approximations in the equations and so also in the solutions.

Ultimately the result is not the same between reality and the model. The cause of the difference must be found in the model, not in the natural laws. Let us verify it with an old, astromechanic example. The law of mass attraction is well known. Taking into account the Sun and the planets of our solar system, a model was created about the motion track of Neptune. According to the model – taking into account the law of mass attraction – the calculated result did not correspond with the astronomers' observation. Maybe the law of mass attraction did not work there? Or some important feature was neglected in the model? Eventually, they came to the following conclusion: one external effect caused the anomaly in the motion. Then they appointed a certain position at a certain time in the sky looking for the mysterious perturbance. Thus they discovered Pluto. Therefore the model was incorrect for determining the motion track of Neptune. That is why the calculated result did not correspond with reality.

5th Principle: The created models provide new information about the world, but these results must be always compared with reality and the chosen aim. Decisions about the adequateness of the model must be based on the collective results.

According to the 4th and 5th principles a conclusion can be drawn for the technical practice:

the correct model is as simple as it can be, but properly approximates reality regarding the aims for examinating.

4. Methods of mechanical model creation

We have already discussed the concept that the phenomena and the examining aims determine the model, and also that the model is as simple as possible. The purpose of model creation has been also investigated. Let us discuss what methods are possible to use in order to create models. The following investigations – regarding the examples – will be limited to mechanical models. Three methods are adequate to reach our goals.

4.1. **Analytical 'exact' models.** The 'exact' word in the subhead means that the error of the model is within the range of the limited margin of error regarding the aim of examination. In these models the estimation or error is generally based on hundreds of years engineering experience. The complete model can be obtained by these experience verified modelparts. Intuition and the engineering experience have a great relevancy in these cases. Most of the routine engineering models are analytical.

One great feature of the analytical models is the relatively easy parameter identification. Parameter identification reveals what effects the gradient of the parameters perform on the phenomena. This method easily allocates the dominant parameters in a given domain. In addition the parameter identification allows the optimum search algorithm, which can be essential in economical or feasibility aspects.

4.2. **'Approximating' models.** Modeling extremely complex phenomena adduces the application of an initial, but not entirely accurate – regarding the examining aims – model. Most of the times these models are not created by necessity, but after mature deliberation. Let us investigate the reasons that may cause the application of approximating models!

Concept of successive approximation. The engineer does not always find an adequate model. Thus one must start with the model which seems to be the simplest, and by examining the result, a conclusion must be drawn whether it is necessary to use a more advanced model. Step by step, the engineer approaches the simplest, usable and precise enough model. It is also possible if one does not find out all the approximating models, but creates only the proper model.

Complex solution. One problem can be approached in a complex way as well: this is the collective application of theoretical and experimental models. This method is often used in research when the solution of the problem requires experimental methods. Not even in these cases should we surrender the numerical, mechanical, theoretical model creation, even if the model is a coarse approximation of reality. The possible (sometimes really coarse, or just not accurate enough) approximating model must be created since it can greatly support the description of the phenomena in two ways:

- to create the possibility of the equation analysis and the application of analogy laws, or to draw up the model laws which are helpful in the evaluation of the experimental results.
- to decrease the number of parameters and allow the approximation with product-function:

$$y = f_1(x_{11}, x_{12}, \ldots)\, f_2(x_{21}, x_{22}, \ldots)$$

where the function f_2 is the solution of the approximating model, while

$$y(x_{11}, \ldots, x_{21})$$

is the experimental result and $f_1(x_{11}, x_{12}, \ldots)$ is the result of the experiment, which can be used for the determination of the coefficient f_1.

Let's see a simple, elementary example to shed light on this, of course, this example is not a task to be implemented. Suppose that we have a cantilever beam fixed at one of its ends by screws. We would like to evaluate the deflection of the beam's endpoint, because we do not know the rigidity of its support. However, we do not want to determine the concrete deflection of one given beam, but the behavior of the whole system. We have a computational model for the determination of the deflection:

$$y = \frac{f\ell^3}{3IE} = \frac{1}{3} f_2(x_{21}, x_{22}, \ldots) \tag{1}$$

This equation is not a model for the problem, because the number, the size, position and the screwing torque of the screws and the rigidity of the support can modify the deflection. Suppose that we would like to describe these effects by measurements, i.e. we would like to introduce a changing variable instead of the 1/3 multiplier. This changing variable will be determined as a function of measurements:

$$y = f_1(x_{11}, x_{12}, \ldots) \, \frac{f\ell^3}{IE} \tag{2}$$

Based on this method, we get a general, complex solution. Of course, this method is not used for such simple problems, this is just an illustrative example.

Model creation for experimental model. In this case not the mechanical but the experimental is the approximating model. If we wish to verify the behavior of an existing mechanical structure – taking into consideration the specifications – then the experimental investigations may turn out to be extremely costly. Thus we carry out the investigations on – a fairly proper – simpler experimental model. Even in this case a theoretical model must be created for the description of the approximating experimental model in order to verify the applicability of the experimental model.

Parameter identification. This is the most peculiar and important case of the approximating models. The examining aim is so complex that it is impossible to describe it with an analytical model. Here the possible use of a numerical model makes an appearance regarding the given mechanical structure. At the same time if the aim is not verification but design, then first a construction must be achieved. This is often determined by earlier experience of the designer. Rationally first an approximating analytically solvable model must be set up in order to carry out parameter identification. After the identification, optimization must be undertaken. The construction designed in this manner now is ready to be investigated with the more precise numerical model. If the results need more modification then it will take far less effort. This method is quite efficient and successful.

4.3. **Numerical models.** In the previous subhead the possibility to approximate reality with numerical models has been already declared. This numerical model can be either the result of a former approximating model, or a directly created model as well. Primarily the latter is used in verification, in those cases when not the mechanical model is dominant in the determination of the construction.

So far, only a few numerical models are suitable for optimization (one example is the evolutional model), and their capabilities are also limited to a narrow range of application. These problems cannot be solved other way. At this moment these models represent the most complex methods of model creation.

Finally we have to draw attention to the fact that numerical models are not suitable to solve complex engineering problems in general. They can act as supplement in the application and they complements the possible applicable tools, but the given results must be understood, defined, and put into context in the whole by the engineer. The problem cannot be solved either by computer, or with excellent program systems, but only by creative engineer.

5. Educational application of the model creation's basic principles

The author of this article summarized the basic principles in a book titled Model Creation. This book is the fourth in the textbook series Mechanics for Engineers. After the detailed exposition of the basic principles and presentation of basic examples, the book – written by several authors – presents a large number of case studies. These case studies are the solutions of real industrial problems, and there are references within them to the basic principles of model creation, and their implementation. The textbook is for the compulsory subject called Model creation in the MSc engineering program. After studying the basic principles, all the students had the task of analyzing a structure and the creation of all of its models. For solving this, the students had to use all of their mechanical knowledge studied in the previous five semesters and the information written in the textbook. Thus, they had an integrated, creative task that could only be solved by participating in large number of personal consultations. It is my experience and belief, that in this way the students gained knowledge on the creative engineering tasks, and the earliest possible learning of more effective engineering work.

Notes for Contributors

to the Journal of Computational and Applied Mechanics

Aims and scope. The aim of the journal is to publish research papers on theoretical and applied mechanics. Special emphasis is given to articles on computational mechanics, continuum mechanics (mechanics of solid bodies, fluid mechanics, heat and mass transfer) and dynamics. Review papers on a research field and materials effective for teaching can also be accepted and are published as review papers or classroom notes. Papers devoted to mathematical problems relevant to mechanics will also be considered.

Frequency of the journal. Two issues a year (approximately 80 pages per issue).

Submission of Manuscripts. Submission of a manuscript implies that the paper has not been published, nor is being considered for publication elsewhere. Papers should be written in standard grammatical English. The manuscript is to be submitted in electronic, preferably in pdf, format. The text is to be 130 mm wide and 190 mm long and the main text should be typeset in 10pt CMR fonts. Though the length of a paper is not prescribed, authors are encouraged to write concisely. However, short communications or discussions on papers published in the journal must not be longer than 2 pages. Each manuscript should be provided with an English Abstract of about 50–70 words, reporting concisely on the objective and results of the paper. The Abstract is followed by the Mathematical Subject Classification – in case the author (or authors) give the classification codes – then the keywords (no more than five). References should be grouped at the end of the paper in numerical order of appearance. Author's name(s) and initials, paper titles, journal name, volume, issue, year and page numbers should be given for all journals referenced.

The journal prefers the submission of manuscripts in LaTeX. Authors should select the AMS-LaTeX article class and are not recommended to define their own LaTeX commands. Visit our home page for further details concerning how to edit your paper.

For the purpose of refereeing the manuscripts should be sent either to Balázs TÓTH (Balazs.TOTH@uni-miskolc.hu) or György SZEIDL (Gyorgy.SZEIDL@uni-miskolc.hu).

The eventual supply of an accepted for publication paper in its final camera-ready form will ensure more rapid publication. Format requirements are provided by the home page of the journal from which sample LaTeX files can be downloaded:

http://www.mech.uni-miskolc.hu/jcam

These sample files can also be obtained directly (via e-mail) from Balázs TÓTH (Balazs.TOTH@uni-miskolc.hu), upon request.

One issue of the journal and ten offprints will be provided free of charge and mailed to the correspondent author. Since JCAM is an open access journal each paper can be downloaded freely from the homepage of the journal.

The Journal of Computational and Applied Mechanics is abstracted in Zentralblatt für Mathematik and in the Russian Referativnij Zhurnal.

Secretariat of the Vice-Rector for Research and International Relations, University of Miskolc
Responsible for publication: Prof. Dr. Tamás Kékesi
Published by the Miskolc University Press under the leadership of Attila Szendi
Responsible for duplication: Works manager Erzsébet Pásztor
Number of copies printed: 75
Put to the Press on July 1, 2016
Number of permission: TNRT 2016-200-ME **HU ISSN 1586–2070**

A Short History of the Publications of the University of Miskolc

The University of Miskolc (Hungary) is an important center of research in Central Europe. Its parent university was founded by the Empress Maria Theresa in Selmecbánya (today Banska Štiavnica, Slovakia) in 1735. After the first World War the legal predecessor of the University of Miskolc moved to Sopron (Hungary) where, in 1929, it started the series of university publications with the title *Publications of the Mining and Metallurgical Division of the Hungarian Academy of Mining and Forestry Engineering* (Volumes I.-VI.). From 1934 to 1947 the Institution had the name Faculty of Mining, Metallurgical and Forestry Engineering of the József Nádor University of Technology and Economic Sciences at Sopron. Accordingly, the publications were given the title *Publications of the Mining and Metallurgical Engineering Division* (Volumes VII.-XVI.). For the last volume before 1950 – due to a further change in the name of the Institution – *Technical University, Faculties of Mining, Metallurgical and Forestry Engineering, Publications of the Mining and Metallurgical Divisions* was the title.

For some years after 1950 the Publications were temporarily suspended.

After the foundation of the Mechanical Engineering Faculty in Miskolc in 1949 and the movement of the Sopron Mining and Metallurgical Faculties to Miskolc, the Publications restarted with the general title *Publications of the Technical University of Heavy Industry* in 1955. Four new series - Series A (Mining), Series B (Metallurgy), Series C (Machinery) and Series D (Natural Sciences) - were founded in 1976. These came out both in foreign languages (English, German and Russian) and in Hungarian.

In 1990, right after the foundation of some new faculties, the university was renamed University of Miskolc. At the same time the structure of the Publications was reorganized so that it could follow the faculty structure. Accordingly three new series were established: Series E (Legal Sciences), Series F (Economic Sciences) and Series G (Humanities and Social Sciences). The latest series, i.e., the series H (European Integration Studies) was founded in 2001. The eight series are formed by some periodicals and such publications which come out at various frequencies.

Papers on computational and applied mechanics were published in the

Publications of the University of Miskolc, Series D, Natural Sciences.

This series was given the name Natural Sciences, Mathematics in 1995. The name change reflects the fact that most of the papers published in the journal are of mathematical nature though papers on mechanics also come out.

The series

Publications of the University of Miskolc, Series C, Fundamental Engineering Sciences

founded in 1995 also published papers on mechanical issues. The present journal, which is published with the support of the Faculty of Mechanical Engineering and Informatics as a member of the Series C (Machinery), is the legal successor of the above journal.

Journal of Computational and Applied Mechanics

Volume 11, Number 1 (2016)

Contents

Contributed Papers

Krzysztof BOGDANSKI, Jean-Michel DHAINAUT and Andres JOSEPHSOHN: Optimization algorithms for laminated composite panels using nonlinear modal finite elements 3–16

István ECSEDI and Attila BAKSA: Spherical strain state of incompressible elastic bodies 17–32

József FARKAS: Comparisons of welded steel structures designed for minimum cost 33–48

Sándor SZIRBIK: Hypersingular boundary integral formulations for plane elasticity in terms of first–order stress functions 49–66

Péter. T. ZWIERCZYK and Károly VÁRADI: FE modelling of a coupled thermal-elastic-plastic analysis in a rail-wheel contact 67–76

András ZAHÁR, István KEPPLER and István OLDAL: Investigation of the applicability and efficiency of different mathematical modeling and numerical simulation methods for soil–tool interaction 77–94

Classroom Note

Béla CSIZMADIA: Some model creation related questions of engineering 95–102